

Department of Physics and Astronomy  
University of Heidelberg

Master Thesis in Physics  
submitted by

**Christian Möhler**

**2014**

**D-meson production at ultra-low transverse momentum in  
proton-proton collisions with ALICE at the LHC**

This Master Thesis has been carried out by  
Christian Möhler

at the  
University of Heidelberg

under the supervision of  
PD Dr. Kai Schweda

## Abstract

The measurement of charm production provides valuable insights into the properties of the Quark-Gluon Plasma, which is expected to be formed in ultra-relativistic heavy-ion collisions at the Large Hadron Collider (LHC) at CERN. The high-precision tracking and particle identification capabilities of A Large Ion Collider Experiment (ALICE) allow for the measurement of D mesons in hadronic decay channels, based on the reconstruction of secondary decay vertices. For weakly decaying D mesons, these are typically displaced from the primary vertex by a few hundred  $\mu\text{m}$ . However, this topological approach will inevitably fail at low transverse momentum ( $p_{\text{T}}$ ), where the Lorentz boost is not strong enough to be resolved. Current ALICE results of D-meson production using this analysis strategy are therefore limited to  $p_{\text{T}} > 1 \text{ GeV}/c$ .

This thesis presents a new measurement of the  $p_{\text{T}}$ -differential cross section of prompt  $\text{D}^0$  production in the decay channel  $\text{D}^0 \rightarrow \text{K}^- \pi^+$  at mid-rapidity in proton-proton collisions at  $\sqrt{s} = 7 \text{ TeV}$ . By giving up the topological selection, the presented analysis extends the measurable  $p_{\text{T}}$  range down to zero. The extraction of a stable signal at low  $p_{\text{T}}$  is made possible by using the like-sign background subtraction technique. In the overlapping  $p_{\text{T}}$  range, the results of this work are consistent with those obtained using the standard topological approach. The  $p_{\text{T}}$ -integrated charm production cross section at mid-rapidity can be given without extrapolation for the first time at the LHC, resulting in  $d\sigma^{c\bar{c}}/dy = (879 \pm 135) \mu\text{b}$ , which represents an increase in precision by about a factor two over the previous topological measurement.

## Zusammenfassung

Die Messung der Produktion von Charm-Quarks gewährt einen wertvollen experimentellen Zugang zu den Eigenschaften des Quark-Gluon-Plasmas, welches wahrscheinlich in ultra-relativistischen Schwerionenkollisionen am LHC (Large Hadron Collider) am CERN erzeugt wird. Dank präziser Teilchenspurrekonstruktion und Teilchenidentifikation können mit dem ALICE-Detektor D-Mesonen über ihre hadronischen Zerfallskanäle gemessen werden. Hierbei wird ausgenutzt, dass abhängig von der Lebensdauer eines D-Mesons der Zerfallsvertex typischerweise um einige hundert Mikrometer vom primären Vertex entfernt ist. Dieser topologische Ansatz kann allerdings nicht für die Messung von D-Mesonen mit niedrigem Transversalimpuls ( $p_T$ ) verwendet werden, da die geringe Zerfallslänge nicht im Detektor aufgelöst werden kann. Alle gegenwärtig veröffentlichten Ergebnisse der ALICE-Kollaboration zur Messung von D-Mesonen beschränken sich daher notwendigerweise auf Transversalimpulse  $p_T > 1 \text{ GeV}/c$ .

In der vorliegenden Arbeit wird eine neue Messung des  $p_T$ -differentiellen Wirkungsquerschnitts der Produktion von D-Mesonen bei mittlerer Rapidität vorgestellt. Hierbei wurde der Zerfallskanal  $D^0 \rightarrow K^- \pi^+$  in Protonenkollisionen bei einer Schwerpunktsenergie von  $\sqrt{s} = 7 \text{ TeV}$  analysiert. Durch Verzicht auf eine topologische Selektion konnte der gemessene Transversalimpulsbereich bis hin zu  $0 \text{ GeV}/c$  erweitert werden. Die Signalextraktion wurde dabei durch die Verwendung der "Like-Sign"-Methode stabilisiert. In dem Transversalimpulsbereich, der von beiden Analysen abgedeckt wird, stimmen die Resultate der hier vorgestellten Messung mit denen der topologischen Messung überein. Zum ersten Mal am LHC ist es nun möglich, den  $p_T$ -integrierten Wirkungsquerschnitt der Charm-Produktion bei mittlerer Rapidität in Protonenkollisionen ohne eine Extrapolation in  $p_T$  anzugeben. Der ermittelte Wirkungsquerschnitt beträgt  $d\sigma^{c\bar{c}}/dy = (879 \pm 135) \mu\text{b}$ . Im Vergleich zur topologischen Analyse konnte der Messfehler auf die Hälfte reduziert werden.

# CONTENTS

---

<b>1</b>	<b>Introduction</b>	<b>1</b>
<b>2</b>	<b>D-Meson Production in Hadronic Collisions</b>	<b>5</b>
2.1	Key Features of Quantum Chromodynamics . . . . .	5
2.2	Exploring the QCD Phase Diagram . . . . .	7
2.3	Heavy Quarks in the QGP . . . . .	9
2.4	Open Charm and Charmonium . . . . .	13
2.5	Theoretical Predictions for Heavy-Flavour Production . . . . .	15
<b>3</b>	<b>ALICE at the LHC</b>	<b>19</b>
3.1	LHC Experiments and Physics Programme . . . . .	19
3.2	ALICE Detector Overview . . . . .	20
3.3	Inner Tracking System . . . . .	21
3.4	Time Projection Chamber . . . . .	22
3.5	Time of Flight . . . . .	23
3.6	T0 . . . . .	23
3.7	V0 . . . . .	24
<b>4</b>	<b>The <math>D^0</math> Decay</b>	<b>25</b>
4.1	$D^0$ Decay Modes . . . . .	25
4.2	$D^0$ Decay Kinematics . . . . .	27
4.2.1	Momentum-Space Variables . . . . .	27
4.2.2	Invariant Mass . . . . .	29
4.2.3	Decay Length . . . . .	29
4.2.4	Kinematics of a Two-Body Decay . . . . .	31
4.2.5	A Toy Monte Carlo for Decay Kinematics . . . . .	31

<b>5</b>	<b>Data Analysis</b>	<b>34</b>
5.1	Strategy and Overview . . . . .	34
5.2	Computational Analysis . . . . .	36
5.3	Data Sets and Event Selection . . . . .	37
5.4	Track Reconstruction and Selection . . . . .	38
5.5	Particle Identification . . . . .	42
5.5.1	PID Information from TPC and TOF . . . . .	42
5.5.2	PID Strategy . . . . .	44
5.6	Signal Extraction . . . . .	46
5.6.1	Overview and Preliminary Considerations . . . . .	46
5.6.2	Background Subtraction . . . . .	49
5.6.3	Fitting Procedure . . . . .	54
5.6.4	Randomised Multi-Trial Approach . . . . .	56
5.7	Efficiency Correction . . . . .	57
5.8	Feed-Down Correction . . . . .	59
5.9	Calculation of the Cross Section . . . . .	61
<b>6</b>	<b>Uncertainties</b>	<b>63</b>
6.1	Statistical Uncertainties . . . . .	63
6.2	Systematic Uncertainties . . . . .	64
<b>7</b>	<b>Results</b>	<b>67</b>
7.1	$D^0$ Production Cross Section . . . . .	67
7.2	Total Charm Production Cross Section . . . . .	70
<b>8</b>	<b>Summary and Outlook</b>	<b>74</b>

# LIST OF FIGURES

---

2.1	The ‘running’ of the strong coupling constant $\alpha_s$ as a function of the energy scale $Q$ . . . . .	6
2.2	Sketch of a possible QCD phase diagram. . . . .	8
2.3	Generation mechanisms of quark masses . . . . .	10
2.4	Relative abundances of charmed hadrons in pp collisions . . . . .	11
2.6	Feynman diagrams of the leading-order (LO) processes of heavy-flavour pair production. . . . .	16
2.7	Feynman diagrams of two contributions to the heavy-quark pair production cross section at next-to-leading order (NLO). . . . .	16
2.8	FONLL predictions of the $D^0$ $p_T$ spectrum . . . . .	18
3.1	Sketch of ALICE with labels for the different subsystems . . . . .	20
4.1	Feynman diagrams of the Cabibbo-favoured decay $D^0 \rightarrow K^- \pi^+$ (left) and the doubly Cabibbo-suppressed decay $D^0 \rightarrow K^+ \pi^-$ (right). . . . .	25
4.2	Average $D^0$ decay length in the lab frame as a function of the $D^0$ transverse momentum and rapidity. . . . .	30
4.3	Simulated kinematics of the $D^0 \rightarrow K^- \pi^+$ decay. . . . .	33
5.1	Distribution of the $z$ position of reconstructed vertices in pp and Pb-Pb collisions. . . . .	37
5.2	Flow chart for the different stages of the tracking procedure. . . . .	39
5.3	ITS-TPC matching efficiency in pp collisions with different requirements of ITS and SPD clusters. . . . .	41
5.4	TPC $dE/dx$ signal (left) and Lorentz $\beta$ from TOF information (right) as a function of the reconstructed track momentum $p$ . . . . .	43

5.5	The PID $n_\sigma$ variable for the kaon (top) and pion (bottom) mass hypotheses in TPC (left) and TOF (right). . . . .	45
5.6	Overview of the structure of the $K\pi$ invariant mass distribution for $D^0$ candidates in two selected $p_T$ intervals. . . . .	47
5.7	Invariant mass distribution for $D^0$ candidates, as well as like-sign, track-rotation and event-mixing background. . . . .	51
5.8	Signal to background ratio before and after like-sign subtraction (left) and the remaining residual background in percent (right). . . . .	54
5.9	Invariant mass distribution after like-sign subtraction for all analysed $p_T$ intervals. . . . .	55
5.10	Comparison between data and Monte Carlo of the position $\mu$ and the width $\sigma$ of the $D^0$ peak. . . . .	56
5.11	Distribution of the extracted raw yield, using the multi-trial approach with one thousand random parameter configurations. . . . .	57
5.12	Acceptance and efficiency for the selections specified in previous chapters.	59
5.13	Prompt fraction $f_{\text{prompt}}$ . . . . .	60
7.1	Transverse momentum dependence of the $D^0$ production cross section at mid-rapidity in pp collisions at $\sqrt{s} = 7$ TeV. . . . .	68
7.2	LHC measurements of the total charm production cross section in pp collisions at $\sqrt{s} = 7$ TeV. . . . .	72
7.3	Total charm cross section in nucleon-nucleon collisions as a function of the centre-of-mass energy. . . . .	73

## LIST OF TABLES

---

2.1	Properties of charmed mesons and their most important resonances . . . .	12
2.2	Parameters included in FONLL calculations of heavy-flavour production. .	17
5.1	Selection cuts for single tracks used in this analysis. The cuts are labelled for reference in the text. . . . .	40
5.2	Raw yield, efficiency correction and prompt fraction as an input to $D^0$ production cross section. . . . .	62
6.1	Summary of the statistical uncertainties of the $D^0$ production cross section in percent. . . . .	64
6.2	Summary of the systematic uncertainties on the $D^0$ production cross section.	66
7.1	$D^0$ production cross section at mid-rapidity in pp collisions at $\sqrt{s} = 7$ TeV, as obtained with this analysis (left) and with the topological analysis (right).	69
7.2	LHC measurements of the total charm production cross section in pp collisions at $\sqrt{s} = 7$ TeV. . . . .	72

# INTRODUCTION

---

It is the goal of particle physics to explore the building blocks of matter and their interactions on the most fundamental level. In a constant interplay of theory and experiment, great progress has been made in the last few decades to establish a consistent description of fundamental interactions between elementary particles, which is known today as the Standard Model of Particle Physics. This theory is formulated in the context of relativistic quantum field theories and comprises the description of the electromagnetic and the weak force in the electroweak sector and the strong force in Quantum Chromodynamics (QCD). An important milestone was the unification of the electromagnetic and the weak force via the introduction of a symmetry breaking mechanism in the electroweak theory, sometimes also referred to as Glashow-Weinberg-Salam theory after its founders [1–3] and the proof of its renormalisability [4]. Though it is known that the Standard Model does not describe all of the phenomena observed in nature, it has been tested to very high precision in the regime of its validity. No disagreement between theory and experiment has yet been found.

The main experimental tools for high-energy particle physics are large particle colliders in combination with specialised particle detectors. Over the last few decades, colliders and detectors have grown larger and more powerful, both profiting from and inspiring the development of new technology. In 2009, a new era in experimental particle physics began with the start of data taking at the Large Hadron Collider (LHC) at the European Organization for Nuclear Research (CERN). As a proton and heavy-ion collider, the LHC breaks new ground both in its design centre-of-mass energy for proton-proton collisions of 14 TeV, corresponding to a centre-of-mass energy per nucleon pair of 5.52 TeV in Pb–Pb

collisions, and in its design luminosity of  $10^{34} \text{ cm}^{-2}\text{s}^{-1}$ . Currently, as of the end of 2014, the LHC is in a maintenance period, the Long Shutdown I, and is being prepared for its second period of operation and data taking (Run II). In Run I from 2009 until 2013, the LHC provided extensive data sets for proton-proton (pp) collisions at a centre-of-mass energy of 0.9 TeV, 2.76 TeV, 7 TeV and 8 TeV; lead-lead (Pb–Pb) collisions with a centre-of-mass energy per nucleon pair of 2.76 TeV; and proton-lead (p–Pb) collisions at a centre-of-mass energy per nucleon pair of 5.02 TeV. The most prominent LHC result so far was the discovery of a new resonance with a mass of  $125 \text{ GeV}/c^2$  in 2012 by the Toroidal LHC Apparatus (ATLAS) and the Compact Muon Solenoid (CMS) [5, 6]. Up until now, the properties of this resonance are compatible with the Standard Model Higgs boson and are currently under further investigation. Already predicted in 1964 [7, 8], the Higgs boson was the last missing particle in the Standard Model to be experimentally confirmed.

Besides the rich physics programme related to the electroweak theory and its symmetry breaking mechanism or to the search for ‘new physics’ beyond the Standard Model, the LHC provides an excellent environment for the study of strongly interacting matter under extreme conditions. In ultra-relativistic nucleus-nucleus collisions, a deconfined, thermalised state of strongly interacting matter, the Quark-Gluon Plasma (QGP), is expected to be formed [9, 10]. This hot and dense phase of QCD matter permeated the early universe in the first few microseconds, according to the standard Big Bang model. Among the four major experiments at the LHC, the Large Ion Collider Experiment (ALICE) is dedicated to the study of heavy-ion collisions. A variety of rare probes is investigated, including quarkonia, heavy-flavour hadrons, photons and jets. Heavy quarks (charm, beauty) are produced at an early stage in heavy-ion collisions and thus provide access to the QGP properties through their interaction with the medium. The study of heavy-quark production at low momentum is of particular importance to address the question, to which extent heavy quarks might be thermalised and take part in the collective behaviour of the strongly interacting medium.

Experimental access to heavy quarks is given via the detection of hadrons containing charm or beauty. A large fraction of the produced charm hadronises into various D meson species, which consist of one charm quark and one of the light quarks up, down or strange. D mesons decay before reaching active detector material and must be reconstructed via their decay products. When an invariant mass analysis in hadronic decay channels is

performed, the full kinematic information of the heavy-flavour hadron is retained. The high spatial resolution provided by the combined tracking of the ALICE Inner Tracking System and the Time Projection Chamber enable the reconstruction of secondary decay vertices of D mesons with intermediate-to-high momenta, which are typically displaced from the primary vertex by a few hundred  $\mu\text{m}$ . D mesons can thus be very efficiently distinguished from background by a selection on the decay topology. Using this analysis strategy, the ALICE collaboration published a series of results for D-meson production at central rapidity. These include the transverse momentum ( $p_{\text{T}}$ ) spectra for different D-meson species in pp collisions at  $\sqrt{s} = 7 \text{ TeV}$  and  $\sqrt{s} = 2.76 \text{ TeV}$  [11–13] and D-meson suppression and flow in Pb–Pb collisions at  $\sqrt{s_{\text{NN}}} = 2.76 \text{ TeV}$  [14–16].

While performing efficiently at high  $p_{\text{T}}$ , the topological selection of D mesons is bound to fail at low  $p_{\text{T}}$ , where the small Lorentz boost can no longer be resolved with the detector and, consequently, the selection efficiency drops very sharply. All of the D meson results currently published by the ALICE collaboration are therefore limited to  $p_{\text{T}} > 1 \text{ GeV}/c$  in pp collisions and  $p_{\text{T}} > 2 \text{ GeV}/c$  in Pb–Pb collisions with increasing uncertainty towards this low- $p_{\text{T}}$  limit.

Despite the experimental challenge, it is of great interest to extend the measurements to zero transverse momentum. Fixed Order plus Next-to-Leading Logarithms (FONLL) calculations [17] predict that over 50 % of the  $\text{D}^0$  yield lies below  $2 \text{ GeV}/c$  in pp collisions. The low- $p_{\text{T}}$  region is therefore crucial for a precise determination of the total charm production cross section at mid-rapidity, which is of substantial importance for the interpretation of charmonium production in QGP studies at the LHC [18, 19]. Up until now, the best ALICE measurement of the charm production cross section at mid-rapidity still relies on an extrapolation to zero transverse momentum based on theory input with rather large uncertainties [12]. Moreover, the low- $p_{\text{T}}$  measurement of charm production in pp collisions is important as a baseline to study the low-momentum phenomenology of charm quarks in nucleus-nucleus collisions.

This thesis presents the first measurement of D-meson production in pp collisions down to zero transverse momentum with ALICE. The studied system comprises  $\text{D}^0$  mesons and their antiparticles by means of the reconstructed decay  $\text{D}^0 \rightarrow \text{K}^- \pi^+$  and its charge conjugate. In order to keep a high efficiency in the low- $p_{\text{T}}$  region, it is necessary to give up the topological selection. The challenge of how to deal with the large combinatorial

background from primary pion and kaon production then arises. This background peaks in a similar kinematic region to that populated by kaons and pions originating from  $D^0$  decays in the low- $p_T$  regime. After exploiting the excellent particle identification (PID) capabilities of ALICE, the remaining signal-to-background ratio is still  $10^{-3}$  in the  $p_T$  interval  $0 < p_T < 1 \text{ GeV}/c$ , impeding the extraction of a stable signal in the invariant mass. The subtraction of an estimate of the combinatorial background improves the stability of the signal extraction. Background estimates are obtained from data, using the like-sign technique. After background subtraction, the  $D^0$  signal can be extracted down to zero transverse momentum.

The analysis strategy applied in this work is similar to that used by the Solenoidal Tracker at RHIC (STAR) collaboration at the Relativistic Heavy-Ion Collider (RHIC) for their measurement of  $D^0$  and  $D^*$  production in pp collisions at  $\sqrt{s} = 200 \text{ GeV}$  [20] and gold-gold (Au-Au) collisions at  $\sqrt{s_{NN}} = 200 \text{ GeV}$  [21]. Due to the lack of a high-precision vertex detector at the time of the STAR measurement, the topological approach to D-meson reconstruction was not available. The measurements are therefore based on background-subtraction techniques, such as like sign, track rotation and event mixing. The recent installation of a Heavy Flavor Tracker will allow for the topological reconstruction of heavy-flavour hadrons with STAR in the near future [22].

This thesis is structured as follows. Chapter 2 presents the theoretical and experimental background of D-meson production in hadronic collisions. After a short description of ALICE in chapter 3, chapter 4 offers details on the  $D^0$  decay. Chapter 5 presents the data analysis in detail. A discussion of the uncertainties in chapter 6 is followed by the results in chapter 7. The thesis concludes in chapter 8.

# D-MESON PRODUCTION IN HADRONIC COLLISIONS

---

This chapter introduces the basic theoretical and experimental concepts in order to put D-meson production in proton-proton and heavy-ion collisions into context.

## 2.1 Key Features of Quantum Chromodynamics

Quantum Chromodynamics (QCD) is one of the pillars of the Standard Model of Particle Physics. It describes the strong interaction between colour-charged quarks and gluons, with the latter being the gauge bosons of the theory. Unlike in Quantum Electrodynamics (QED), where the force carrier is a neutral photon, gluons carry colour charge and are thus subject to interactions with one another. This gauge boson self-interaction is manifest in the non-abelian nature of the underlying symmetry group, which is the  $SU(3)$  component of the Standard Model gauge group  $SU(3) \times SU(2) \times U(1)$ . Non-zero commutators of the 8 generators of  $SU(3)$  in the fundamental representation lead to terms in the gluon field kinematic part of the Lagrangian that correspond to vertices with three or four gluons. This particular structure is responsible for some characteristic features of QCD, which are described in the following.

Figure 2.1 shows the energy dependence of the renormalised ‘running’ coupling constant  $\alpha_s$ . Data points from various experiments at different energy scales or momentum transfer  $Q$  are displayed. At low  $Q$ , corresponding to a large spatial range of the interaction, the

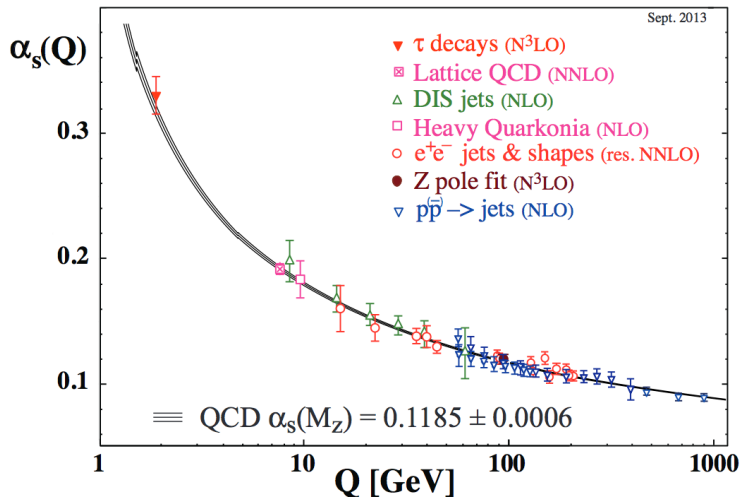


Figure 2.1: The ‘running’ of the strong coupling constant  $\alpha_s$  as a function of the energy scale  $Q$ . Data points originating from a variety of experiments are displayed. This figure was taken from [23].

coupling becomes large, whereas at high  $Q$ , corresponding to small distances, the coupling approaches zero. At sufficiently high energy, quarks become quasi-free. This property of QCD is known as asymptotic freedom [24, 25]. The high-energy behaviour of QCD is opposite to that of QED, where the coupling constant  $\alpha_{EM}$  rises with the energy scale, until the theory encounters infinities in the form of a Landau pole.

Hard QCD processes can be described by perturbative QCD (pQCD) calculations due to the small coupling strength at high energy. The solution of the renormalisation group equation in the leading-order approximation of a perturbative calculation yields the following renormalised coupling constant:

$$\alpha_s(Q^2) = \frac{12\pi}{(33 - 2N_f) \log(Q^2/\Lambda_{QCD}^2)}. \quad (2.1)$$

In this formula,  $N_f$  denotes the number of participating quark flavours and  $\Lambda_{QCD}$  is a parameter that marks the energy scale at which the strong coupling diverges. Perturbative QCD calculations are thus only feasible for energy scales significantly above  $\Lambda_{QCD}$ . Its numerical value is about 200 MeV [23], corresponding to an interaction distance of 1 fm - the typical length scale of nuclear matter. For soft processes, the perturbative approach fails and it becomes difficult to make quantitative predictions. Nowadays, the most

promising approach to working in the soft QCD regime is a numerical scheme on a discretised space-time grid known as Lattice QCD [26].

Phenomenologically, the opposing energy dependence of the QCD and QED couplings can be understood in terms of a screening or anti-screening effect of the respective charge. Vacuum polarisation leads to an effectively reduced coupling strength between electric charges that are being separated. This effect is referred to as screening. Self-interacting gluons establish an anti-screening effect between colour charges that are being separated, meaning that the coupling strength increases. The phenomenological picture can be extended such that the gluons between two colour charges form a narrow string tube of high tension, preventing the colour charges from being separated completely. This concept is known as colour confinement. It states that colour charges must form colour-neutral objects and do not exist freely. In particular, quarks are always bound in hadrons.

Confinement is reflected in an additional linear term in the QCD potential between two colour charges forming together a colour-neutral state. In the case of a quark-antiquark pair, for example, the potential takes the form:

$$V(r) = -\frac{4}{3} \frac{\alpha_s(r)}{r} + \kappa r. \quad (2.2)$$

The first term represents a Coulomb-like interaction, which dominates at short ranges  $r$ . The factor  $-4/3$  is called the colour factor and depends on the particle types that interact. The second term dominates at large distance. It can be seen as the potential energy of a gluon string between the quark and the antiquark with the string constant  $\kappa$ . It becomes apparent that a total separation of the quark and antiquark would require infinite energy and thus cannot be accomplished. Instead the gluon string would eventually break up and form additional quark pairs until colour-neutral hadrons are formed in the process of hadronisation. While QCD still lacks a formal proof of confinement [27], the concept remains a postulate, based on the fact that free quarks have not yet been observed in nature.

## 2.2 Exploring the QCD Phase Diagram

Figure 2.2 shows a sketch of the QCD phase diagram, as it is understood by current research, in terms of temperature and net baryon density. The latter is closely related

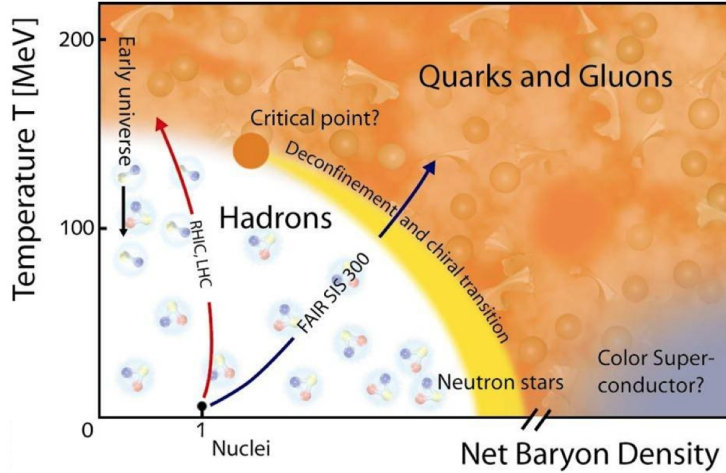


Figure 2.2: Sketch of a possible QCD phase diagram, as illustrated by the Compressed Baryonic Matter (CBM) collaboration [28].

to the baryochemical potential. Two main regimes can be identified: ordinary hadronic matter at low temperature or low baryon density; and the Quark Gluon Plasma (QGP) at high temperature or high baryon density. The QGP is a deconfined state of matter, the properties of which are determined by the degrees of freedom of single quarks and gluons [9, 10]. Moreover, the QGP is characterised by the restoration of chiral symmetry [29]. The critical temperature  $T_c$  marks the transition between the two phases at zero baryochemical potential. Its value is currently estimated to be about  $T_c = 160 \text{ MeV}$  [9, 10]. At low temperature and high density, a new phase of colour superconductivity is predicted [30]. However, this region of the phase diagram is not yet covered by experiments and predictions are very difficult to make.

It is one of the goals of heavy-ion physics to explore the different phases and transitions of the QCD phase diagram. Different experiments are hereby sensitive to different paths, such as those indicated by arrows in fig. 2.2. High-energy particle colliders like the RHIC and the LHC explore the regime of low baryochemical potential, while the future experiments at the Facility for Antiproton and Ion Research (FAIR), which is currently being built at the GSI Helmholtz Centre for Heavy Ion Research, are designed to explore the regions of higher baryochemical potential at lower energy.

The QGP phase of strongly interacting matter is expected to be created in high-energy nucleus-nucleus collisions. In the standard picture, an ultra-relativistic heavy-ion collision

experiences the following stages. The pre-equilibrium phase immediately after the collision is characterised by hard scatterings of partons in the colliding nuclei. After a thermalisation time of about  $\tau = 1 \text{ fm}/c = 3.3 \times 10^{-24} \text{ s}$ , the QGP is formed. High pressure gradients subsequently drive a collective expansion of the medium, which can be described by hydrodynamical modelling [31]. During the expansion, the fireball cools down until the medium undergoes a phase transition and hadrons are formed. At chemical freeze-out, the relative abundances of the created particle species are fixed. Afterwards, hadrons are allowed to re-scatter, until particle momenta are fixed by the time of the kinetic freeze-out. The free streaming particles then reach the detector.

## 2.3 Heavy Quarks in the QGP

Throughout this thesis, the term ‘heavy quark’ encompasses the charm and the beauty quarks, which have masses of  $m_c \approx 1.3 \text{ GeV}/c^2$  and  $m_b \approx 4.2 \text{ GeV}/c^2$  [23]. The top quark, with a mass of  $m_t \approx 173 \text{ GeV}/c^2$ , is not considered for reasons explained further down.

Heavy quarks are produced at an early stage in heavy-ion collisions, before the QGP is formed. The production time scale is of the order of  $\frac{1}{2m}$ , where  $m$  is the mass of the heavy quark. In contrast to the light quarks, their total mass is dominated by the coupling to the Higgs field, as illustrated in fig. 2.3. Consequently, heavy quarks keep their large mass even when chiral symmetry is restored. Since the charm and beauty masses are much larger than the QGP temperature,  $m_c, m_b \gg T_{\text{QGP}}$ , the thermal production of heavy quarks in the medium can be neglected at LHC energies. The annihilation rate of heavy-quark pairs is also negligible [32]. In summary, it can be stated that heavy flavour is approximately conserved during the evolution of the system, which makes heavy quarks calibrated probes of the QGP medium properties.

In contrast to charm and beauty quarks, top quarks decay on a very short time scale of  $1.3 \times 10^{-24} \text{ s}$  [23] due to the large available phase space. All produced top quarks have therefore already decayed before they can interact with the equilibrated medium (cf. previous section). Consequently, they can not be used to probe the QGP. Furthermore, top pair production is very rare. With a production cross section of about 200 pb in pp collisions at  $\sqrt{s} = 7 \text{ TeV}$  [34, 35], only one top event in the entire data set of  $5.25 \text{ nb}^{-1}$

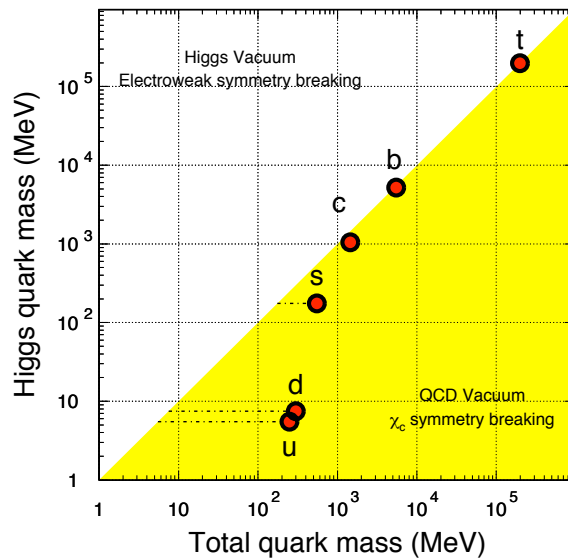


Figure 2.3: Generation mechanisms of quark masses. Charm (c), beauty (b) and top (t) quarks acquire their mass almost entirely by the coupling to the Higgs field. This figure was taken from [33].

used in this work is expected. Top pair creation is studied at the LHC with the ATLAS and CMS detectors, using triggers that allow them to scan pp collisions at much higher event rates.

Experimental access to heavy quarks is made possible via the detection of hadrons containing charm or beauty. Figure 2.4 shows the relative abundances of charmed hadrons in pp collisions. About 1.5% of the produced charm hadronises to charmonium (quark content  $c\bar{c}$ ), 9.4% to the  $\Lambda_c^+$  baryon (quark content  $udc$ ) and the rest to various D-meson ground and excited states. The masses and lifetimes of  $D^0$ ,  $D^+$ ,  $D_s^+$ ,  $D^*(2007)^0$  and  $D^*(2010)^+$  are listed in table 2.1 along with selected decay channels and their respective branching ratios. The D-meson excited states decay rapidly to neutral and charged ground states by means of the strong interaction. The  $D^*(2007)^0$  decays exclusively to  $D^0 + X$ , where X is a  $\pi^0$  or  $\gamma$  (cf. table 2.1). The  $D^*(2010)^+$  decays with a fraction of 67.7% to  $D^0 + \pi^+$  and with a fraction of 30.7% to  $D^+ + \pi^0$ . In fig. 2.4, the respective fraction of excited states decaying to  $D^0$  ( $D^+$ ) is coloured in blue (red). A D meson that is directly produced from a charm quark or in the decay of a charmed resonance is referred to as a ‘prompt’ D meson throughout the thesis. The fraction of prompt  $D^0$

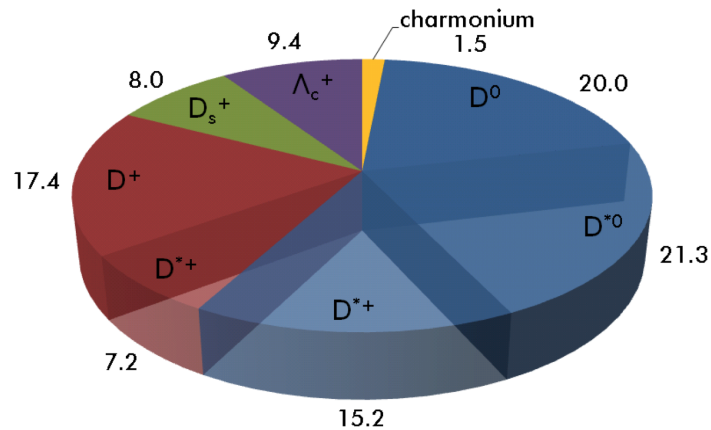


Figure 2.4: Relative abundances of charmed hadrons in pp collisions. The fraction of the first excited states  $D^*(2007)^0$  and  $D^*(2010)^+$  further decaying to  $D^0$  ( $D^+$ ) is marked in blue (red). This figure was taken from [36].

relative to the number of prompt charm quarks is  $0.557 \pm 0.023$ , corresponding to the total blue area in fig. 2.4.

The ALICE collaboration currently pursues three independent strategies for the analysis of heavy-flavour hadrons in pp, Pb–Pb and p–Pb collisions at the LHC. The first two consist of analysing semileptonic decay channels, containing either a single muon or a single electron in the final state. The production of muons from heavy-flavour hadron decays is studied with the ALICE muon spectrometer at forward rapidity [37, 38]. The production of heavy-flavour electrons is measured based on PID information provided by the TPC, TOF, TRD and EMCAL [39]. Another possibility is to exploit the fact that electrons from heavy-flavour decays have a non-zero impact parameter (i.e. distance of the track from the primary vertex) due to the non-zero decay length of the heavy-flavour hadron. Using this method, a statistical separation of charm and beauty via their different impact parameter distributions can be performed, allowing for a separate measurement of electrons from beauty-hadron decays [40, 41]. The semileptonic decay channels come with the advantage of large branching ratios and thus large available statistics. However, lepton flavour conservation enforces the presence of a neutrino, which is undetectable. Therefore, the kinematic information of the original heavy-flavour hadron is always partially lost in the reconstruction.

The third strategy for heavy-flavour measurements is the full reconstruction of purely

meson	mass (MeV/ $c^2$ )	$c\tau$ ( $\mu\text{m}$ )	$\{\Gamma$ (keV) $\}$	decay channel	$\mathcal{B}(\%)$
$D^0$	$1864.84 \pm 0.07$	$123.03 \pm 0.45$		$K^- \pi^+$	$3.88 \pm 0.05$
				$K^+ \pi^-$	$(1.380 \pm 0.028) \times 10^{-4}$
$D^+$	$1869.61 \pm 0.10$	$312.00 \pm 2.1$		$K^- \pi^+ \pi^+$	$9.13 \pm 0.19$
$D_s^+$	$1968.30 \pm 0.11$	$150.00 \pm 2.1$		$\phi(K^- K^+) \pi^+$	$2.24 \pm 0.10$
$D^*(2007)^0$	$2006.96 \pm 0.10$	$\{< 2100\}$		$D^0 \pi^0$	$61.9 \pm 2.9$
				$D^0 \gamma$	$38.1 \pm 2.9$
$D^*(2010)^+$	$2010.26 \pm 0.07$	$\{83.4 \pm 1.8\}$		$D^0 \pi^+$	$67.7 \pm 0.5$
				$D^0(K^- \pi^+) \pi^+$	$2.63 \pm 0.04$
				$D^+ \pi^0$	$30.7 \pm 0.5$

Table 2.1: Properties of charmed mesons and their most abundant first excited states. For the short-lived  $D^*(2007)^0$  and  $D^*(2010)^+$  the natural line width  $\Gamma$  is given instead of the mean lifetime  $c\tau$ . The framed decay modes are analysed in ALICE for the reconstruction of the respective D-meson species. The listed values and uncertainties were taken from [23].

hadronic decay channels via invariant mass analysis. In this case, the full kinematic information is retained. The current analysis efforts concentrate on D mesons, as the full kinematic reconstruction of B mesons was not yet feasible with ALICE based on the available data sets. The cross section of charm-pair production in pp collisions at the LHC is about 20 times larger than that of beauty-pair production [42]. D mesons are consequently more abundant than B mesons and therefore easier to measure.

The D-meson species  $D^0$ ,  $D^+$ ,  $D_s^+$  and  $D^*(2010)^+$  are reconstructed in pp, p-Pb and Pb-Pb collisions with ALICE using the topological approach that was introduced in chapter 1 [11–16]. The selected decay channel for each of the reconstructed species is framed in the corresponding column of table 2.1. The choice of a specific decay channel is based on the size of the branching fraction and on the feasibility of the decay reconstruction. In this respect, the ‘golden channel’ is  $D^0 \rightarrow K^- \pi^+$ , as the final state comprises only two particles. The possible combinations for background candidates are thus restricted as compared to the decay channels of the other D mesons, which require the detection of three particles. Accordingly, the  $D^0 \rightarrow K^- \pi^+$  decay mode is chosen for the new analysis presented in this thesis.

## 2.4 Open Charm and Charmonium

Charmed hadrons that contain exactly one charm or anti-charm quark, i.e. mainly D mesons and the  $\Lambda_c^+$  baryon, are often referred to as ‘open charm’. In contrast, bound states of one charm and one anti-charm quark are known as charmonium. A variety of charmonium states exist that differ in quantum numbers and binding energy. For an extensive review of the physics of charmonium spectroscopy see [43] or [44]. For the field of ultra-relativistic heavy-ion physics, the most relevant charmonium state is the vector ground state,  $J/\psi$ , as it is produced in relatively large abundance and can be directly measured via its decay into  $e^+e^-$  or  $\mu^+\mu^-$  with a branching ratio of about 6% each [23].

The detection of charmonium has played a central role in heavy-ion physics since its possible suppression in heavy-ion collisions was proposed as a direct observable for deconfinement [45]. The original concept assumes that charmonium is produced in initial hard scattering processes and is subsequently destroyed in the possibly deconfined medium via a process known as colour screening. It is assumed that this ‘melting’ of charmonium occurs above the Debye temperature  $T_D$ , which depends on the binding energy of the respective state. This implies that excited states are melted at lower temperatures than the ground state. The possible observation of a hierarchy in the suppression of different charmonium states, also referred to as ‘sequential melting’, was therefore proposed as a proxy for the QGP temperature [46].

The modern picture of charmonium production in ultra-relativistic heavy-ion collisions is more refined and takes into account non-primordial production during the evolution of the medium or at the phase boundary. In the Statistical Hadronisation Model [18], it is assumed that charmonium is exclusively produced at the phase boundary. In such a scenario, the production of charmonium is then governed by the total number of charm quarks available for thermal hadron formation. An important premise is that charm quarks are formed in initial hard scatterings and their total number is approximately conserved during the evolution of the system [32]. Transport models comprise the second main scenario for charmonium production in relativistic heavy-ion collisions [19]. These models account for a continuous generation and destruction of charmonium throughout the evolution of the system.

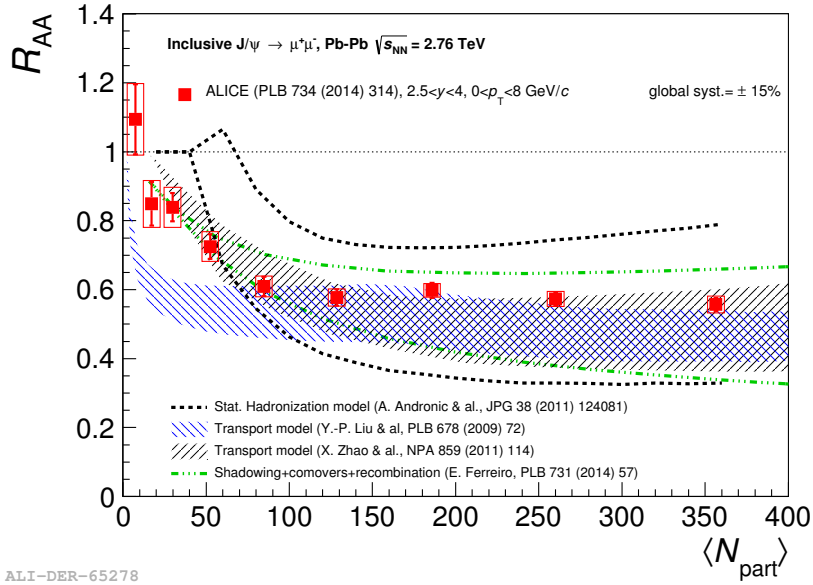


Figure 2.5:  $J/\psi$  suppression in Pb–Pb collisions at  $\sqrt{s_{\text{NN}}} = 2.76$  TeV vs.  $N_{\text{part}}$ . A recent ALICE measurement in the  $\mu^+\mu^-$  decay channel [47] is displayed along with theoretical predictions from different models [48–50]. The large uncertainties of the models are due to the uncertainty on the charm production cross section, which enters quadratically as a model parameter. This figure was derived from [47].

The experimental observable to quantify medium effects like suppression or enhancement is the nuclear modification factor  $R_{\text{AA}}^{J/\psi}$ . It is defined as the ratio of the  $J/\psi$  yield in nucleus-nucleus (AA) collisions to the yield in pp collisions, scaled up by the average number of binary collisions  $\langle N_{\text{coll}} \rangle$ :

$$R_{\text{AA}}^{J/\psi} = \frac{dN_{J/\psi}^{\text{AA}}/dy}{\langle N_{\text{coll}} \rangle \cdot dN_{J/\psi}^{\text{pp}}/dy}. \quad (2.3)$$

Figure 2.5 presents the  $J/\psi$  nuclear modification factor in Pb–Pb collisions at  $\sqrt{s_{\text{NN}}} = 2.76$  TeV as a function of the number of nucleons participating in the collision,  $N_{\text{part}}$ . A recent measurement in the  $\mu^+\mu^-$  decay channel with the ALICE muon spectrometer at forward rapidity [47] is displayed along with the theoretical predictions from the Statistical Hadronisation Model [48] and two transport models [49, 50].

From this example, it can be seen that the measurement is considerably more precise than the theory. The large uncertainties in the models are due to the large uncertainties of

the total charm cross section,  $d\sigma^{c\bar{c}}/dy$ , which is required as an input parameter for both types of models. In the case of the Statistical Hadronisation Model,  $d\sigma^{c\bar{c}}/dy$  is actually the only free parameter. Furthermore, as two charm quarks are needed to form a  $J/\psi$  meson,  $d\sigma^{c\bar{c}}/dy$  enters quadratically into the  $J/\psi$  yield calculation. A better precision of the measurement of  $d\sigma^{c\bar{c}}/dy$  will therefore significantly contribute to the understanding of charmonium production in nucleus-nucleus collisions.

## 2.5 Theoretical Predictions for Heavy-Flavour Production

The production cross section of a heavy-flavour meson in pp collisions can be calculated by splitting the calculation into a perturbative and a non-perturbative part. This technique is known as the factorisation approach. It consists of a convolution of the perturbative cross section of heavy-quark pair production with a non-perturbative fragmentation function that parameterises the relative abundance and momentum distribution of the heavy-flavour hadron:

$$d\sigma_{pp \rightarrow H_Q X} = d\sigma_{pp \rightarrow Q\bar{Q}X} \otimes D_{Q\bar{Q} \rightarrow H_Q}^{\text{NP}}. \quad (2.4)$$

Here,  $H_Q$  is the produced heavy-flavour meson and heavy (anti)quarks are denoted as  $Q$  ( $\bar{Q}$ ). The cross section for heavy-quark pair production from two colliding protons, i.e. the first term in eq. (2.4), can be reduced to a sum of elementary processes as follows:

$$d\sigma_{pp \rightarrow Q\bar{Q}X} = \sum_{i,j} \int dx_1 \int dx_2 F^i(x_1, \mu_F^2) F^j(x_2, \mu_F^2) d\sigma_{ij \rightarrow Q\bar{Q}X}(p_1, p_2, \mu_R^2, \mu_F^2). \quad (2.5)$$

This formula involves the cross sections  $d\sigma_{ij \rightarrow Q\bar{Q}X}$  for the interaction of single partons  $i$  and  $j$  that can be computed by the means of a perturbative series in the strong coupling constant. The formula further includes the parton distribution functions (PDFs),  $F^i(x_k, \mu_F^2)$  with  $k \in 1, 2$ , which denote the probability density of the parton  $i$  to carry the momentum  $p_k = x_k P_k$ , where  $P_k$  is the respective proton momentum. The parton distribution functions and the partonic cross sections depend on the factorisation and renormalisation scale parameters  $\mu_F$  and  $\mu_R$ .

The lowest order in the perturbative expansion for the calculation of the elementary

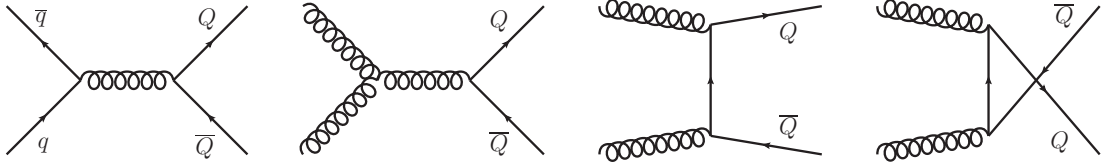


Figure 2.6: Feynman diagrams of the leading-order (LO) processes of heavy-flavour pair production. Quarks are denoted with a straight line labelled with  $q$  ( $\bar{q}$ ) for light (anti)quarks and  $Q$  ( $\bar{Q}$ ) for heavy (anti)quarks. Gluons are represented by curly lines.

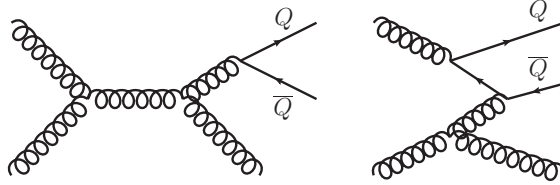


Figure 2.7: Feynman diagrams of two contributions to the heavy-quark pair production cross section at next-to-leading order (NLO). The process depicted on the left is called gluon splitting, the process on the right flavour excitation. The diagrams are labelled as in fig. 2.6.

processes is known as the leading order (LO). The possible hard scattering processes at LO are quark-antiquark annihilation  $q+\bar{q} \rightarrow Q+\bar{Q}$  and gluon-gluon fusion  $g+g \rightarrow Q+\bar{Q}$ . The corresponding Feynman diagrams can be found in fig. 2.6. As the diagrams contain two vertices, the leading order is in  $\alpha_s^2$ . Gluon fusion is the dominant production mechanism for heavy-quark pairs at the LHC.

A large variety of basic processes contribute to the next-to-leading order (NLO) in  $\alpha_s^3$ . Two examples are gluon splitting and flavour excitation, the Feynman diagrams of which are displayed in fig. 2.7. Next-to-leading order calculations of heavy-flavour production yield realistic results for transverse momenta at the order of the heavy-quark mass, see e.g. [51]. However, NLO calculations contain logarithmic terms in  $p_T/m$  that spoil the convergence of the expansion for  $p_T \gg m$ . These terms are categorised as leading logarithmic terms (LL), next-to-leading logarithmic terms (NLL) and so on. The convergence of the expansion can be recovered for high  $p_T$  using the fragmentation-function formalism [52]. Since this is a massless formulation, however, it does not work properly in the regime where  $p_T$  is of the order of the heavy quark mass.

The Fixed Order plus Next-to-Leading Logarithms (FONLL) framework [17] solves

	default value	variations
$m_c$ (GeV/c <sup>2</sup> )	1.5	1.3, 1.7
$m_b$ (GeV/c <sup>2</sup> )	4.75	4.5, 5
$\mu_R, \mu_F$	$\mu_0 = \sqrt{p_T^2 + m^2}$	$0.5 \leq \mu_{R,F}/\mu_0 \leq 2$ with $0.5 \leq \mu_R/\mu_F \leq 2$

Table 2.2: Parameters included in FONLL calculations of heavy-flavour production [56]. The listed variations of the default values are used to estimate the systematic uncertainty.

this issue in combining fixed order NLO calculations with the fragmentation function formalism, correctly taking into account the LO, NLO, LL and NLL terms. Thus FONLL provides a valid description of heavy flavour production from low to high  $p_T$ . The calculations need to be provided with a PDF set and parameterised fragmentation functions as an input. They contain as parameters the charm (or beauty) mass and the renormalisation and factorisation scale parameters  $\mu_R$  and  $\mu_F$ . FONLL calculations for heavy-quark production in pp collisions at different collider energies are available on a public website [53]. A central value and an uncertainty band are quoted in the output. The central values for the parameters are listed in table 2.2, along with the ranges that were used to estimate the uncertainty. The employed PDF set for the central values is CTEQ6.6 [54]. The uncertainty due to the PDF set is estimated as in [55].

The left panel of fig. 2.8 displays the  $p_T$ -differential  $D^0$  production cross section at mid-rapidity,  $|y| < 0.5$ , in pp collisions at  $\sqrt{s} = 7$  TeV, obtained with FONLL calculations [56]. The blue solid line represents the central value and the blue band the uncertainty. The theoretical uncertainties are sizeable, in particular in the low- $p_T$  range and span up to an order of magnitude. The right panel of fig. 2.8 shows the cumulative FONLL cross section normalised by the integral from zero to infinity at  $y = 0$ . The plot can thus be interpreted as the  $D^0$  yield fraction below a given transverse momentum. As indicated by the red dotted line, more than 50 % of the yield lies below 2 GeV/ $c$  and about 20 % of the yield lies below 1 GeV/ $c$ . The low- $p_T$  region is thus crucial for a precise determination of the  $p_T$ -integrated charm production cross section. The topological selection of D mesons is limited to transverse momenta above about 1 GeV/ $c$ , as will be detailed in section 4.2.3. A fraction of about 20 % of the  $D^0$  yield is thus not accessible with the topological method and the cross section must be extrapolated down to zero transverse momentum based

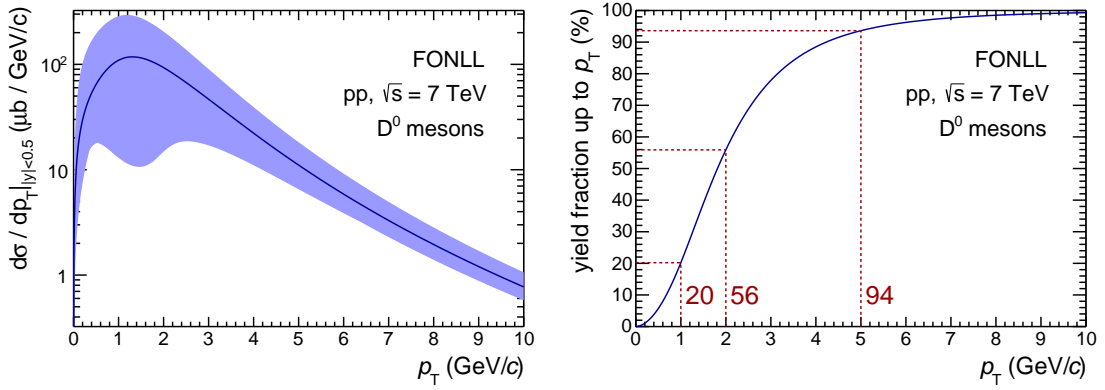


Figure 2.8: FONLL prediction of the  $p_T$ -differential  $D^0$  production cross section at  $|y| < 0.5$  in pp collisions at  $\sqrt{s} = 7$  TeV (left) and cumulative yield fraction up to a given  $p_T$  in percent (right). More than 50% of the  $D^0$  yield is predicted to lie below 2  $\text{GeV}/c$ . The values were taken from [56].

on theory input. Such an extrapolation is associated with large uncertainties, as can be seen in fig. 2.8.

In this work, FONLL predictions for charm and beauty production are used to estimate the feed-down fraction of  $D^0$  from B decays in the  $D^0$  yield (section 5.8) and for a comparison with the measured  $p_T$  spectrum of  $D^0$  production (chapter 7).

# ALICE AT THE LHC

---

This chapter introduces ALICE in the context of the physics programme of the Large Hadron Collider (LHC) and describes the detectors of ALICE that are important for this thesis.

## 3.1 LHC Experiments and Physics Programme

The LHC [57] provides hadron collisions to four major experiments. A Toroidal LHC Apparatus (ATLAS) [58] and the Compact Muon Solenoid (CMS) [59] are two general purpose detectors, currently focussing on the investigation of the Higgs boson and the search for new physics beyond the Standard Model, mainly in pp collisions. ATLAS and CMS essentially share the same physics programme, allowing for the cross check of important results by two independent collaborations – a concept that has already been proven successful for the Higgs discovery. The Large Hadron Collider Beauty (LHCb) experiment [60] is specialised in physics involving beauty quarks, for example the investigation of CP violation in B meson oscillations.

Whereas ATLAS, CMS and LHCb primarily focus on the investigation of pp collisions, A Large Ion Collider Experiment (ALICE) [61] is dedicated to the heavy-ion programme at the LHC. The detector is therefore optimised to meet the specific challenges that arise from the high multiplicity environment created in central Pb-Pb collisions. The Time Projection Chamber, which is the main tracking device of ALICE, can handle particle densities up to  $dN/dy = 8000$  [61]. A low material budget, a moderate magnetic field of

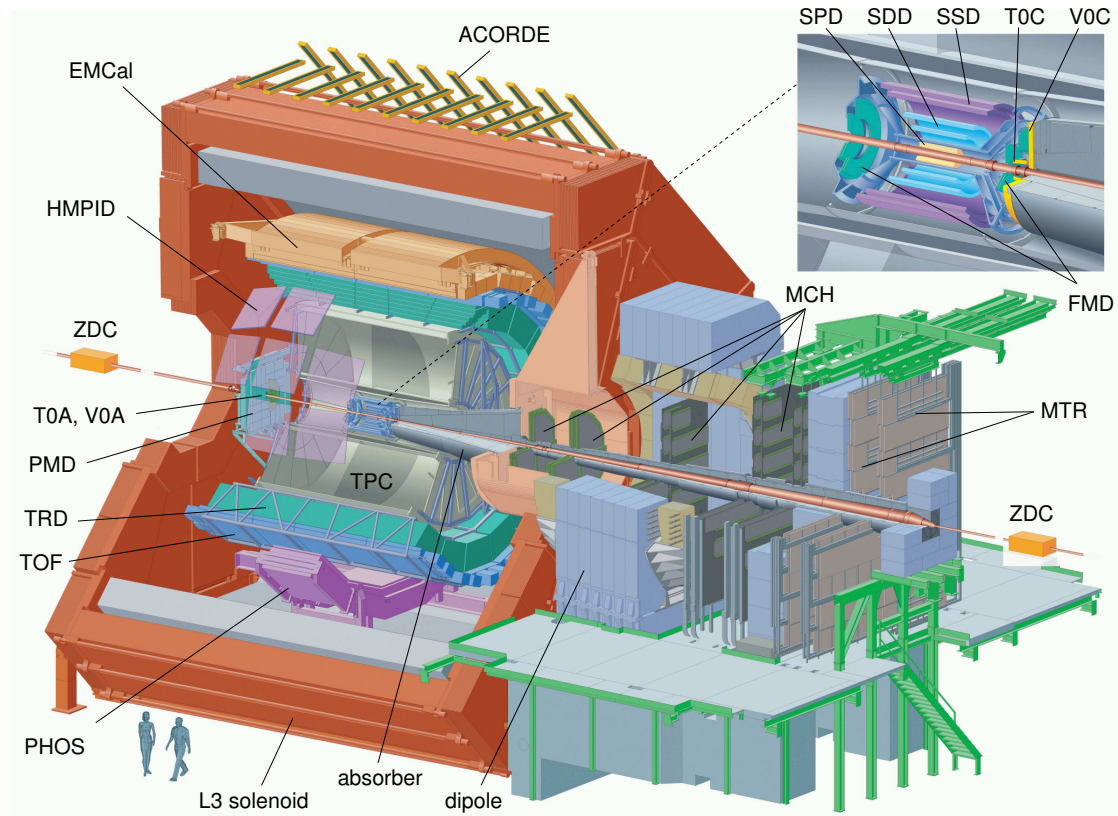


Figure 3.1: Sketch of ALICE with labels for the different subsystems. This figure was taken from [62].

0.5 T and excellent particle identification (PID) capabilities allow for the comprehensive study of particle production down to low momentum.

### 3.2 ALICE Detector Overview

Figure 3.1 shows a sketch of ALICE with labels for the different subsystems. The detector consists of a central barrel for measurements mainly at mid-rapidity and a muon spectrometer for measurements at forward rapidity. From the beamline to the outside, the central barrel hosts the Inner Tracking System (ITS) for tracking and vertex detection; the Time Projection Chamber (TPC) for tracking and particle identification via energy loss  $dE/dx$ ; the Transition Radiation Detector (TRD) for electron identification; and the Time-of-Flight (TOF) system for particle identification by means of a velocity

measurement. ITS, TPC and TOF cover full azimuth and a pseudo-rapidity range of about  $|\eta| < 0.9$ , apart from the first two layers of the ITS that have an extended  $\eta$  coverage. The TRD is currently completed with the missing modules and will be established in full azimuthal coverage in Run II. The Electromagnetic Calorimeter (EMCAL), the Photon Calorimeter (PHOS) and the High Momentum Particle Identification Detector (HMPID) cover only a part in azimuth and in pseudo-rapidity.

A magnetic field of 0.5 T is provided by a solenoidal magnet that was inherited from the L3 experiment at the Large Electron Positron (LEP) collider. Some smaller detectors for event characterisation and triggering are located in the forward rapidity region, close to the beam pipe. In the central barrel, these are the V0 and T0 detectors, the Photon Multiplicity Detector (PMD) and the Forward Multiplicity Detector (FMD). The Zero Degree Calorimeters (ZDC) are located outside the detector at a distance of 116 m at each side of the central interaction point.

Throughout this thesis, the standard ALICE coordinate system is used, if not otherwise stated. The central interaction point in the detector defines the origin of the cartesian coordinate system. The  $z$  axis points along the beamline. Accordingly, the  $xy$  plane is oriented transverse to the beamline and sometimes denoted as the transverse plane. The muon system defines the ‘C-side’ of the detector, the opposite side is called ‘A-side’.

The subsystems of ALICE that are relevant for this work are described in detail in the following sections. A comprehensive description of layout and performance of the detector is given in the Technical Design Report [61] and a recent performance paper [62].

### 3.3 Inner Tracking System

The Inner Tracking System (ITS) provides tracking and identification of charged particles in six cylindrical layers of silicon semiconductor detectors at radii between 3.9 cm and 43.0 cm in coaxial arrangement around the beam pipe. The two innermost layers with a pseudo-rapidity coverage of  $|\eta| < 1.98$  constitute the Silicon Pixel Detector (SPD). With a granularity of  $50 \mu\text{m}$  ( $r\phi$ ) x  $425 \mu\text{m}$  ( $z$ ), it provides a high spatial resolution of  $12 \mu\text{m}$  in  $r\phi$  and of  $100 \mu\text{m}$  in  $z$ . The SPD is followed by two layers of the Silicon Drift Detector (SDD) and two layers of the Silicon Strip Detector (SSD) with a pseudo-rapidity acceptance of  $|\eta| < 0.9$ . The total material budget for a track traversing each layer of

the ITS is only about 8% of a radiation length.

In this analysis, the ITS is used to improve the momentum resolution of particles reconstructed with the TPC and for the precise localisation of primary vertices. Moreover, the SPD contributes a signal to the minimum bias trigger that is used in this analysis. The contribution of the ITS to the combined ITS-TPC tracking system is crucial for the reconstruction of secondary decay vertices and thus for the topological selection of D mesons. This particular functionality of the ITS, however, is not needed in this work, where D mesons are measured without the reconstruction of secondary vertices. Furthermore, the SSD and SDD layers provide energy loss information that can be used for the identification of charged particles. This feature is particularly useful to identify low momentum particles that do not reach the TPC. However, in this analysis, the PID information from the ITS is not used, since the corresponding  $dE/dx$  information from the TPC is more precise and thus preferred.

### 3.4 Time Projection Chamber

The Time Projection Chamber (TPC) is the heart of the central barrel with an essential contribution to most of the ALICE physics analyses. With an inner radius of 85 cm, an outer radius of 250 cm and a length of 500 cm, it is the largest TPC ever built. The TPC provides tracking in a large transverse momentum range, as well as PID information by measuring the specific energy loss of charged particles in the TPC gas. In the period of data taking that is relevant for this thesis, it was operated with a gas mixture of neon, carbon dioxide and nitrogen in the proportions 90/10/5. The drift field is provided by a central electrode at a negative voltage of 100 kV. The produced ionisation electrons are collected at read-out plates on either side of the chamber. The drift time for electrons traversing the full chamber is of about 90  $\mu$ s. The read-out panels are organised in 18 sectors at each side in azimuthal direction and 159 pad rows in radial direction.

For tracks with full radial length that have possible matches in ITS, TOF and TRD, the acceptance is about  $|\eta| < 0.9$ . Tracks with a pseudo-rapidity outside this range are still reconstructed, but suffer from reduced momentum resolution since the track only partially traverses the active volume and the lever arm is shortened. The TPC is designed for the high occupancies that occur in central Pb–Pb collisions. The fast read-out can

manage primary charged particle multiplicities up to  $dN/d\eta = 8000$ , mounting up to about 20000 tracks in the acceptance. The relative  $dE/dx$  resolution in the data set used in this work was measured to be about 5.5% [63], enabling a kaon-pion separation of  $2\sigma$  up to a momentum of about 0.8 GeV/ $c$  and a proton-pion separation of  $2\sigma$  up to a momentum of about 1.6 GeV/ $c$  [62].

The current analysis strongly relies on both the tracking and the particle identification capacities of the TPC.

### 3.5 Time of Flight

The Time-of-Flight (TOF) system provides particle identification via flight-time measurements in an acceptance range of  $|\eta| < 0.88$ . It consists of 1593 Multi-gap Resistive-Plate Chambers (MRPCs), arranged in 18 segments in  $\phi$  and 5 segments in  $z$  direction with a radial distance between 3.7 m and 3.99 m from the beamline. The flight time of a particle is evaluated by taking the difference of the measured arrival time in the TOF system and a reference start time for each event that is provided by the T0 detector. In combination with the track length and the track momentum measured in the TPC, a mass hypothesis for the particle can be calculated. The resolution of particle arrival times in the TOF detector is about 80 ps [64], enabling a kaon-pion separation of  $2\sigma$  up to a momentum of 3 GeV/ $c$  and a proton-pion separation of  $2\sigma$  up to a momentum of 5 GeV/ $c$ . [62].

In this analysis, the TOF information is used in conjunction with the PID information provided by the TPC.

### 3.6 T0

The T0 detector consists of two small arrays of Cherenkov detectors placed at forward rapidity on either side of the interaction point, very close to the beam pipe. The part on the A-side (T0A) covers a pseudo-rapidity of  $4.61 \leq \eta \leq 4.92$ . Due to space constraints on the C-side, T0C had to be placed in front of the muon absorber. It is hence located closer to the nominal interaction point and covers a pseudo-rapidity range of  $-3.28 \leq \eta \leq -2.97$ .

The T0 detector is primarily used to provide a common start time per event to the TOF system. Besides, it contributes the earliest signal to the lowest-level trigger and participates in the luminosity measurement.

### **3.7 V0**

The V0 detector consists of two arrays of scintillator counters, V0A and V0C, placed on both sides of the interaction point, close to the T0 detectors. V0A and V0C cover a pseudo-rapidity of  $2.8 \leq \eta \leq 5.1$  and  $-3.7 \leq \eta \leq -1.7$  respectively.

The V0 detector is used to define various minimum bias (MB) triggers in combination with other sub-detectors. The monotonic increase of the V0 signal amplitudes with the event multiplicity are exploited to classify the multiplicity and, in the case of nucleus-nucleus collisions, the centrality of events. With this functionality, the V0 detector is also employed as a centrality trigger. Furthermore, the combined timing information of V0A and V0C is exploited for the rejection of beam-gas events. The V0 detector is also used as a luminometer.

# THE $D^0$ DECAY

The first part of this chapter presents details about the  $D^0$  decay modes that are relevant for the analysis presented in this thesis. In particular, the notion of Cabibbo suppression is introduced in the context of the decay mode  $D^0 \rightarrow K^+\pi^-$ . In the second part of this chapter, the  $D^0$  decay kinematics is studied, which is essential for various aspects of this thesis.

## 4.1 $D^0$ Decay Modes

In this analysis,  $D^0$  mesons are reconstructed in the  $D^0 \rightarrow K^-\pi^+$  decay channel and its charge conjugate  $\overline{D}^0 \rightarrow K^+\pi^-$ . The specific choice among the many possible decay modes was motivated in chapter 2. All opposite-signed  $K\pi$  pairs are thus considered for the invariant mass analysis. Naturally, also the decay mode  $D^0 \rightarrow K^+\pi^-$  and its

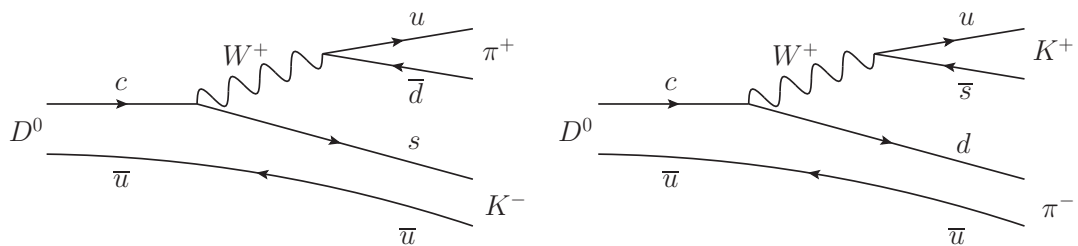


Figure 4.1: Feynman diagrams of the Cabibbo-favoured decay  $D^0 \rightarrow K^-\pi^+$  (left) with a branching ratio of  $(3.88 \pm 0.05)\%$  and the doubly Cabibbo-suppressed decay  $D^0 \rightarrow K^+\pi^-$  (right) with a branching ratio of  $(1.380 \pm 0.028) \times 10^{-2}\%$ .

charge conjugate  $\overline{D}^0 \rightarrow K^- \pi^+$  contribute to the measured  $D^0$  signal, though they are strongly suppressed. Figure 4.1 shows Feynman diagrams of the two processes. During the  $D^0 \rightarrow K^- \pi^+$  decay (left diagram in fig. 4.1), the charm quark from the original  $D^0$  splits into a strange quark and a  $W^+$  that subsequently decays to a  $\overline{u}d$  quark pair forming a  $\pi^+$ . The two flavour changes involved are either within the first or within the second quark family. The transition amplitude consequently contains only diagonal elements of the Cabibbo-Kobayashi-Maskawa (CKM) matrix [65, 66]. In the  $D^0 \rightarrow K^+ \pi^-$  decay, the charm quark changes its flavour to a down quark radiating a  $W^+$  that decays further to a  $u\overline{s}$  quark pair, constituting a  $K^+$  in the final state. A cross-over between different quark-families now occurs in both of these flavour changes. The transition amplitude accordingly contains two off-diagonal elements of the CKM matrix, which are much smaller than the diagonal entries. This effect is known as Cabibbo suppression.  $D^0 \rightarrow K^+ \pi^-$  is doubly Cabibbo-suppressed, whereas  $D^0 \rightarrow K^- \pi^+$  is Cabibbo-favoured.

The Particle Data Group (PDG) currently lists the branching fractions  $(3.88 \pm 0.05) \%$  for  $D^0 \rightarrow K^- \pi^+$  and  $(1.380 \pm 0.028) \times 10^{-4}$  for  $D^0 \rightarrow K^+ \pi^-$  as world average [23]. The ratio of the branching fractions of the Cabibbo-suppressed to the Cabibbo-favoured decay is  $(3.56 \pm 0.06) \times 10^{-3}$ . Though it is hence of little relevance to the analysis results whether the doubly Cabibbo-suppressed decay is taken into account or not, it is straight forward to add the branching ratios of the two contributing decay channels. A total branching ratio of  $\mathcal{B} = (3.89 \pm 0.05) \%$  is consequently used for the calculation of the  $D^0$  cross section (cf. section 5.9).

The PDG values of the branching fractions are subject to small fluctuations due to regular updates from recent measurements. By the time the topological  $D^0$  analysis was published, the PDG value for the branching ratio of  $D^0 \rightarrow K^- \pi^+$  was  $3.87 \%$  [11]. Furthermore, the doubly-Cabibbo suppressed decay channel was not taken into account. The branching ratio used in this analysis is therefore  $0.02 \%$  larger than that used in the topological analysis. The relative difference of about  $0.5 \%$  should be kept in mind, even though it is negligible compared to the uncertainties of the measurements. The inconsistency could in principle be avoided by quoting the branching ratio times cross section as the final result. Meanwhile, the current PDG value of the branching fraction  $\mathcal{B}(D^0 \rightarrow K^- \pi^+)$  is likely to be adjusted again soon, as the CLEO collaboration recently updated their measurement of several D-meson branching ratios in electron-positron collisions at the Cornell Electron Storage Ring (CESR) [67]. They reported an updated

result of  $3.934 \pm 0.021(\text{stat.}) \pm 0.061(\text{syst.})\%$  for  $D^0 \rightarrow K^- \pi^+$ , which constitutes now the most precise single measurement of this particular branching ratio.

In a rare process, known as oscillation, a  $D^0$  can transform to its antiparticle  $\overline{D}^0$  and vice versa before it decays. Such  $D^0$ - $\overline{D}^0$  oscillations were observed recently with the LHCb experiment via a precise decay time dependent measurement of the ratio  $\mathcal{B}(D^0 \rightarrow K^+ \pi^-)/\mathcal{B}(D^0 \rightarrow K^- \pi^+)$  [68]. This measurement is the first significant observation of D-meson oscillations with a single experiment and contains interesting physics of its own. For this analysis, however, possible influences of D-meson oscillations on the invariant mass distributions can be completely neglected.

## 4.2 $D^0$ Decay Kinematics

### 4.2.1 Momentum-Space Variables

This section is intended to provide a collection of important definitions and equations for the kinematic variables that are used in this thesis. In equations in this chapter and throughout the thesis, natural units with  $c = 1$  are used, where  $c$  denotes the speed of light.

In this thesis, the momentum-space variables  $(p_T, y, \phi)$  are used, where  $p_T$  is the transverse momentum, i.e. the momentum projected to the transverse plane,  $\phi$  the azimuthal angle in the transverse plane, and  $y$  the rapidity defined as

$$y = \tanh^{-1} \beta_z = \frac{1}{2} \ln \frac{E + p_z}{E - p_z}. \quad (4.1)$$

Here,  $E$  denotes the energy of the particle and  $\beta_z$  and  $p_z$  the relativistic velocity and the momentum along the  $z$  direction, which corresponds to the beam axis (cf. section 3.2). As defined according to eq. (4.1), rapidity is an additive quantity under Lorentz transformations along the  $z$  direction. For massive particles, the rapidity depends on the mass  $m$  of the particle. Rapidity is thus only a meaningful quantity if the particle type is known. For some applications, it is therefore more convenient to use the pseudo-rapidity

$\eta$  instead, which is independent of the particle species. It is defined as

$$\eta = -\ln \tan \left( \frac{\theta}{2} \right), \quad (4.2)$$

where  $\theta$  is the polar angle between the  $z$  axis and the momentum vector. A flight direction of a particle transverse to the beam axis corresponds to  $\eta = 0$ ; a flight direction at  $\theta = 45^\circ$  corresponds to  $|\eta| \approx 0.88$ ; and a flight direction along the beam axis corresponds to  $|\eta| = \infty$ . The transformation from pseudo-rapidity to rapidity is

$$y = \ln \frac{\sqrt{m^2 + p_T^2} \cosh^2 \eta + p_T \sinh \eta}{\sqrt{m^2 + p_T^2}}. \quad (4.3)$$

Rapidity coincides with pseudo-rapidity for massless particles or in the ultra-relativistic limit  $E \gg m$  for a massive particle. The following inequality for rapidity  $y$  and pseudo-rapidity  $\eta$  always holds:

$$|y| \leq |\eta|. \quad (4.4)$$

The transformation of the momentum coordinates  $(p_T, y, \phi)$  to cartesian momentum coordinates  $(p_x, p_y, p_z)$  is given by

$$p_x = p_T \cos \phi, \quad (4.5)$$

$$p_y = p_T \sin \phi, \quad (4.6)$$

$$p_z = p_T \sinh \eta = m_T \sinh y. \quad (4.7)$$

Here, the transverse mass  $m_T$  is defined as

$$m_T = \sqrt{m^2 + p_T^2}. \quad (4.8)$$

The following expressions for the energy and the absolute value of the momentum as a function of  $p_T$  and  $y$  are also useful:

$$E = m_T \cosh y, \quad (4.9)$$

$$|\vec{p}| = p_T \cosh \eta = \sqrt{(m^2 + p_T^2) \sinh^2 y + p_T^2}. \quad (4.10)$$

### 4.2.2 Invariant Mass

The invariant mass  $M$  of a system of  $N$  particles with four-momenta  $p_i = (E_i, \vec{p}_i)$  is defined as

$$M^2 = \left( \sum_{i=0}^N p_i \right)^2. \quad (4.11)$$

For two particles, the invariant mass can be written in the form

$$M^2 = (p_1 + p_2)^2 = m_1^2 + m_2^2 + 2(E_1 E_2 - |\vec{p}_1| |\vec{p}_2| \cos \theta). \quad (4.12)$$

Using the  $(p_T, y, \phi)$  momentum-space variables, the formula translates to

$$M^2 = m_1^2 + m_2^2 + 2m_{T,1} m_{T,2} \cosh \Delta y - 2p_{T,1} p_{T,2} \cos \Delta \phi \quad (4.13)$$

with the differences in rapidity,  $\Delta y = y_1 - y_2$ , and in the azimuthal angle,  $\Delta \phi = \phi_1 - \phi_2$ , of the two particles and the transverse mass  $m_T$  as defined in eq. (4.8).

### 4.2.3 Decay Length

The decay length is defined as the distance between the production point of a particle, i.e. the primary vertex, and the location where it decays, i.e. the secondary vertex. The decay length of D mesons is the determining parameter for the performance of the measurement of D-meson production via the reconstruction of the decay topology. The efficiency of the background rejection decreases with decreasing decay length. If the decay length is too small, the secondary vertex can no longer be distinguished from the primary vertex and the topological approach for D-meson reconstruction fails. For an evaluation of the experimental limit of the topological approach for the measurement of D mesons towards low  $p_T$ , it is therefore instructive to analyse the dependence of the decay length on kinematic variables and to compare it to the detector resolution.

The average lifetime of a  $D^0$  in its rest frame is about  $\tau_0 = 123 \mu\text{m}/c$  [23]. Performing a Lorentz boost to the lab frame yields for the average decay length

$$L = \beta \gamma \tau_0 = \frac{p}{m} \tau_0, \quad (4.14)$$

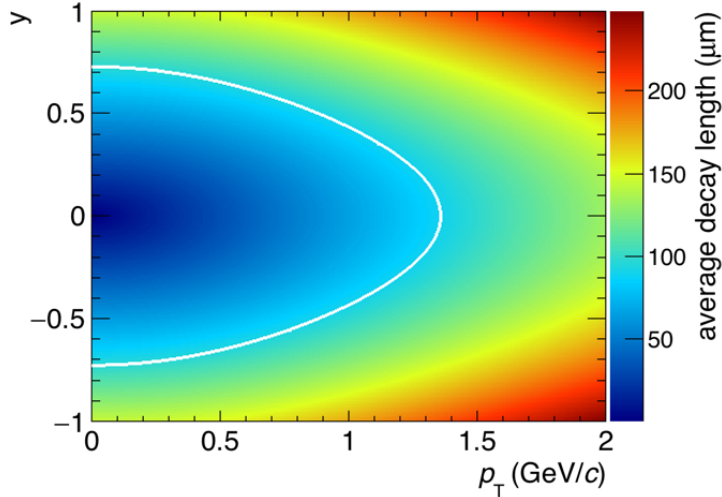


Figure 4.2: Average  $D^0$  decay length in the lab frame as a function of the  $D^0$  transverse momentum and rapidity. The white line marks the resolution limit of about  $80\ \mu\text{m}$  for the separation of the secondary from the primary vertex.

where  $p$  is the absolute value of the momentum and  $m = 1.865\ \text{GeV}/c^2$  the  $D^0$  mass. The average decay length can be expressed as a function of the  $D^0$  rapidity and transverse momentum using eq. (4.10):

$$L = \frac{\tau_0}{m} \sqrt{(m^2 + p_T^2) \sinh^2 y + p_T^2}. \quad (4.15)$$

A plot of this formula in the rapidity range  $|y| < 1$  and in the  $p_T$  range  $0 < p_T < 2\ \text{GeV}/c$  is shown in fig. 4.2. The resolution of the separation of the secondary vertex from the primary vertex is about  $80\ \mu\text{m}$  for a  $D^0$  at zero transverse momentum [11]. The white contour line in fig. 4.2 encloses the phase space region, for which the average  $D^0$  decay length is below this resolution limit of  $80\ \mu\text{m}$ . As this area covers almost the entire phase space for a  $D^0$  with  $p_T < 1\ \text{GeV}/c$  at mid-rapidity  $|y| < 0.8$ , the topological reconstruction of D mesons with ALICE is limited to about  $p_T > 1\ \text{GeV}/c$ .

Figure 4.2 also demonstrates that, profiting from the boost in rapidity, the topological approach can still be applied down to zero transverse momentum using a forward detector. With the LHCb experiment, D-meson production in pp collisions at  $\sqrt{s} = 7\ \text{TeV}$  was measured at forward rapidity in  $2.0 < y < 4.5$  and in the  $p_T$  range  $0 < p_T < 8\ \text{GeV}/c$  [69].

#### 4.2.4 Kinematics of a Two-Body Decay

Consider a general two-body decay, where a mother particle with mass  $M$  decays to two daughter particles with masses  $m_1$  and  $m_2$ , where  $M \geq m_1 + m_2$ . The centre-of-mass frame (CMS) of the system corresponds to the rest frame of the decaying particle. In the CMS, the four-momenta of the involved particles can be written as  $p = (M, 0, 0, 0)$  for the mother particle and  $p_i = (E_i, \vec{p}_i)$ , with  $i \in \{1, 2\}$ , for the daughter particles. Starting from four-momentum conservation

$$p = p_1 + p_2, \quad (4.16)$$

the energies and momenta of the daughter particles in the CMS can be expressed as

$$E_1 = \frac{1}{2M}(M^2 + m_1^2 - m_2^2), \quad (4.17)$$

$$E_2 = \frac{1}{2M}(M^2 + m_2^2 - m_1^2), \quad (4.18)$$

$$|\vec{p}_1| = |\vec{p}_2| = \frac{1}{2M} \sqrt{M^4 + m_1^4 + m_2^4 - 2(M^2 m_1^2 + M^2 m_2^2 + m_1^2 m_2^2)}. \quad (4.19)$$

These expressions are symmetric under the exchange of the two particles, as expected. For the  $D^0 \rightarrow K^- \pi^+$  decay, with the masses of the involved particles,  $m_{D^0} = 1.865 \text{ GeV}/c^2$ ,  $m_{K^-} = 0.494 \text{ GeV}/c^2$  and  $m_{\pi^+} = 0.140 \text{ GeV}/c^2$ , eqs. (4.18) - (4.19) yield for the energies and momenta of the decay products:

$$|\vec{p}_{K^-}| = |\vec{p}_{\pi^+}| = 0.861 \text{ GeV}/c, \quad (4.20)$$

$$E_{K^-} = 0.993 \text{ GeV}, \quad (4.21)$$

$$E_{\pi^+} = 0.873 \text{ GeV}. \quad (4.22)$$

In the CMS, the energy and momentum spectra of the daughter particles are discrete. Boosting the decay kinematics to the lab frame results in continuous spectra for the case of a moving mother particle.

#### 4.2.5 A Toy Monte Carlo for Decay Kinematics

Based on the equations of the last section, the two-body decay  $D^0 \rightarrow K^- \pi^+$  can be simulated using four-vector relativistic kinematics and random generators. In the course

of this work, a toy Monte Carlo (MC) was developed for the use in several parts of this thesis.

The decay routine is described in the following. In the centre-of-mass frame of the  $D^0$ , the four-momentum of the kaon is initialised with the three-momentum pointing in a random direction on a sphere with radius  $861.06 \text{ MeV}/c$  (cf. section 4.2.4). In a second step, the four-momentum of the pion is initialised with the three-momentum pointing in the opposite direction. The three-momentum of the corresponding mother particle is then randomly generated in  $(p_T, y, \phi)$  space. According to both FONLL [17] and PYTHIA [70, 71] predictions, the rapidity distribution of  $D^0$  mesons in pp collisions is flat within 1% in  $|y| < 1$ . The rapidity for generated  $D^0$  mesons is thus drawn from a uniform distribution in a given interval around mid-rapidity. The underlying  $p_T$  distribution can be chosen flat, or realistic, e.g. using the FONLL  $p_T$  distribution. For the  $\phi$  angle, a flat distribution in  $[0, 2\pi]$  is used. Once the mother and daughter particles are initialised, the four-momenta of the daughter particles are boosted to the lab frame with a Lorentz transformation based on the three-momentum of the mother particle. The entire kinematic information of a particular decay is thus contained in the resulting three-momenta of the kaon and the pion (six numbers). Depending on the goal of the specific simulation, this information is then processed further.

In fig. 4.3, the momentum and transverse momentum spectra of the decay daughters are displayed, along with their angular distance in the transverse plane,  $\Delta\phi$ . Ten million  $D^0$  mesons with  $|y| < 0.8$  were generated with the toy MC in four  $p_T$  bins in  $0 < p_T < 4 \text{ GeV}/c$  (top to bottom in fig. 4.3). The daughter particles were additionally restricted to  $|\eta| < 0.8$  to mimic the corresponding track selection cut applied in this analysis (cf. section 5.4). A minimum transverse momentum was not required.

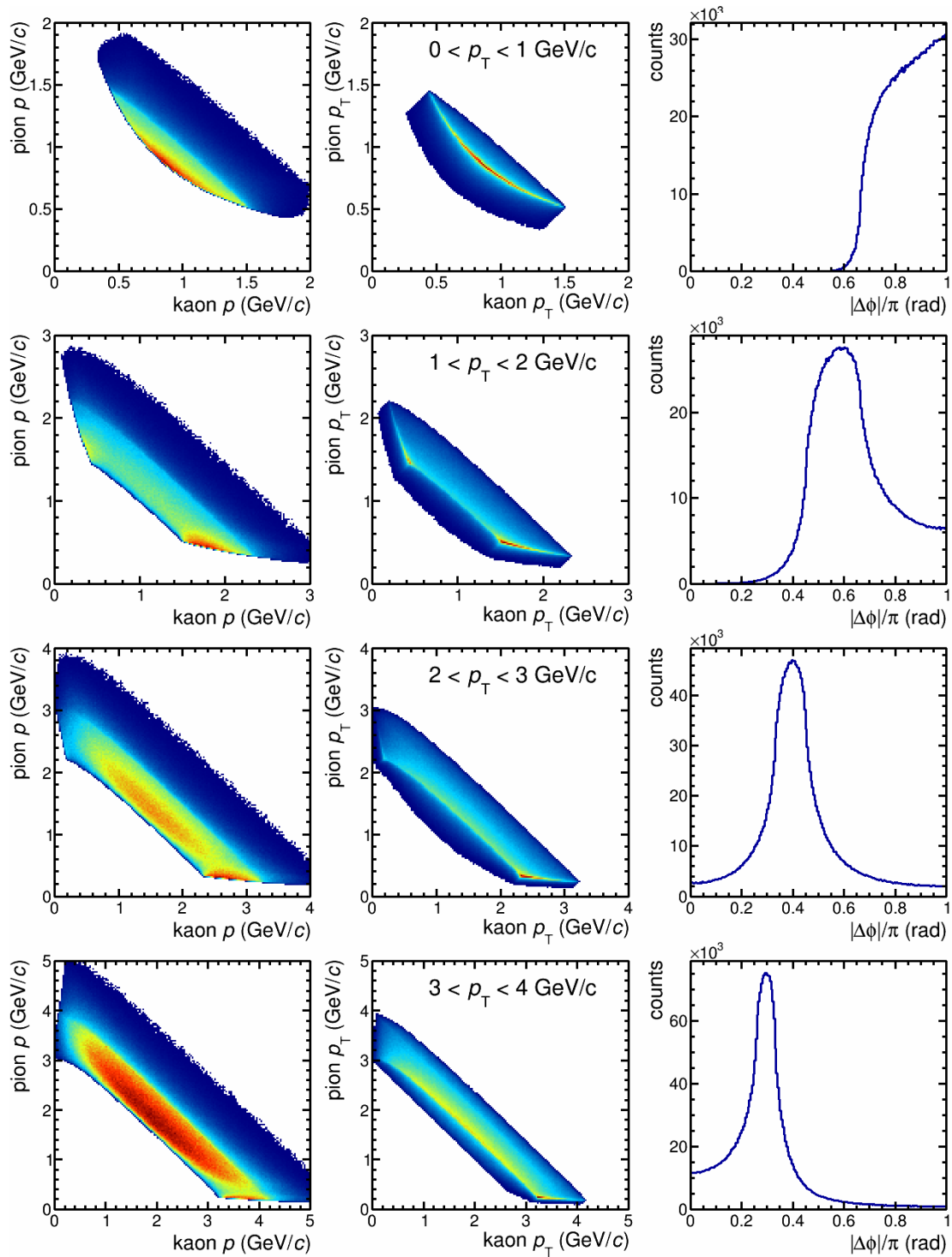


Figure 4.3: Simulated kinematics of the  $D^0 \rightarrow K^- \pi^+$  decay. The two-dimensional (transverse) momentum spectra of the daughter particles are shown on the left (in the middle), along with their angular distance,  $\Delta\phi$ , on the right. Ten million  $D^0$  mesons were generated in  $|y| < 0.8$ . A selection with  $|\eta| < 0.8$  was applied on the daughter particles.

## DATA ANALYSIS

---

In this chapter, the different steps of the analysis of low- $p_T$   $D^0$  production are described in detail. The chapter starts with a general overview of the analysis strategy. After some remarks on computational aspects and workflow, further details about each analysis stage can be found in a dedicated subsequent section.

## 5.1 Strategy and Overview

$D^0$  mesons and their antiparticles  $\bar{D}^0$  mesons are reconstructed in the decay channel  $D^0 \rightarrow K^- \pi^+$  and its charge conjugate with a small contribution of about 0.4% from the doubly Cabibbo-suppressed decay  $D^0 \rightarrow K^+ \pi^-$ , as pointed out in section 4.1. The analysis is run on selected events in a data set of pp collisions recorded with ALICE in 2010 at a centre-of-mass energy  $\sqrt{s} = 7$  TeV. The data samples and the event selection are described in section 5.3. Within the reconstructed events, charged particles are represented by tracks that have been reconstructed from detector signals in the ITS and the TPC. A quality and kinematic selection is applied on the tracks that are present in each event, as detailed in section 5.4. The selected tracks are then processed further in the analysis. Without any assumption on the particle type, each combination of a negative and a positive track within the same event is accepted as a  $D^0$  candidate. The  $D^0$  signature is a peak in the invariant mass distribution of all such candidates at the nominal  $D^0$  mass. It is intrinsic to the procedure of combining tracks to implicate a large combinatorial background of track pairs not originating from a  $D^0$  decay, of

which the invariant mass falls in the  $D^0$  peak region by coincidence. A priori, the signal-to-background ratio (S/B) is thus only about  $2.5 \times 10^{-4}$  in the low- $p_T$  region, where the combinatorial background is particularly large due to the production of soft pions and kaons. The stable extraction of the signal in such a high background environment constitutes the major challenge to this analysis.

The excellent particle identification (PID) capabilities of ALICE contribute significantly to the reduction of background, while retaining a high efficiency for the signal. The specific energy loss per unit of path length  $dE/dx$  of charged particles in the TPC gas is used in conjunction with the time-of-flight information provided by the TOF system. Details of the PID strategy are discussed in section 5.5. After PID selection, the S/B ratio is about  $10^{-3}$  in the  $p_T$  interval  $0 < p_T < 1 \text{ GeV}/c$ . At this scale, signal extraction is still very sensitive to the unknown background shape and thus highly unstable. An estimate of the combinatorial background is therefore subtracted from the invariant mass spectrum, as part of the signal extraction, using the like-sign technique. After subtraction of the combinatorial background, the  $D^0$  yield is extracted in the full  $p_T$  range  $0 < p_T < 16 \text{ GeV}/c$  by fitting with a parameterisation of the signal and the small residual background that survived the background subtraction. Section 5.6 is dedicated to the signal extraction procedure.

The extracted raw yield is corrected by the efficiency of the reconstruction and the selections applied in the analysis. The efficiency correction is determined by analysing Monte Carlo (MC) events that were generated in a realistic simulated detector environment, applying the identical reconstruction algorithm and the same selections as for real data. In the standard topological D-meson analysis, the efficiency quickly drops to zero for small  $p_T$ . In this work, however, the efficiency flattens off at about 20% going towards zero transverse momentum of the  $D^0$ . Signal extraction thus becomes possible in the entire momentum space, assuming that the background is under control. Section 5.7 contains details about the efficiency correction.  $D^0$  mesons from B decays are denoted as feed-down. Their contribution to the measured  $D^0$  yield must be subtracted, relying on theory input, in order to derive the cross section of prompt  $D^0$  production. The analysis step of feed-down subtraction is described in section 5.8. With all the input gathered, the chapter concludes section 5.9 with the calculation of the  $D^0$  production cross section.

## 5.2 Computational Analysis

For a variety of programming tasks including data processing, Monte Carlo simulation and data visualisation, the ALICE collaboration uses the C++ based object oriented data analysis framework ROOT [72]. Libraries that are specific to the ALICE experiment are collected and maintained in a derived package known as AliRoot [73]. The code used for data analysis with a specific physics goal is called an analysis task and is typically implemented as an AliRoot class. Analysis tasks share a common global structure, the most important parts being a function for the definition of output objects, which are mainly histograms, and a function that is executed for each analysed event. The task developed for the analysis of D mesons without topological selection is `AliAnalysisTaskCombinHF` and can currently be found in the AliRoot directory `PWGHF/vertexingHF`. Certain configurations like the track selection cuts or the specific method for particle identification can be inserted as parameters by the user. Thus, it becomes possible to run multiple versions of the same task with different setups in order to compare different selections. Due to the rather large data files, the analysis is computationally expensive and the infrastructure of a world-wide computing grid [74] was used. The average CPU time to process one event was of the order of 10 ms. With parallelisation, the typical duration for processing the entire data set of about 380 million events before selection was about six hours.

Analysis tasks operate on preprocessed data sets that contain fully reconstructed events, providing a convenient interface for the end user. The first step towards these sets after data taking is the reconstruction of physical objects from raw detector signals. In a tracking detector, for example, the procedure consists of reconstructing charged particle tracks by fitting neighbouring clusters of energy loss to curved lines (cf. section 5.4). The reconstructed events containing the reconstructed objects for the different detector systems are initially stored in a structure called Event Summary Data (ESD). The data sets can then be processed further into a final format called Analysis Object Data (AOD). Different filters can be applied in this last processing step from ESDs to AODs, in order to reduce the large data amount and to provide easier access to the end user.

Once the output of an analysis task is available, a series of ‘post-processing’ steps is performed, including signal extraction, the calculation of the cross section with the respective corrections and finally data visualisation.

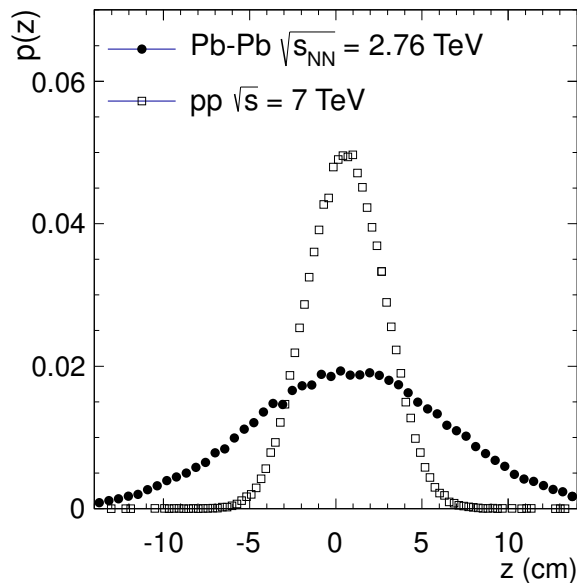


Figure 5.1: Distribution of the  $z$  position of reconstructed vertices in pp and Pb–Pb collisions. This figure was taken from [62].

### 5.3 Data Sets and Event Selection

The analysed data set consists of pp collisions from 2010 at a centre-of-mass energy of 7 TeV. The events were collected with a minimum bias trigger, requiring a hit in either of the two V0 counters or in one of the two SPD layers in coincidence with the arrival of proton bunches. This particular trigger is sensitive to about 87 % of the inelastic pp cross section [75]. It was verified that the trigger was 100 % efficient for D mesons [11].

The event selection is the same as in the topological analysis [11]. The following event cuts are applied offline in addition to the online trigger requirement. Background from interactions of the beam with residual gas in the beam pipe is rejected using the timing information from V0A and V0C. Events without a reconstructed vertex are discarded. The reconstructed vertex is required to be located within  $|z| < 10$  cm from the central interaction point, in order to assure some amount of symmetry in the detector acceptance. This cut is almost fully efficient for pp collisions, as can be seen in fig. 5.1, where the distribution of the  $z$  position of reconstructed vertices is shown. Furthermore, events that contain more than one collision vertex are rejected. This so-called pile-up rejection is

performed on the basis of vertices reconstructed from SPD tracklets, which are correlated hit pairs in the two SPD layers. An event is classified as a pile-up event and consequently rejected if it contains more than one SPD vertex with a minimum number of three contributing tracklets and a minimum distance of 0.8 cm in  $z$  direction between the vertices. A total number of about 280 million selected events is then processed in the analysis task.

In addition to the number of analysed events, the number of events with a non-reconstructed vertex in  $|z| < 10$  cm has to be accounted for in the calculation of the cross section. Under the assumption that the  $z$  distribution is the same for events with and without a reconstructed vertex, the number of events with a non-reconstructed vertex in  $|z| < 10$  cm can be estimated from the number of events with a reconstructed vertex using

$$N(\text{w/o vert.}, |z| < 10 \text{ cm}) = N(\text{w/o vert.}, |z| < \infty) \times \frac{N(\text{w/ vert.}, |z| < 10 \text{ cm})}{N(\text{w/ vert.}, |z| < \infty)}. \quad (5.1)$$

In this formula,  $N(\dots)$  denotes the number of events with (w/) or without (w/o) a reconstructed vertex, within the specified  $z$  range. The total number of events,  $N_{\text{events}}$ , considered for the calculation of the  $D^0$  production cross section is then

$$N_{\text{events}} = N(\text{w/ vert.}, |z| < 10 \text{ cm}) + N(\text{w/o vert.}, |z| < 10 \text{ cm}) = 327 \text{ million}. \quad (5.2)$$

The first term corresponds to the number of analysed events having passed the selection; the second term is estimated using eq. (5.1) above. With the minimum bias cross section,  $\sigma_{\text{MB}} = 62.3 \text{ mb}$  [75], this number of events corresponds to the following integrated luminosity for the analysed data sample:

$$\mathcal{L}_{\text{int}} = \frac{N_{\text{events}}}{\sigma_{\text{MB}}} = 5.25 \text{ nb}^{-1}. \quad (5.3)$$

## 5.4 Track Reconstruction and Selection

A track represents the flight path of a charged particle traversing active detector volume. The procedure of combining single detector signals to global tracks in the course of event reconstruction is called tracking. Several central barrel detectors of ALICE are involved

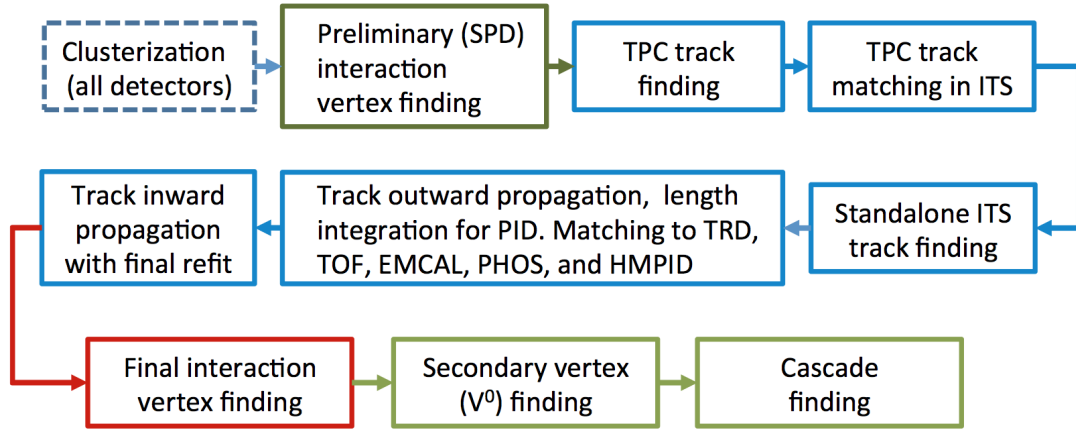


Figure 5.2: Flow chart for the different stages of the tracking procedure. This figure was taken from [62].

in this process. The outcome of the tracking algorithm is a set of reconstructed tracks for each event. Afterwards, an analysis can operate on these reconstructed tracks, applying a certain selection based on parameters that are stored together with each track.

A flow chart of the tracking procedure can be found in fig. 5.2. In a preliminary step, single detector signals are clustered within each detector. A first estimation of the interaction vertex position is obtained from SPD tracklets. The tracking procedure then uses track seeds from adjacent clusters in the outer TPC pad rows pointing towards the estimated vertex. Starting from each track seed, a track is propagated inwards throughout the TPC chamber performing a fit based on a Kalman filter approach [76]. During the fitting procedure, the track parameters are continuously updated, taking into account multiple scattering and energy loss. If a match is found, the fit is continued through the ITS up to the estimated primary vertex. In the next step, the track is re-propagated outwards through the ITS and the TPC. If re-matching with the TPC is achieved, the track is assigned the label ‘TPC refit success’. The track is then matched with detectors at larger radial distance, namely TRD, TOF, EMCAL, PHOS and HMPID (for explanation of the acronyms see section 3.2). Only the matching with TOF is relevant for this analysis. In the last tracking step, the track is re-propagated inwards starting from the initial track seed again. If re-matching with ITS succeeds, the track is assigned the label ‘ITS refit success’.

After all the tracks in one event are processed, the primary vertex and possible secondary

label	description	cut value
TS1	no. of crossed rows in the TPC	$\geq 70$
TS2	no. of crossed rows / no. of findable clusters	$\geq 0.8$
TS3	no. of clusters in the TPC	$\geq 50$
TS4	$\chi^2$ per no. of clusters in the TPC	$\leq 4$
TS5	TPC refit success	yes
TS6	ITS refit success	yes
TS7	reject kink daughters	yes
TS8a	DCA to vertex in transverse plane	$< 2.4$ cm
TS8b	DCA to vertex in $z$ direction	$< 3.2$ cm
TS9	pseudo-rapidity $ \eta $	$< 0.8$
TS10	transverse momentum $p_T$	$> 0.3$ GeV/ $c$

Table 5.1: Selection cuts for single tracks used in this analysis. The cuts are labelled for reference in the text.

vertices are recomputed using the full information from the reconstructed tracks. This results in a better precision on the position of primary and secondary vertices. The reconstruction of secondary vertices with high precision is not relevant to the analysis presented here, in contrast to the topological analysis, where it is an essential part of the analysis strategy.

A quality selection of tracks has to be applied in order to assure sufficient momentum and  $dE/dx$  resolution and a high reconstruction efficiency. The applied single track cuts are listed in table 5.1. The cuts are labelled for referencing in the text. The cuts TS1 to TS6 are pure quality cuts; TS7 to TS8b partially serve as background rejection; TS9 and TS10 are kinematic cuts. A minimum of 70 crossed pad rows in the TPC (TS1) out of a possible 159 is required in order to assure a minimum track length. This has the most direct impact on the momentum resolution. An additional cut on the ratio of the number of crossed rows in the TPC and the number of findable TPC clusters of 0.8 (TS2) is applied. The number of findable clusters is defined as the maximum number of clusters that could be assigned to a track with a given geometry provided full efficiency in the reconstruction. The minimum requirement of 50 clusters in the TPC (TS3), is an artefact of the AOD-filtering stage of the used data set (cf. section 5.2). However, TS3 has no effect, since all tracks rejected by TS3 are also rejected by TS1 and TS2.

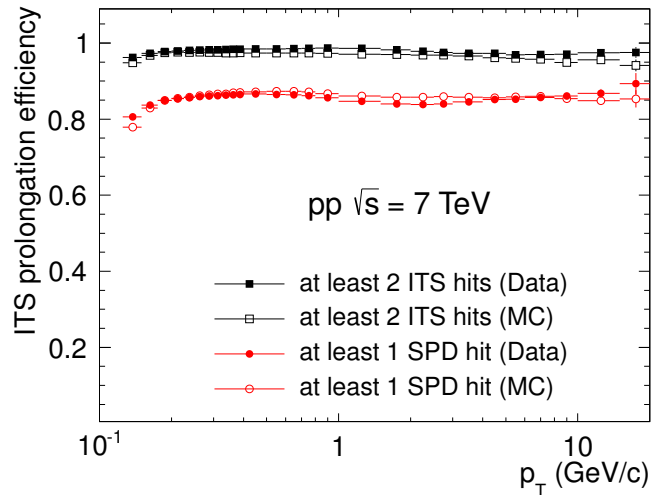


Figure 5.3: ITS-TPC matching efficiency in pp collisions with different requirements of ITS and SPD clusters. The figure was taken from [62].

To ensure good quality of the track reconstruction, a maximum  $\chi^2$  per number of TPC clusters of four is required in the fitting of space points during the reconstruction (TS4). Tracks are accepted only if the TPC (TS5) and the ITS (TS6) refit succeed. Tracks with kinks are rejected (TS7) because they typically represent decaying particles. Tracks with a distance of closest approach (DCA) to the primary vertex outside an ellipsoid centred around the primary vertex, with half-axes of 2.4 cm in the transverse plane (TS8a) and 3.2 cm in  $z$  direction (TS8b), are rejected. The DCA cut is intended to reject secondary tracks, e.g. from the decay of strange particles, and background from interactions with the beam pipe. As the cut is rather soft, it has little impact on the total number of accepted tracks in this analysis.

Finally, kinematic cuts on the pseudo-rapidity of  $|\eta| < 0.8$  (TS9) and on the transverse momentum of  $p_T > 0.3 \text{ GeV}/c$  (TS10) are applied. The minimum  $p_T$  cut is necessary to avoid uncertainties in the Monte Carlo description of the dropping tracking efficiency at low momenta. Furthermore, the  $p_T$  cut of  $0.3 \text{ GeV}/c$  corresponds to the kinematic acceptance of the TOF detector, as for particles with smaller momenta the track curvature in the magnetic field is too large. It can be seen in fig. 4.3 that the low  $p_T$  cut is essentially fully efficient for the signal in the  $D^0$  transverse momentum bin  $0 < p_T < 1 \text{ GeV}/c$ .

The track selection differs in one important aspect from the selection applied in the topological analysis: the requirement of a hit in at least one of the two SPD layers is

crucial for the topological D-meson analysis to assure high precision in the reconstruction of the decay topology. This requirement results, however, in a relatively large decrease of the ITS prolongation efficiency from close to 100 % down to around 85 %, as can be observed in fig. 5.3. This decrease is due to cooling problems in the SPD during the pp data runs from 2010, which lead to a high dead channel rate and thus reduced acceptance. For this analysis, it is considered fully sufficient to require at least two hits in any of the ITS layers, which is implicitly contained in the selection cuts TS5 and TS6. For this looser selection, the ITS prolongation efficiency is close to one. Since two tracks are involved in the analysis, the absence of the requirement of an SPD hit yields an excess of about 30 % on the number of  $D^0$  candidates for this analysis as compared to the topological analysis. It is reasonable to assume that signal and background scale in the same way, as no topological selection is involved, which would require high-precision pointing of the track. The increase in statistics is consequently associated with an increase in significance of about a factor  $\sqrt{1.3} = 1.14$ . This increase in significance is an important benefit for the signal extraction at low  $p_T$ .

In addition to the single track selection, a rapidity cut of  $|y| < 0.8$  was applied on  $D^0$  candidates constructed by combining track pairs. This corresponds to the maximum rapidity range for  $D^0$  mesons that is kinematically accessible due to the selection  $|\eta| < 0.8$  on the single tracks (TS9). Apart from the rapidity cut, no further selection was applied on  $D^0$  candidates.

## 5.5 Particle Identification

A powerful tool at hand for the rejection of background is particle identification (PID). For the identification of kaons and pions, the specific energy loss  $dE/dx$  in the TPC and the time of flight measured with the TOF system are used.

### 5.5.1 PID Information from TPC and TOF

A charged particle propagating in the active volume in the TPC loses energy via ionisation of gas atoms (cf. section 3.4). The number of generated electrons and ions is proportional to the specific energy loss per unit of path length,  $dE/dx$ , of the ionising particle. The created charge is collected with the TPC readout panels and transformed into a

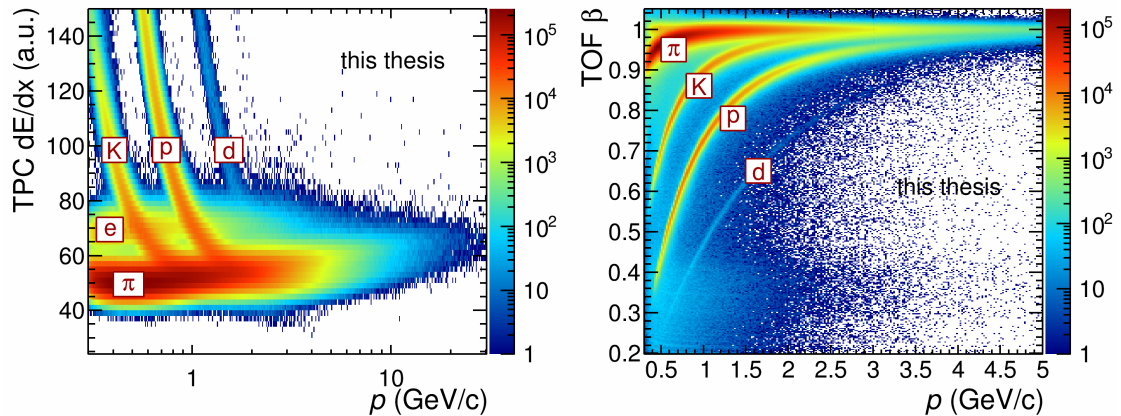


Figure 5.4: TPC  $dE/dx$  signal (left) and Lorentz  $\beta$  from TOF time-of-flight information (right) as a function of the reconstructed track momentum  $p$ . The displayed tracks were selected using the cuts listed in table 5.1. The bands for electrons, pions, kaons, protons and deuterons are distinguishable up to a certain track momentum, which increases for heavier particles.

dimensionless signal in arbitrary units, which is assigned to each track. No absolute normalisation is given, as it is sufficient for PID purposes to deal in relative numbers. The energy loss depends on the momentum and mass of the ionising particle. In combination with a momentum measurement, the  $dE/dx$  signal can thus be used to test a given mass hypothesis for a particle by comparing with the expected energy loss for the respective species. The expected energy loss is extracted from data via a fit with a parameterisation of the Bethe-Bloch formula using 5 free parameters  $P_i$ , which was first proposed by the ALEPH experiment [77]:

$$f(\beta\gamma) = \frac{P_1}{\beta^{P_4}} (P_2 - \beta^{P_4} - \ln \left( P_3 + \frac{1}{\beta\gamma^{P_5}} \right)). \quad (5.4)$$

In the left panel of fig. 5.4, the measured  $dE/dx$  vs. track momentum is plotted for all tracks selected with the cuts listed in table 5.1. Bands for electrons, pions, kaons, protons and deuterons can be clearly distinguished up to a certain momentum, where the bands start to cross and overlap. Kaons start to merge with the pion band at about  $0.7 \text{ GeV}/c$ , protons at about  $1.3 \text{ GeV}/c$ . The largest separation power is given in the low-momentum region, where the  $1/\beta^2$  term of the Bethe-Bloch formula dominates. This region extends up to higher momenta for heavier particles. Identification in the relativistic rise is more challenging, but can still be performed using a statistical separation method. The electron

band differs in its structure from the other particles, as electrons are already at the Fermi plateau in the plotted momentum range due to their low mass.

The particle identification with TOF is independent of the identification using the TPC. It provides complementary information, which is of particular importance in the momentum region where the TPC  $dE/dx$  bands for different particles cross. The TOF particle identification is based on a velocity measurement to distinguish massive charged particles. The relativistic velocity  $\beta$  can be determined from the track length  $l$  and the measured time difference  $\Delta t$  between the TOF arrival time and the start signal from the T0 detector, using

$$\beta = \frac{l}{\Delta t}. \quad (5.5)$$

Again with the additional knowledge of the particle momentum  $p$ , a relation to the particle mass  $m$  can be established via  $p = \beta\gamma m$ . The momentum dependence of  $\beta$  for a given mass hypothesis is derived by solving this equation for  $\beta$ :

$$\beta = \frac{p/m}{\sqrt{1 + (p/m)^2}}. \quad (5.6)$$

It becomes apparent in this formula that the mass acts as a scaling factor for the rise from  $\beta = 0$  at  $p = 0$  to  $\beta = 1$  for  $p \rightarrow \infty$ , in the sense that light particles approach  $\beta = 1$  already at low momentum. Larger separation power is thus given for heavier particles, as in the case of particle identification from the TPC.

Thus in analogy to  $dE/dx$  particle identification, the TOF particle identification has larger separation power for heavier particles. The expected behaviour is observed in the right panel of fig. 5.4, where the measured velocities are plotted for the tracks in the investigated data sample. Due to the finite timing resolution, values for  $\beta$  slightly above unity are visible.

### 5.5.2 PID Strategy

Based on the information from TPC and TOF, kaons and pions are identified using compatibility cuts on the difference between the measured signal  $A$  and the expected signal  $\langle A \rangle_{\text{exp}}^{\text{K}/\pi}$  for a kaon or pion normalised to the experimental resolution  $\sigma_A$ , where  $A$  represents either  $dE/dx$  or time of flight. A dedicated variable is accordingly defined

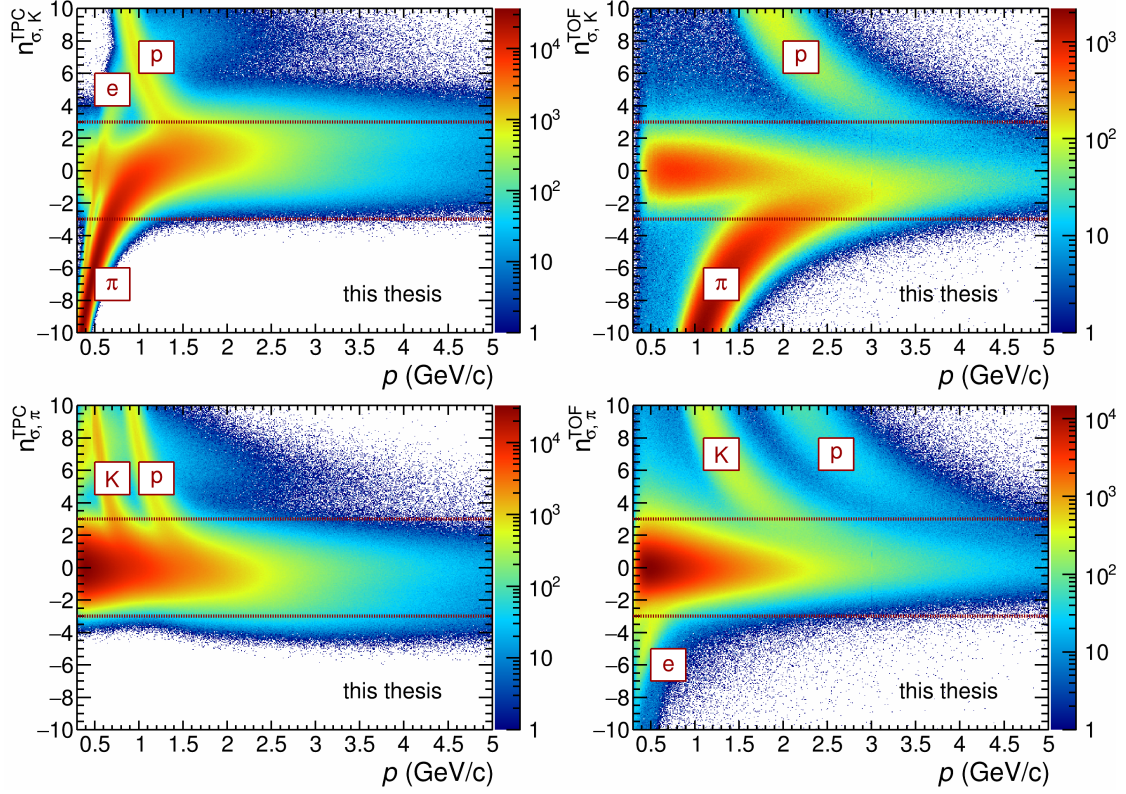


Figure 5.5: The PID  $n_\sigma$  variable for the kaon (top) and pion (bottom) hypothesis in TPC (left) and TOF (right). The dashed lines indicate the  $3\sigma$  cut used in the analysis. Contaminations from different species are labelled.

as

$$n_{\sigma,K/\pi}^{\text{TPC/TOF}} = \frac{A - \langle A \rangle_{\text{exp}}^{K/\pi}}{\sigma_A}. \quad (5.7)$$

The TPC information is available for every track used in the analysis. This does not hold for the TOF information, which can be absent, if the matching of the track from TPC to TOF fails, for example if the particle is absorbed after traversing the TPC. If TOF information is missing, the particle is identified using only the TPC with a cut of  $n_\sigma^{\text{TPC}} < 3$  for both kaons and pions. If the TOF information is present, the requirement  $n_\sigma^{\text{TOF}} < 3$  is applied in addition. The efficiency of this strategy is thus close to 100%. PID cuts of this type are also referred to as ‘ $n_\sigma$  cuts’ and the corresponding strategy as ‘ $n_\sigma$ ’ PID. In fig. 5.5,  $n_\sigma$  is plotted for the TPC (left) and the TOF system (right) with a kaon hypothesis (top) or a pion hypothesis (bottom), respectively. The upper and lower  $3\sigma$  cut is indicated by the dotted red lines. Daughter particles from

the decay of a  $D^0$  with a transverse momentum in  $0 < p_T < 1 \text{ GeV}/c$  populate the momentum space between about  $0.5 \text{ GeV}/c$  and  $2 \text{ GeV}/c$ , as can be seen in fig. 4.3. For this momentum region, the  $3\sigma$  TOF cut is particularly powerful in terms of background rejection. With the presented strategy, the background at low  $p_T$  is reduced by about a factor of four, while retaining more than 99% of the signal.

Different PID strategies were studied for potential use in the analysis, evaluating important criteria such as the ability to reject background and the robustness in terms of the systematic uncertainty of the method. In particular, several tighter  $n_\sigma$  strategies and a Bayesian approach were considered, in addition to the presented  $3\sigma$  strategy. However, an increased S/B ratio that one might get from a more refined strategy is associated with systematic uncertainties that are typically larger and harder to determine. The basic  $3\sigma$  approach was chosen due to its close to 100% efficiency and its robustness. This comes also with the advantage that the systematic uncertainty of the particle identification can be inherited from the topological approach, which uses the same strategy, as discussed in section 6.2.

## 5.6 Signal Extraction

The extraction of the  $D^0$  yield, also referred to as the raw yield, from the invariant mass spectra is a crucial step in the analysis and the main source of statistical and systematic uncertainty.

### 5.6.1 Overview and Preliminary Considerations

The signal extraction is performed separately in ten  $p_T$  intervals with the bin limits 0-1-2-3-4-5-6-7-8-12-16  $\text{GeV}/c$ . The nine  $p_T$  intervals in  $1 < p_T < 16 \text{ GeV}/c$  are chosen so as to be identical to those of the topological analysis [11] to simplify a one-to-one comparison. The  $p_T$  bin  $0 < p_T < 1 \text{ GeV}/c$  is new in this analysis. The invariant mass distributions are integrated in the full measured rapidity range  $|y| < 0.8$ .

Figure 5.6 shows the  $K\pi$  invariant mass distribution for  $D^0$  candidates in the range  $0.5 < M(K\pi) < 2.5 \text{ GeV}/c^2$  for the two selected  $p_T$  bins  $0 < p_T < 1 \text{ GeV}/c$  and  $3 < p_T < 4 \text{ GeV}/c$ . The invariant mass bin width of the two histograms is  $2 \text{ MeV}/c^2$ .

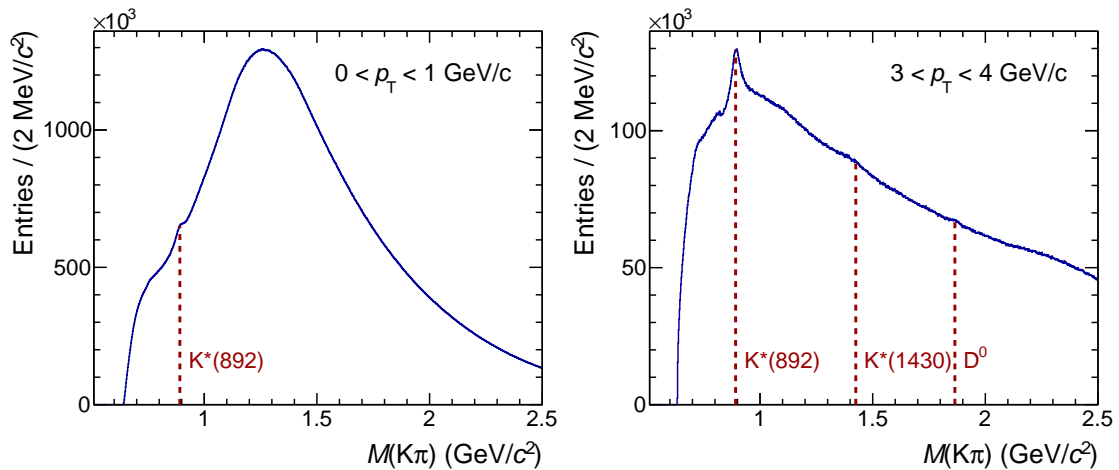


Figure 5.6: Overview of the structure of the  $K\pi$  invariant mass distribution for  $D^0$  candidates in the  $p_T$  intervals  $0 < p_T < 1 \text{ GeV}/c$  (left) and  $3 < p_T < 4 \text{ GeV}/c$  (right). In the first  $p_T$  bin, only the  $K^*(892)$  peak can be distinguished from the large background by the eye. The  $D^0$  peak apparently vanishes due to a low signal-to-background ratio of about  $10^{-3}$ . For  $3 < p_T < 4 \text{ GeV}/c$ , the  $K^*(1430)$  peak and the  $D^0$  peak also become visible.

The observed invariant mass threshold coincides well with the theoretical value of  $M_{\min} = 0.633 \text{ GeV}/c^2$ , which is the sum of the kaon and pion mass, as can be seen from eq. (4.12). Starting from this kinematic boundary, the invariant mass distribution rises up to a maximum and then falls again, where the rise is steeper than the decrease. This global structure is similar for those transverse momentum intervals not displayed in fig. 5.6.

The bin entries of the invariant mass distribution follow a Poisson distribution. The associated relative uncertainty thus decreases with  $1/\sqrt{N}$ , where  $N$  is the bin content. The shape of the  $D^0$  candidate distribution in  $0 < p_T < 1 \text{ GeV}/c$  is therefore rather smooth due to the large number of candidates per invariant mass bin. A peak is visible in the structure at  $M(K\pi) = 892 \text{ MeV}/c^2$ , which results from the  $K^*(892)$  decay to a  $K\pi$  pair. In this lowest  $p_T$  interval, the  $D^0$  peak, expected at  $M(K\pi) = 1865 \text{ MeV}/c^2$ , remains hidden to the naked eye due to a low signal-to-background (S/B) ratio of about  $10^{-3}$ . In the  $p_T$  interval  $3 < p_T < 4 \text{ GeV}/c$ , the background scale is decreased by about an order of magnitude and the  $D^0$  peak can be identified. In addition, another kaon resonance, the  $K^*(1430)$ , becomes visible. Statistical fluctuations in the invariant mass distribution are more pronounced than for  $0 < p_T < 1 \text{ GeV}/c$  due to the lower background.

The width of the  $D^0$  peak in the  $K\pi$  invariant mass distribution is determined by the resolution of the transverse momentum and the resolution of the angular separation in  $\phi$  of the reconstructed kaon and pion tracks, as can be seen from eq. (4.13). For the  $D^0$  momenta that are considered in this analysis, the  $p_T$  resolution of daughter tracks has the dominant influence on the  $D^0$  peak width, since the angular difference between the two daughter tracks is large (cf. fig. 4.3). For daughter particles originating from a low- $p_T$   $D^0$  decay, the relative  $p_T$  resolution is about 1%. The Gaussian shape of the inverse transverse momentum resolution from the track fit propagates to an approximate Gaussian shape of the peak in the invariant mass distribution. It was verified with a Monte Carlo (MC) simulation that the deviation of the peak shape from a real Gaussian is small and can be neglected as compared to the systematic uncertainty of the yield extraction. The MC framework is the same as that used for the efficiency correction, as described in section 5.7. A prediction for the  $D^0$  peak width can be extracted from this MC framework. It is about  $10 \text{ MeV}/c^2$  in the lowest  $p_T$  bin and increases up to about  $25 \text{ MeV}/c^2$  in the highest  $p_T$  bin. The increase towards larger  $p_T$  of the mother particle is due to the linear increase of the  $p_T$  resolution of the daughter tracks. The natural  $D^0$  linewidth of  $1.6 \text{ meV}$  [23] can certainly be neglected in these considerations. The detailed knowledge of the peak shape serves as a valuable input for the signal extraction, as will be detailed in section 5.6.3.

The adopted procedure for the yield extraction is to fit the invariant mass distribution in a certain window around the  $D^0$  peak. The fit function can be composed of the sum of a Gaussian function for the signal, as motivated in the last paragraph, and a parameterisation for the background. The signal is then extracted as the integral of the signal function. The challenge of this procedure is the fact that the shape of the background is a priori unknown. In the topological  $D^0$  analysis, an exponential function is used to describe the background, which is then substituted by a second-order polynomial to evaluate the systematic uncertainty. This simple approach performs well if the signal-to-background ratio is sufficiently large. For the topological analysis, the S/B values between 0.1 and 1 are relatively large by construction, as the selection on the decay topology is tuned for large significance and S/B ratio in the data.

The cost of giving up the topological selection in order to extend the measurement down to zero transverse momentum is a much lower S/B ratio. The lowest  $p_T$  bins, which are targeted by this analysis, suffer from a particularly low S/B ratio of the order of  $10^{-3}$

since the combinatorial background originates mainly from soft pion and kaon production. A direct fit of the invariant mass distribution in the  $p_T$  bin  $0 < p_T < 1 \text{ GeV}/c$  with the sum of a Gaussian and a second-order polynomial or exponential function still converges with a reasonable result, if the information about the width and position of the  $D^0$  peak is provided. Due to the low S/B ratio, however, the fit result is highly sensitive to the particular choice of the fit function and the fit range and thus unstable. In order to improve the stability of the signal extraction at low  $p_T$ , it is therefore necessary to subtract a background estimate before a fit is performed.

### 5.6.2 Background Subtraction

The combinatorial background presumably contains a variety of correlated background, including for example  $K\pi$  pairs that are part of the final state of hadron decays other than  $D^0 \rightarrow K^- \pi^+$ . Another contribution comes from correlated hadron pairs from decays that have been misidentified as  $K\pi$  pairs.  $K\pi$  pairs from jet fragmentation provide a further contribution to the correlated background that is particularly important in pp collisions as compared to Pb–Pb collisions. Due to the many possible correlations between produced primary or secondary kaons and pions in pp collisions, it is practically impossible to precisely calculate or simulate the entire background.

The random combinatorial background from uncorrelated kaon and pion production could still be simulated, based on realistic  $p_T$  spectra for kaon and pion production. The practical use of such a simulation for the signal extraction would, however, require many details, in particular: the tracking efficiencies for kaons and pions; a realistic  $\eta$  and  $\phi$  distribution; the imperfections of the particle identification and event multiplicity and topology. Most of these parameters would have to be taken from or tuned on data. A more promising approach is therefore to obtain an estimate of the combinatorial background in a completely data-driven approach. In this work, the like-sign, track-rotation and event-mixing techniques were studied. The basic working principle of these methods is to change a small aspect in the reconstruction of the  $K\pi$  invariant such that a certain class of possible correlations between the kaon and the pion is excluded. Each of the methods thus results in an invariant mass distribution for mainly uncorrelated combinatorial background. A clear distinction of ‘correlated’ and ‘uncorrelated’ background is difficult in this context, as initially correlated kaons and pions also enter into these methods.

In the **like-sign** (LS) approach, correlations between kaons and pions are destroyed by combining pairs of equal sign instead of opposite sign. The invariant mass distribution of the equal-sign pairs,  $K^+\pi^+$  and  $K^-\pi^-$ , is thus reconstructed, instead of building  $D^0$  ( $\overline{D}^0$ ) candidates from opposite-signed  $K^-\pi^+$  ( $K^+\pi^-$ ) pairs. The two like-sign distributions are combined by taking two times their geometric mean:

$$N^{\text{like-sign}} = 2 \cdot \sqrt{N(K^+\pi^+) \cdot N(K^-\pi^-)} \quad (5.8)$$

It was verified that the two distributions for equal-sign pairs are similar. The particular form of their combination thus has a minor effect on the resulting like-sign distribution. Apart from this combination using the geometric mean, the like-sign method does not contain any parameters or particular configurations and is thus the most ‘straightforward’ of the background-subtraction methods. In particular, no further normalisation is required.

The idea of the **track-rotation** (TR) method is to decouple the kaons from the pions by altering their kinematic relations. For this purpose, all kaon tracks in one event are rotated in the transverse plane by a series of defined angles, leaving  $\eta$  and  $p_T$  invariant. The rotated kaons are then recombined with the opposite-charged pions from the event to rebuild an invariant mass distribution without  $K\pi$  pairs originating from real  $D^0$  decays. For this analysis, the kaon tracks are rotated 19 times with angles  $\Delta\phi = \pi/10, 2\pi/10, \dots, 19\pi/10$ . A 19-fold set of statistics, compared to the LS method, is thus generated and the background shape is determined with negligible statistical uncertainty.

With the **event-mixing** (EM) technique,  $D^0$  candidates are built by combining a kaon and a pion track from two different events. Only events with ‘similar’ properties are mixed with one another. For this purpose, the events are categorised into pools depending on the  $z$  position of their primary vertex and their multiplicity. The limits for the  $z$  vertex position are in the range  $-10 < z < 10$  cm in steps of 2.5 cm. The multiplicity pool limits are 0, 5, 10, 15, 20, 25, 30, 40,  $\infty$ . Consequently, only events within the same pool are mixed. By mixing many different events, a large number of background candidates is generated, similar to the track-rotation method.

In fig. 5.7, the invariant mass distribution of  $D^0$  candidates is displayed along with the LS, TR and EM distributions for all analysed  $p_T$  bins in the range  $0 < p_T < 16$  GeV/ $c$ .

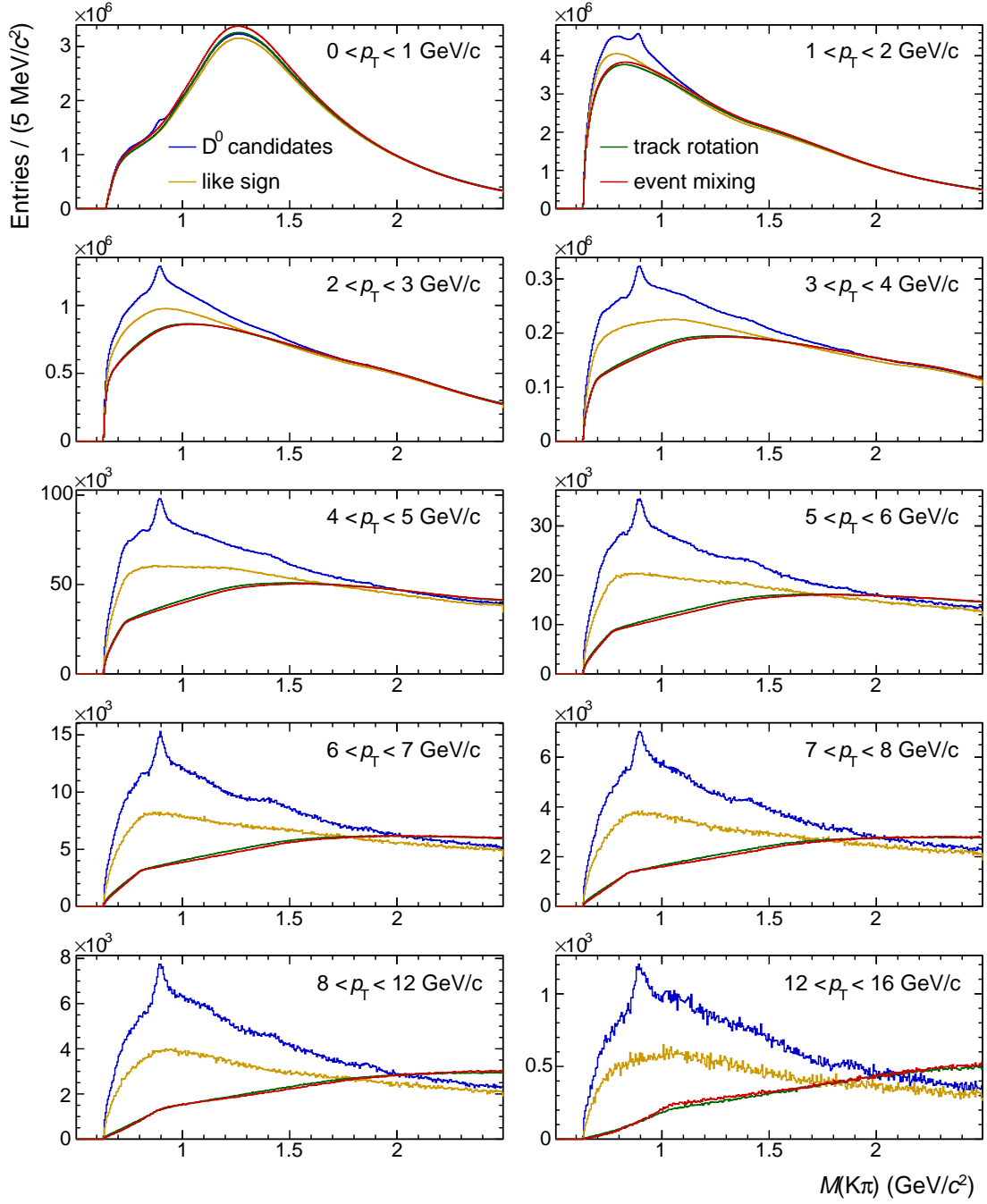


Figure 5.7: The invariant mass distribution for  $D^0$  candidates are shown in all analysed  $p_T$  bins, along with the like-sign, track-rotation and event-mixing distributions. The track-rotation and event-mixing distributions are normalised in the invariant mass region  $2.0 < M(K\pi) < 2.05 \text{ GeV}/c^2$ .

The invariant mass bin width is  $5 \text{ MeV}/c^2$ . Since the TR and EM distribution are not intrinsically normalised as the LS distribution, a certain normalisation has to be enforced. Here, the TR and EM are normalised such that their integrals in the invariant mass range  $2.0 < M(K\pi) < 2.05 \text{ GeV}/c^2$ , just next to the  $D^0$  peak, match the integral of the  $D^0$  candidate distribution in the same invariant mass range.

The LS distribution captures the shape of the  $D^0$  candidate distribution rather well in the entire  $p_T$  range, apart from an offset in higher  $p_T$  bins, which might be due to the correlated background not being described by the LS distribution. This so-called residual background is further quantified at the end of this section. The normalised TR and EM distributions only represent the  $D^0$  candidate distribution in the relevant mass window around the  $D^0$  peak in the first three  $p_T$  bins. Going to higher  $p_T$  bins, the TR and EM distributions deviate more and more from the  $D^0$  candidate distribution. In the highest  $p_T$  bins, the TR and EM shapes feature a continuous increase in the plotted invariant mass range, instead of the typical background structure of a steep rise, a maximum and a decrease. Despite this deviation from the  $D^0$  candidate distribution, the agreement between the TR and the EM distributions is evident in the entire  $p_T$  range.

The deviation of the TR and EM distributions from the candidate and LS distributions can be understood qualitatively in terms of particular event topologies in pp collisions that arise due to the high prevalence of jets. Though the TR and EM techniques are conceptually very different, they have in common the fact that angular correlations between the decay daughters within the event are destroyed. This means that the TR and EM distributions only realistically represent the combinatorial background if the initial distribution of the kaons and pions in  $(\eta, \phi)$  is homogeneous within the event. In the presence of a jet, this is not the case, as charged particles are rather concentrated in a small subspace in  $(\eta, \phi)$ . A smaller angular distance between the kaon and the pion would shift the invariant mass to lower values, as can be seen in eq. (4.13). This is consistent with what can be observed in fig. 5.7. In contrast to the TR and EM distributions, the LS background preserves potential angular correlations between charged particles within one event under the assumption of equally distributed positive and negative kaons and pions.

The consistency of the above considerations was qualitatively checked with the following simple simulation of the combinatorial background. A large number of kaons and pions

with  $\phi \in [0, 2\pi[$ ,  $\eta \in [-0.8, 0.8]$  and  $p_T > 0.3 \text{ GeV}/c$  were generated. These  $\eta$  and  $p_T$  ranges correspond to the kinematic selection applied for the data (TS9, TS10 in table 5.1). The kaon and pion three-momenta were drawn randomly from a uniform  $\eta$  distribution, a uniform  $\phi$  distribution and from parameterised  $p_T$  spectra of measured pion and kaon production. The invariant mass distribution of these generated  $K\pi$  pairs corresponds to the combinatorial background in an ideal environment, where all of the kaons and pions are homogeneously distributed in  $(\eta, \phi)$ . In this configuration, the simulation reflects the general features of the TR and EM distributions, such as the two kinks observed in the rising shape in higher  $p_T$  bins. A restriction of the generated kaons and pions to angles  $\phi \in [0, \pi/4]$  results in a simulated invariant mass distribution that is close to the LS distribution.

In summary, it can be stated that the LS distribution seems to provide the most suitable background description for the  $D^0 \rightarrow K^-\pi^+$  invariant mass analysis in pp collisions. For this work, the like-sign background subtraction is consequently used for the signal extraction in the following. For p-Pb and Pb-Pb collisions, the situation might be different as the distribution of tracks within the events is more homogeneous in  $(\eta, \phi)$ .

As pointed out above, the like-sign distribution description of the combinatorial background is not perfect. A certain fraction of residual background remains after like-sign subtraction, which might be due to correlations between kaons and pions as discussed in the beginning of this section. Figure 5.8 shows the S/B ratio before and after subtraction (left) and the fraction of background that remains after subtraction (right). The values for the signal  $S$  are obtained as described in section 5.6.3. The values for the background  $B$  are obtained counting bin entries of the invariant mass distribution around the  $D^0$  peak and then subtracting the signal. The used range for the bin counting is  $\mu_{MC} \pm 3\sigma_{MC}$ , where  $\mu_{MC}$  and  $\sigma_{MC}$  are the position and width of the mass peak, obtained from Monte Carlo simulations. In the lowest  $p_T$  bin the S/B ratio improves from  $10^{-3}$  before to  $10^{-1}$  after like-sign subtraction. The residual background is thus about 1% of the original background and the like-sign distribution accordingly accounts for 99% of the background. Going to higher  $p_T$  bins, the residual background fraction continuously increases up to about 20%. Interestingly, the S/B ratio after background subtraction is roughly constant at a value of about  $10^{-1}$  in the full  $p_T$  range.

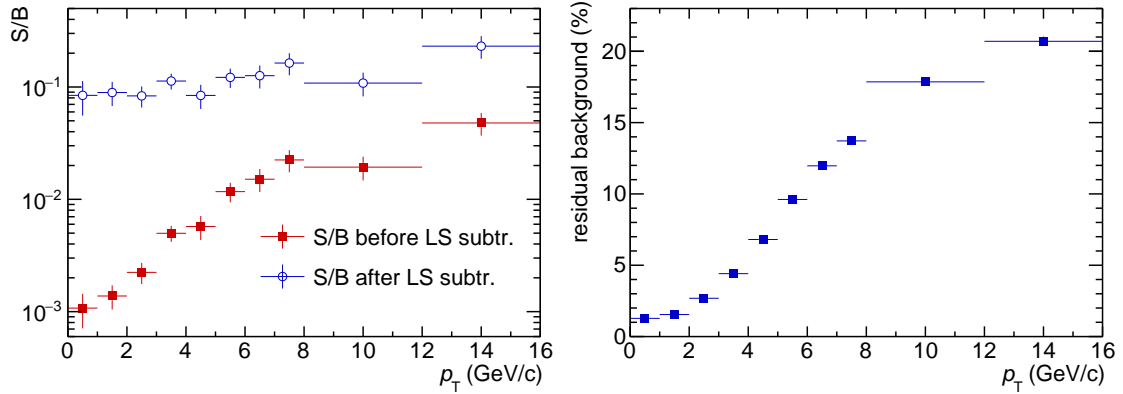


Figure 5.8: Signal to background ratio before and after like-sign subtraction (left) and the remaining residual background in percent (right).

### 5.6.3 Fitting Procedure

Figure 5.9 presents the  $D^0$  candidate invariant mass distribution after like-sign subtraction in the different  $p_T$  intervals. A  $D^0$  peak is now visible by the eye even in the lowest  $p_T$  bin. The invariant mass distribution is fitted individually for each  $p_T$  bin, using the sum of a function for the signal and a function for the background:  $f = f_S + f_B$ . For figs. 5.9 and 5.10, a second-order polynomial is chosen for the background description. An exponential function is considered to be equally suitable and is therefore also considered in the determination of the final raw yields, as described in section 5.6.4. For the signal a Gaussian function is used, as motivated in section 5.6.1:

$$f_S = \frac{S}{\sqrt{2\pi}\sigma} \exp\left(-\frac{(M(K\pi) - \mu)^2}{2\sigma^2}\right) \quad (5.9)$$

The  $D^0$  signal and its statistical uncertainty can be taken directly from the value and the uncertainty of the fit parameter  $S$ , which corresponds to the integral of  $f_S$ . Figure 5.10 shows the peak position  $\mu$  and width  $\sigma$  compared to values obtained from a Monte Carlo analysis. The values from data and MC are consistent within the statistical uncertainties. However, the rather large statistical fluctuations in the peak width have a large impact on the result of the signal extraction. To stabilise the trend of a peak width that increases with  $p_T$ , the width is fixed to the MC values for the extraction of the final raw yields.

The fits of the invariant mass distributions are based on  $\chi^2$  minimisation, assuming

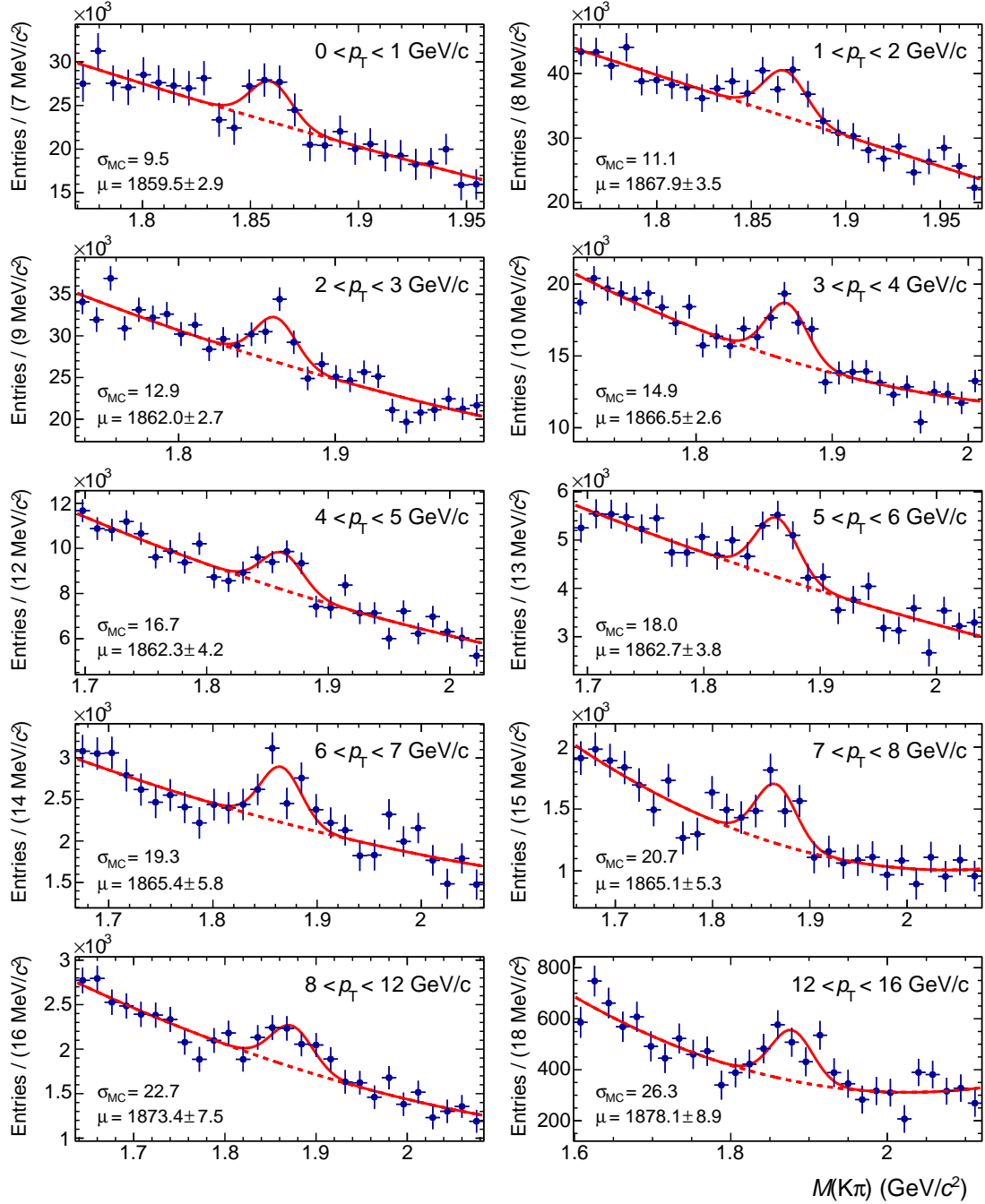


Figure 5.9: Invariant mass distribution after like-sign subtraction for all analysed  $p_T$  intervals. The distributions are fitted with the sum of a Gaussian function for the signal and a second-order polynomial for the background (red curve). For each  $p_T$  bin, the width of the Gaussian is fixed with the value obtained from Monte Carlo,  $\mu_{MC}$ . The numerical values of  $\mu_{MC}$  are indicated on the plots, along with those of the peak positions  $\mu$ , which are treated as a free parameter in the fits.

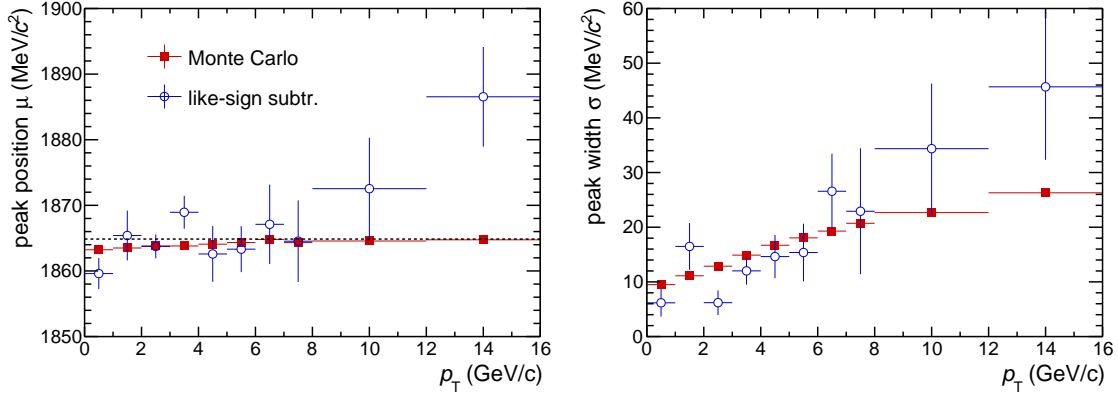


Figure 5.10: Comparison between data and Monte Carlo of the position  $\mu$  and the width  $\sigma$  of the  $D^0$  peak.

Gaussian uncertainties on the bin entries. This assumption is justified as the statistics of the bin entries is large, even for the higher  $p_T$  bins. The invariant mass bin widths are 7, 8, 9, 10, 12, 13, 14, 15, 16, 18  $\text{MeV}/c^2$  for the different  $p_T$  bins. This particular binning is chosen such that the bin width corresponds to about  $0.7\sigma_{\text{MC}}$  in the respective  $p_T$  bin. The fit range has to be chosen such that it contains the mass peak and reasonably large side-bands. As the actual form of the background is unknown, it is favourable to choose as small a range as possible. There is no interest in describing the background far from the mass peak. Decreasing the fit range too much, on the other hand, causes the fit to become more sensitive to background fluctuations. For figs. 5.9 and 5.10, the invariant mass is fitted in a range that corresponds to  $10\sigma_{\text{MC}}$ . For each  $p_T$  bin in fig. 5.9, the plotted range corresponds to the fit range.

#### 5.6.4 Randomised Multi-Trial Approach

To determine the central value for the  $D^0$  signal and the associated statistical and systematic uncertainties, the following method was developed. The fit is performed one thousand times in each  $p_T$  bin, with a different parameter set for each trial. The parameters for each fit are drawn randomly from a pre-defined distribution. The fit function for the background is randomly chosen as either a second-order polynomial or an exponential function. The binning of the invariant mass distributions is drawn from a uniform distribution in the range of  $\pm 20\%$  around the central values defined in section 5.6.3. The values are rounded to the nearest integer. The lower value of

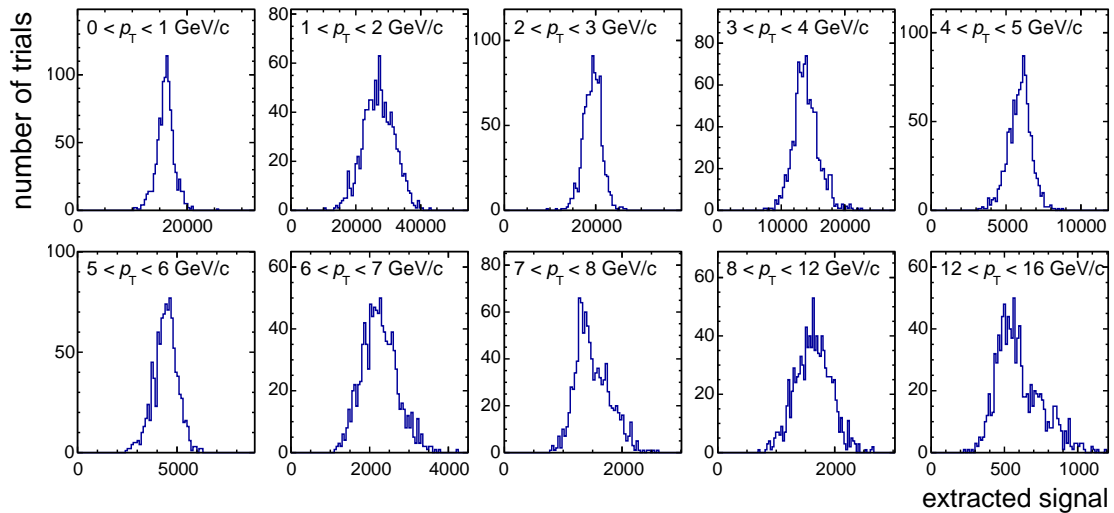


Figure 5.11: Distribution of the extracted raw yield, using the multi-trial approach with one thousand random parameter configurations, as described in the text.

the fit range is drawn from a uniform distribution in the range  $\mu_{MC} - 12\sigma_{MC}$  up to  $\mu_{MC} - 8\sigma_{MC}$ ; the upper value of the fit range is drawn from a uniform distribution in the range  $\mu_{MC} + 8\sigma_{MC}$  up to  $\mu_{MC} + 12\sigma_{MC}$ . Asymmetric fit ranges are thus also accepted. The peak parameter  $\sigma$  is varied using a Gaussian distribution around  $\sigma_{MC}$  with a width of  $\pm 20\%$ .

In fig. 5.11, the resulting  $D^0$  yields from one thousand trials are plotted in a histograms for each  $p_T$  bin. The final  $D^0$  raw yields are taken as the mean of these distributions. The systematic uncertainty is taken as the standard deviation. The statistical uncertainty is taken from the mean of the resulting statistical uncertainties from all trials. The final raw values are listed in table 5.2 in section 5.9, along with the extracted statistical and systematic uncertainties.

## 5.7 Efficiency Correction

The raw  $D^0$  yield must be corrected by the efficiency of the reconstruction and the selection. The corrected yield,  $N_{\text{corr}}$ , is obtained by dividing the raw yield,  $N_{\text{raw}}$ , by the efficiency correction,  $c_{\alpha \times \epsilon}$ :

$$N_{\text{corr}} = N_{\text{raw}}/c_{\alpha \times \epsilon} \quad (5.10)$$

The efficiency correction is a number between zero and one. It can be viewed as the probability for a  $D^0$  that is created in the collision to be actually reconstructed in the detector and selected in the analysis. In this analysis, the efficiency correction is factorised into a purely geometric acceptance and a reconstruction and selection efficiency. A  $D^0$  decay daughter is called ‘accepted’ if it survives the kinematic cuts (TS9 and TS10 in table 5.1). The term ‘acceptance’ can then be defined as the probability for a kinematic configuration such that both decay daughters are accepted. The ‘reconstruction and selection efficiency’ then refers to the probability that a  $D^0$  with two accepted decay daughters is actually reconstructed and selected in the analysis. The efficiency correction can be determined to a certain precision in a simulation with high statistics using ratios of total numbers of  $D^0$  mesons:

$$c_{\alpha \times \epsilon} = \frac{N_{\text{gen, acc}}^1}{N_{\text{gen}}^1} \times \frac{N_{\text{reco}}^2}{N_{\text{gen, acc}}^2} \quad (5.11)$$

Here,  $N_{\text{gen}}$  and  $N_{\text{reco}}$  refer to the number of generated and reconstructed  $D^0$  mesons in a certain region of phase space and  $N_{\text{gen, acc}}$  denotes the number of generated  $D^0$  mesons the daughters of which are accepted. The indices 1 and 2 indicate that different frameworks are used for the two factors of the efficiency correction. The acceptance is a purely kinematic quantity and can as such be simulated using simple four-vector kinematics. In this thesis, the toy MC, described in section 4.2.5, is used for this purpose. The results were checked with those from the Monte Carlo simulation described below and were found to agree within the statistical uncertainty of the MC simulation. The advantage of the toy MC is a higher precision due to the much larger number of generated  $D^0$  mesons. Furthermore, the simulation provides a cross check for the more complicated MC framework.

In contrast to the case of the kinematic acceptance, a full detector description is needed to determine the reconstruction and selection efficiency. Events are simulated using PYTHIA [70, 71]. The generated particles are then propagated through the detector using the GEANT3 package [78]. The same analysis task is run on MC as in real data in order to ensure that the same cuts and PID are applied. A charm enriched MC sample is used in order to enhance statistics.

Figure 5.12 shows the acceptance, the reconstruction and selection efficiency and the total correction factor. The efficiency rises from about 0.2 at low  $p_T$  to about 0.65 at

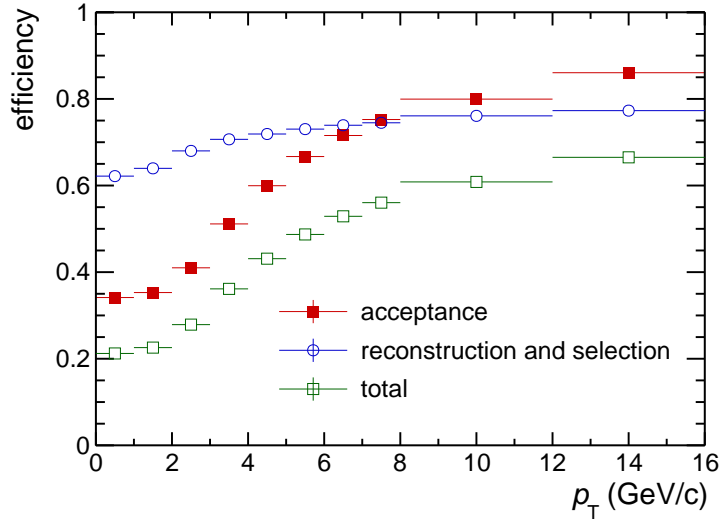


Figure 5.12: Acceptance and efficiency for the selections specified in previous chapters.

high  $p_T$ , where the shape is mainly dominated by the shape of the acceptance. Towards zero  $p_T$ , the efficiency flattens off at a relatively high value of 0.2, in contrast to the topological analysis, where the efficiency drastically drops to zero.

## 5.8 Feed-Down Correction

The raw  $D^0$  yields are contaminated with a certain fraction of  $D^0$  mesons from B meson decays of the form

$$B \rightarrow D^0 + X, \quad (5.12)$$

where B is any type of B meson and X is any other combination of particles. This contribution to the  $D^0$  yield is denoted feed-down. The feed-down contribution from the  $\Lambda_b$  baryon is negligible due to the low branching ratio of  $\Lambda_b \rightarrow D^0 + X$  of about  $6 \times 10^{-4}$  [23, 79].

In order to quote a cross section for prompt  $D^0$  production, the feed-down from B mesons must be subtracted. For this purpose, the prompt fraction,  $f_{\text{prompt}}$ , is defined as the ratio of the number of prompt  $D^0$  mesons,  $N_{\text{prompt}}$ , over the measured raw yield,  $N_{\text{raw}}$ , including the contribution from feed-down,  $N_{\text{feed-down}}$ , in a given region of phase

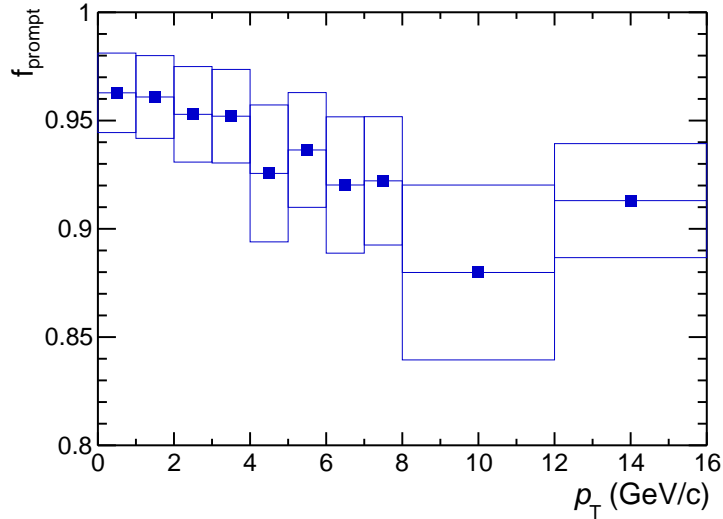


Figure 5.13: The fraction of prompt  $D^0$  production over the total  $D^0$  production. The feed-down component of the raw yield is determined using FONLL calculations with the full theoretical uncertainty included.

space:

$$f_{\text{prompt}} = \frac{N_{\text{prompt}}}{N_{\text{raw}}} = 1 - \frac{N_{\text{feed-down}}}{N_{\text{raw}}}. \quad (5.13)$$

The prompt fraction enters into the cross section as a correction factor between zero and one, where a value of one signifies no contamination from feed-down and a value of zero signifies full contamination.

As no direct mid-rapidity measurement of the  $b\bar{b}$  cross section at low momentum for pp collisions at  $\sqrt{s} = 7$  TeV is available, FONLL predictions [17] are used to determine  $N_{\text{feed-down}}$ .

$$N_{\text{feed-down}} = 2 \cdot 2Y \cdot \Delta p_T \cdot c_{\alpha \times \epsilon} \cdot \mathcal{B} \cdot \mathcal{L}_{\text{int}} \cdot \left. \frac{d\sigma_{\text{FONLL}}^{D^0 \text{ from B}}}{dp_T} \right|_{|y| < 0.5} \quad (5.14)$$

This formula is obtained by taking eq. (5.15) and substituting  $N_{\text{raw}}$  by  $N_{\text{feed-down}}$  and the  $D^0$  cross section by the FONLL cross section for  $D^0$  from B; and solving for  $N_{\text{feed-down}}$ . The involved symbols are explained in section 5.9.

Figure 5.13 presents the prompt fraction in the full analysed  $p_T$  range. The horizontal lines indicate the  $p_T$  bin width and the boxes the systematic uncertainty. The prompt fraction decreases from about 0.96 in the lowest  $p_T$  bin to around 0.9 for higher  $p_T$  bins.

The decrease is explained by the fact that the B meson  $p_T$  spectra are harder than the  $D^0$  spectrum, meaning they are shifted towards higher transverse momenta. The fluctuations in the prompt fraction are due to the fluctuations in the raw yield, which is involved in the definition of  $f_{\text{prompt}}$  in eq. (5.13).

A distinct advantage as compared to the topological analysis are the equal efficiencies for prompt and feed-down  $D^0$  mesons. In the topological analysis, the feed-down efficiency is considerably higher than the prompt efficiency due to the longer lifetimes of B mesons in comparison to  $D^0$  mesons. The feed-down is consequently enhanced by the topological selection and the prompt fraction resides in a lower range between about 0.8 and 0.9. A higher feed-down efficiency as compared to the prompt efficiency translates linearly into a higher uncertainties of the prompt fraction. In the lowest  $p_T$  bin of the topological analysis,  $p_T \ 1 < p_T < 2 \text{ GeV}/c$ , the efficiencies differ by a factor of three. With the new analysis approach presented in this thesis, the uncertainty is thus decreased by a factor of three at low  $p_T$ .

## 5.9 Calculation of the Cross Section

With the output from the different analysis steps described in the previous sections, the  $p_T$ -differential  $D^0$  production cross section at central rapidity,  $|y| < 0.5$ , is calculated using the following formula:

$$\left. \frac{d\sigma^{D^0}}{dp_T} \right|_{|y|<0.5} = \frac{1}{2} \frac{1}{2Y \Delta p_T(p_T)} \frac{f_{\text{prompt}} \cdot N_{\text{raw}}(p_T)}{c_{\alpha \times \epsilon}} \Big|_{|y|<Y} \frac{1}{\mathcal{B} \cdot \mathcal{L}_{\text{int}}}. \quad (5.15)$$

The factor of one half accounts for the fact that, according to an ALICE convention, the cross section is quoted for particles only, whereas the raw yield contains both  $D^0$  and  $\bar{D}^0$ , making the assumption of equal yields for particles and antiparticles at the high LHC energies. The transverse momentum bin width is denoted by  $\Delta p_T$ . Following a convention of ALICE results for D-meson production, the cross section is given in the rapidity interval  $|y| < 0.5$ . It must therefore be scaled down by the measured rapidity window  $2Y$ , where  $Y = 0.8$  is the rapidity cut applied on  $D^0$  candidates in the analysis (cf. section 5.4). The simple rapidity scaling is justified since the rapidity distribution of  $D^0$  mesons in pp collisions at  $\sqrt{s} = 7 \text{ TeV}$  is considered flat within 1% (cf. section 4.2.5).

$p_T$ bin (GeV/ $c$ )	$N_{\text{raw}} \pm \text{stat.} \pm \text{syst.}$	$c_{\alpha \times \epsilon} \pm \text{stat.} \pm \text{syst.}$	$f_{\text{prompt}} \pm \text{syst.}$
0-1	$16060 \pm 5102 \pm 1588$	$0.212 \pm 0.001 \pm 0.020$	$0.963 \pm 0.018$
1-2	$27044 \pm 5648 \pm 4804$	$0.226 \pm 0.001 \pm 0.021$	$0.961 \pm 0.019$
2-3	$19294 \pm 3840 \pm 1995$	$0.279 \pm 0.001 \pm 0.024$	$0.953 \pm 0.022$
3-4	$13917 \pm 2244 \pm 2023$	$0.361 \pm 0.001 \pm 0.031$	$0.952 \pm 0.022$
4-5	$5906 \pm 1298 \pm 771$	$0.431 \pm 0.002 \pm 0.037$	$0.926 \pm 0.032$
5-6	$4418 \pm 785 \pm 599$	$0.487 \pm 0.002 \pm 0.042$	$0.936 \pm 0.026$
6-7	$2250 \pm 508 \pm 451$	$0.529 \pm 0.003 \pm 0.045$	$0.920 \pm 0.031$
7-8	$1502 \pm 356 \pm 291$	$0.560 \pm 0.003 \pm 0.048$	$0.922 \pm 0.030$
8-12	$1629 \pm 374 \pm 302$	$0.608 \pm 0.002 \pm 0.052$	$0.880 \pm 0.040$
12-16	$599 \pm 160 \pm 154$	$0.665 \pm 0.004 \pm 0.057$	$0.913 \pm 0.026$

Table 5.2: The collected input for the calculation of the cross section. The raw yield,  $N_{\text{raw}}$ , the efficiency correction,  $c_{\alpha \times \epsilon}$ , and the prompt fraction,  $f_{\text{prompt}}$ , are listed for all analysed  $p_T$  bins with the respective uncertainties. For the systematic uncertainty of the efficiency correction, the tracking and PID uncertainties (cf. section 6.2) were combined in quadrature.

The raw yield,  $N_{\text{raw}}$ , is corrected by the prompt fraction,  $f_{\text{prompt}}$ , and the efficiency correction,  $c_{\alpha \times \epsilon}$ . The values and uncertainties for  $N_{\text{raw}}$ ,  $c_{\alpha \times \epsilon}$  and  $f_{\text{prompt}}$  are given in table 5.2 for all analysed  $p_T$  bins. The yield is further divided by the integrated luminosity,  $\mathcal{L}_{\text{int}} = 5.25 \text{ nb}^{-1}$ , and the combined branching ratio,  $\mathcal{B} = 3.89\%$ , for the analysed decays  $D^0 \rightarrow K^- \pi^+$  and  $D^0 \rightarrow K^+ \pi^-$  (cf. section 4.1).

## UNCERTAINTIES

---

This chapter presents an exhaustive summary of the considered statistical and systematic uncertainties on the  $D^0$  production cross section. For practical reasons, most of the contributions to the statistical and systematic uncertainties were already described in the previous chapter. For these cases, a short summary is given and the respective section is referenced.

## 6.1 Statistical Uncertainties

The following sources of statistical uncertainty for the  $D^0$  production cross section were considered. The corresponding quantity from eq. (5.15) is given in parentheses.

- signal extraction ( $N_{\text{raw}}$ )
- efficiency correction ( $c_{\alpha \times \epsilon}$ )

The statistical uncertainties on the extracted raw yields were determined from the invariant mass fits, using the randomised multi-trial approach described in section 5.6.4.

The statistical uncertainty in the efficiency correction is due to the limited available statistics in the Monte Carlo sample that was used to determine the reconstruction and selection efficiency (cf. section 5.7). It was determined by propagating the binomial uncertainties in the ratio of the reconstructed to the generated  $D^0$  mesons in eq. (5.11).

$p_T(\text{GeV}/c)$	0-1	1-2	2-3	3-4	4-5	5-6	6-7	7-8	8-12	12-16
signal extraction	31.8	20.9	19.9	16.1	22.0	17.8	22.6	23.7	22.9	26.6
efficiency correction	0.3	0.3	0.3	0.3	0.4	0.4	0.5	0.6	0.4	0.6
overall	31.8	20.9	19.9	16.1	22.0	17.8	22.6	23.7	23.0	26.6

Table 6.1: Summary of the statistical uncertainties of the  $D^0$  production cross section in percent.

The overall statistical uncertainty of the  $D^0$  production cross section was obtained by summing the two contributions in quadrature. The resulting values are given in table 6.1, along with those of the single contributions. The statistical uncertainty of the efficiency correction is completely negligible for all of the analysed  $p_T$  bins.

## 6.2 Systematic Uncertainties

The following sources of systematic uncertainty on the  $D^0$  production cross section were studied. The corresponding quantity from eq. (5.15) is given in parentheses.

- signal extraction ( $N_{\text{raw}}$ )
- efficiency correction ( $c_{\alpha \times \epsilon}$ ):
  - track reconstruction and selection
  - particle identification
  - MC input  $p_T$  shape
- feed-down from B ( $f_{\text{prompt}}$ )
- branching ratio ( $\mathcal{B}$ )
- integrated luminosity ( $\mathcal{L}_{\text{int}}$ )

The systematic uncertainty related to the signal extraction was evaluated varying the relevant fit parameters in a randomised multi-trial approach, as described in section 5.6.4.

For the systematic uncertainty of the efficiency correction, the following three sources were considered: the track reconstruction and selection; the particle identification; and the initially unknown  $D^0$  meson  $p_T$  spectrum that has to be provided as an input to the MC simulations. The systematic uncertainty related to the track reconstruction, also referred to as the tracking uncertainty, is inherited from the topological analysis, where

almost the same track selection was used [11]. The only significant difference between the selections is the absence of the SPD requirement in this analysis, as highlighted in section 5.4. It is reasonable to assume that not using this rather stringent cut decreases the uncertainty, as the tracking efficiency in MC is then less dependent on the correct representation of the SPD acceptance. The uncertainty inherited from the topological analysis can thus rather be seen as an upper limit for this analysis. In [11], the tracking uncertainty was determined by varying chosen track selection cuts and evaluating the variation in the cut selection efficiency. The maximum deviation of the resulting cut selection efficiency for the alternative selection from the standard cut set was then quoted as the uncertainty of the tracking. The resulting value is 4% per track. As the uncertainties are assumed to be fully correlated between the two tracks used in the analysis, a  $p_T$ -independent uncertainty of 8% is therefore assigned for the tracking efficiency.

The uncertainty of the PID efficiency is also taken from the standard topological approach, where the same PID strategy was used. As the PID selection is performed on a single-track basis, its uncertainty should not be influenced by the topological selection, which is applied to the track pair afterwards. The uncertainty was estimated in [11] by comparing the corrected yields for a selection with and without PID. Such an approach is principally not feasible in this analysis, as signal extraction is not possible without PID.

In the determination of the efficiency correction, as described in section 5.7, a prediction of the  $D^0$  transverse momentum spectrum must be provided as an input for the MC simulations. To evaluate the effect of the specific choice of  $p_T$  shape, the acceptance was simulated using a flat  $p_T$  distribution instead of the FONLL  $p_T$  spectrum. The resulting values for the acceptance differed on a sub-percent level in all  $p_T$  bins. The effect can be assumed not to be much larger when the total efficiency correction instead of only the acceptance is studied, since the reconstruction and selection efficiency is much flatter in  $p_T$  than the acceptance (cf. fig. 5.12). The uncertainty of the input MC  $p_T$  shape is therefore neglected.

The systematic uncertainty of the fraction of prompt  $D^0$  mesons is determined by a full propagation of the theoretical uncertainty of the FONLL B meson production cross section that is used in eq. (5.14).

$p_T(\text{GeV}/c)$	0-1	1-2	2-3	3-4	4-5	5-6	6-7	7-8	8-12	12-16
signal extraction	9.9	17.8	10.3	14.5	13.0	13.6	20.1	19.4	18.5	25.6
tracking	8.0	8.0	8.0	8.0	8.0	8.0	8.0	8.0	8.0	8.0
PID	5.0	5.0	3.0	3.0	3.0	3.0	3.0	3.0	3.0	3.0
feed-down	1.9	2.0	2.3	2.3	3.4	2.8	3.4	3.2	4.6	2.9
overall	13.8	20.2	13.6	17.0	16.0	16.3	22.1	21.4	20.9	27.2

Table 6.2: Summary of the systematic uncertainties on the  $D^0$  production cross section.

The relative uncertainty of the branching ratio is 1.3% [23] and the relative uncertainty of the integrated luminosity 3.5% [75]. The uncertainties of the branching ratio and of the integrated luminosity are global uncertainties that are fully correlated between the  $p_T$  bins. They are therefore treated separately.

The signal extraction, tracking, PID and feed-down uncertainties are possibly partially correlated between the  $p_T$  bins, but are assumed to be uncorrelated with each other. They are thus summed in quadrature to obtain the overall systematic uncertainty for each  $p_T$  bin. The systematic uncertainties are summarised in table 6.2. The overall uncertainties range from about 14% to 28%. The signal extraction uncertainty is the dominant contribution in all  $p_T$  bins.

## RESULTS

---

In this chapter, the results for  $D^0$  production in pp collisions obtained in this thesis are discussed. The  $p_T$ -differential cross section is shown and compared with the results from the topological approach. In the second part of the chapter, the  $p_T$ -integrated cross section is presented and compared with different measurements.

## 7.1 $D^0$ Production Cross Section

Figure 7.1 presents the  $D^0$  production cross section for pp collisions at  $\sqrt{s} = 7$  TeV. The new values obtained in this work without topological selection (blue) are plotted along with those from the topological analysis (orange) [11]. The lower panel shows the ratio of the two measurements for  $p_T > 1$  GeV/ $c$ . The horizontal bars indicate the  $p_T$  bin width. The vertical bars represent the overall statistical uncertainty and the open boxes the overall systematic uncertainty. The fully correlated systematic uncertainties are not included in the plot, following the convention of ALICE publications of D meson production [11–13]. The shaded yellow boxes represent the uncertainty band of the FONLL theory prediction for  $D^0$  production [56], which are shown for comparison with the measurements. The values of the plotted cross sections from both analyses are given in table 7.1 along with the absolute and relative statistical and systematic uncertainties.

The new data point for  $p_T < 1$  GeV/ $c$  closes the gap towards zero transverse momentum. It conforms well into the trend observed for  $p_T > 1$  GeV/ $c$ , lying in the upper part of

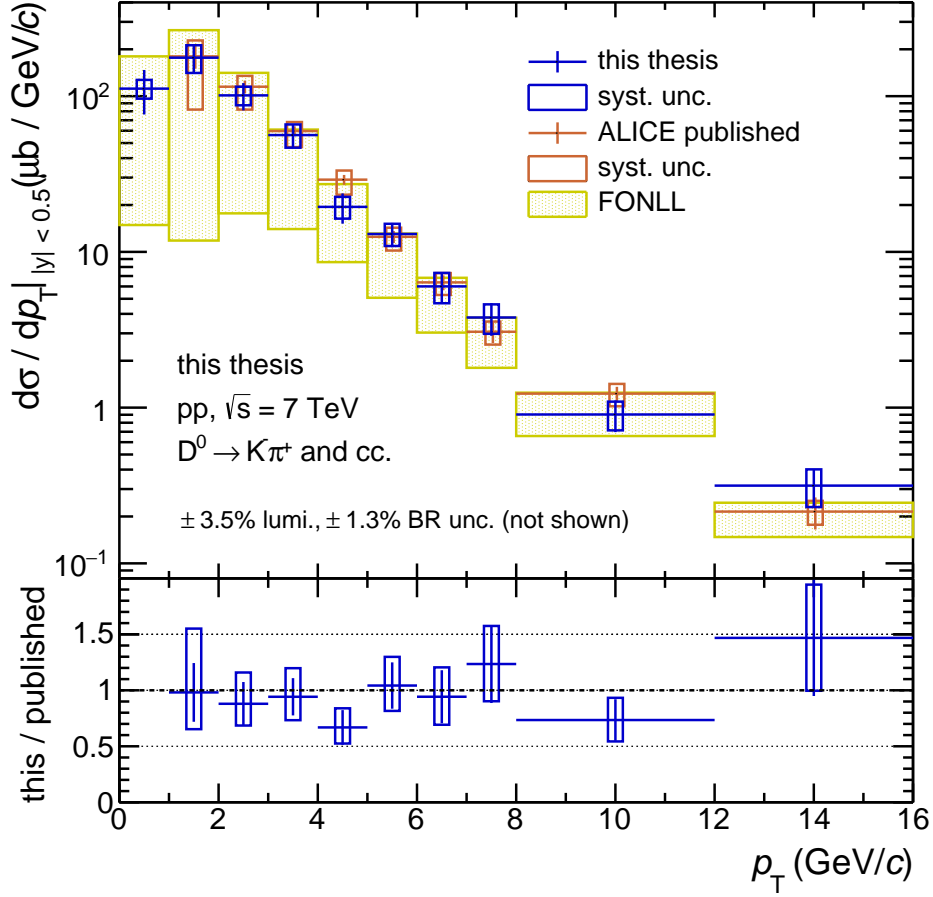


Figure 7.1: Transverse momentum dependence of the  $D^0$  production cross section at mid-rapidity in pp collisions at  $\sqrt{s} = 7$  TeV. The values from the topological analysis [11] are plotted for comparison along with the FONLL theoretical prediction [56]. The overall statistical uncertainties are represented by vertical lines, the systematic uncertainties by open boxes. The global uncertainties of the luminosity and the branching ratio not included in the overall systematic uncertainty. The horizontal lines indicate the  $p_T$  bin width.

$p_T$ interval (GeV/ $c$ )	$d\sigma/dp_T _{ y <0.5} \pm \text{stat.} \pm \text{syst.}$ ( $\mu\text{b}/\text{GeV}/c$ )	
	this analysis	topological analysis
0-1	$112 \pm 36$ (32%) $\pm 15$ (14%)	-
1-2	$177 \pm 37$ (21%) $\pm 36$ (20%)	$180 \pm 30$ (17%) <sup>+48 (27%)</sup> <sub>-98 (54%)</sub>
2-3	$101 \pm 20$ (20%) $\pm 14$ (14%)	$115 \pm 11$ (10%) <sup>+20 (17%)</sup> <sub>-33 (29%)</sub>
3-4	$56.3 \pm 9.1$ (16%) $\pm 9.6$ (17%)	$59.7 \pm 4.3$ (7%) <sup>+8.5 (14%)</sup> <sub>-12.6 (21%)</sub>
4-5	$19.5 \pm 4.3$ (22%) $\pm 3.1$ (16%)	$29.1 \pm 2.1$ (7%) <sup>+4.2 (14%)</sup> <sub>-5.8 (20%)</sub>
5-6	$13.0 \pm 2.3$ (18%) $\pm 2.1$ (16%)	$12.5 \pm 1.1$ (9%) <sup>+1.8 (14%)</sup> <sub>-2.3 (18%)</sub>
6-7	$6.00 \pm 1.36$ (23%) $\pm 1.32$ (22%)	$6.37 \pm 0.70$ (11%) <sup>+0.94 (15%)</sup> <sub>-1.08 (17%)</sub>
7-8	$3.79 \pm 0.90$ (24%) $\pm 0.81$ (21%)	$3.07 \pm 0.47$ (15%) <sup>+0.50 (16%)</sup> <sub>-0.53 (17%)</sub>
8-12	$0.90 \pm 0.21$ (23%) $\pm 0.19$ (21%)	$1.23 \pm 0.13$ (11%) <sup>+0.19 (15%)</sup> <sub>-0.21 (17%)</sub>
12-16	$0.316 \pm 0.084$ (27%) $\pm 0.086$ (27%)	$0.215 \pm 0.050$ (23%) <sup>+0.037 (17%)</sup> <sub>-0.038 (18%)</sub>

Table 7.1:  $D^0$  production cross section in pp collisions at  $\sqrt{s} = 7$  TeV, as obtained with this analysis (left) and with the topological analysis [11] (right). The relative statistical and systematic uncertainties are given in parentheses.

the FONLL uncertainty range. The new measurement is consistent with the topological measurement within their respective total uncertainties. In this context, it is important to notice that the measurements can be regarded as only partially correlated, as the raw  $D^0$  yields in this analysis are larger by about a factor of ten at low  $p_T$  and a factor of five at high  $p_T$ , thus resulting only in a small overlap between the analyses. The systematic difference of 0.5 % due to the different branching ratios in use (cf. section 4.1) is evidently negligible. The mean relative deviation of the two measurements of about 18 % compares well with the order of magnitude of the statistical and systematic uncertainties. In summary, this also provides an excellent verification of the topological D-meson measurements with ALICE.

For the new analysis, the statistical uncertainty is larger in all  $p_T$  bins by up to about a factor of two, whereas the systematic uncertainty is significantly lower for  $p_T < 3$  GeV/ $c$  and of comparable size up to  $p_T < 6$  GeV/ $c$ . This corresponds to the behaviour expected ‘by design’ of the two methods. The topological approach is clearly limited by the systematics of the topological selection, the feed-down and the signal extraction. The new approach is limited by the statistical uncertainty, which becomes particularly clear in the new  $p_T$  bin  $0 < p_T < 1$  GeV/ $c$ , where the statistical uncertainty is more than

twice the size of the systematic uncertainty. In terms of the overall combined statistical and systematic uncertainty, the presented analysis is superior to the topological analysis up to  $p_T = 2 \text{ GeV}/c$  for the upper uncertainty and up to  $p_T = 3 \text{ GeV}/c$  for the lower uncertainty.

## 7.2 Total Charm Production Cross Section

With the measurement presented in this thesis, it is possible to quote the  $p_T$ -integrated charm production cross section at mid-rapidity without extrapolation to low transverse momentum. For this purpose, the  $D^0$  cross section is integrated in the measured momentum range. The cross section values from the analysed  $p_T$  bins are added together, propagating the uncorrelated statistical (stat.) and systematic (syst.) uncertainties, as well as the correlated uncertainties of luminosity (lum.) and branching ratio ( $\mathcal{B}$ ) accordingly. The contribution to the  $p_T$ -integrated  $D^0$  production cross section from the  $p_T$  range above the measured limit of  $16 \text{ GeV}/c$  can be safely neglected (cf. section 2.5). The resulting  $p_T$ -integrated  $D^0$  production cross section at mid-rapidity,  $|y| < 0.5$ , is:

$$d\sigma_{\text{this}}^{D^0}/dy = 489 \pm 56 (\text{stat.}) \pm 43 (\text{syst.}) \pm 17 (\text{lum.}) \pm 6(\mathcal{B}) \mu\text{b}. \quad (7.1)$$

The corresponding published result from the topological analysis [11] includes a rather large additional uncertainty from the extrapolation to zero transverse momentum (extr.). The reported result is:

$$d\sigma_{\text{publ.}}^{D^0}/dy = 516 \pm 41 (\text{stat.}) {}^{+69}_{-175} (\text{syst.}) \pm 18 (\text{lum.}) \pm 7(\mathcal{B}) {}^{+120}_{-37} (\text{extr.}) \mu\text{b}. \quad (7.2)$$

Adding up the single types of uncertainties in quadrature, the results with their overall uncertainties are:

$$d\sigma_{\text{this}}^{D^0}/dy = 489 \pm 73 (\text{overall}) \mu\text{b}, \quad (7.3)$$

$$d\sigma_{\text{publ.}}^{D^0}/dy = 516 {}^{+146}_{-185} (\text{overall}) \mu\text{b}. \quad (7.4)$$

The results from the two different measurements are perfectly consistent. Without the topological analysis, the overall relative uncertainty is considerably reduced from  $+28\%$  and  $-36\%$  down to  $\pm 15\%$ .

The  $p_T$ -integrated charm production cross section at mid-rapidity can be derived by dividing the  $D^0$  result by the fragmentation fraction of charm to  $D^0$ ,  $f(c \rightarrow D^0) = 0.557 \pm 0.023$  (cf. section 2.3). The uncertainty of this fraction has to be added as an additional source of uncertainty on the cross section (FF). The resulting charm cross section at mid-rapidity is:

$$\begin{aligned} d\sigma_{\text{this}}^{c\bar{c}}/dy &= 879 \pm 101 \text{ (stat.)} \pm 76 \text{ (syst.)} \pm 31 \text{ (lum.)} \pm 11 \text{ (}\mathcal{B}\text{)} \pm 36 \text{ (FF)} \mu\text{b} \\ &= 879 \pm 135 \text{ (overall)} \mu\text{b}. \end{aligned} \quad (7.5)$$

The  $p_T$ -integrated result is further extrapolated to the full phase space. For this purpose, the same extrapolation method as in [12] is applied. An extrapolation factor of  $8.56_{-0.42}^{+2.51}$  is obtained as the ratio of the FONLL prediction for  $D^0$  production in the full phase space to the prediction for the measured central rapidity region. The uncertainty of the extrapolation factor is determined by varying the renormalisation and factorisation scale parameters, the charm quark mass and the PDFs as described in section 2.5. The resulting total charm cross section for the measurement presented in this thesis is:

$$\begin{aligned} \sigma_{\text{this}}^{c\bar{c}} &= 7.5 \pm 0.9 \text{ (stat.)} \pm 0.7 \text{ (syst.)} \pm 0.3 \text{ (lum.)} \pm 0.1 \text{ (}\mathcal{B}\text{)} \pm 0.3 \text{ (FF)}_{-0.4}^{+2.2} \text{ (extr.)} \text{ mb} \\ &= 7.5_{-1.2}^{+2.5} \text{ (overall)} \text{ mb}. \end{aligned} \quad (7.6)$$

In fig. 7.2 and table 7.2, the measurement is compared with the ALICE result using the topological approach [12] and results from the LHCb [69] and ATLAS [80, 81] collaborations. The total charm cross section was determined measuring the production of charmed hadrons in different  $p_T$  and  $y$  ( $\eta$ ) ranges, as indicated in table 7.2. For the results involving more than one species, the charm cross section is quoted as the average of the measurements. The LHCb measurement in the visible cross section was extrapolated using the extrapolation factor from [42]. When considering the result of this thesis, the overall uncertainties of the total charm production cross section measured with ALICE are halved as compared to the topological analysis. The data point moves down, yielding a better consistency with the results of LHCb and ATLAS.

The energy dependence of the total nucleon-nucleon charm cross section is shown in fig. 7.3. Data points from various experiments are plotted [12, 20, 69, 80–83]. The measurements of the charm cross section conform well to the trend of a next-to-leading order (NLO) calculation [84] over a wide energy range.

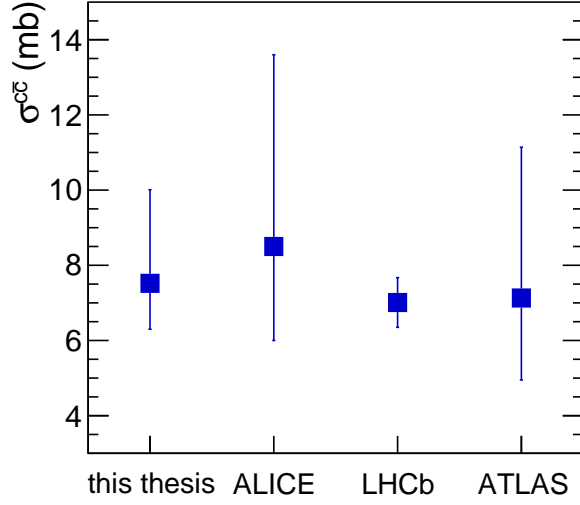


Figure 7.2: LHC measurements of the total charm production cross section in pp collisions at  $\sqrt{s} = 7$  TeV. The result from this thesis compares well with the ALICE measurement using topological selection [12], as well as with results from LHCb [69] and ATLAS [80, 81].

	measured species	$p_T$ range	$y/\eta$ range	$\sigma^{c\bar{c}}$ (mb)
this thesis	$D^0$	$0 < p_T < 16$ GeV/ $c$	$ y  < 0.8$	7.52 $^{+2.49}_{-1.22}$
ALICE	$D^0, D^+, D^{*+}$	$1 < p_T < 16(24)$ GeV/ $c$	$ y  < 0.8$	8.5 $^{+5.1}_{-2.5}$
LHCb	$D^0, D^+, D^{*+}, D_s^+, \Lambda_c^+$	$0 < p_T < 8$ GeV/ $c$	$2 < y < 4.5$	7.01 $\pm$ 0.66
ATLAS	$D^+, D^{*+}, D_s^+$	$p_T > 3.5$	$ \eta  < 2.1$	7.13 $^{+4.01}_{-2.18}$

Table 7.2: LHC measurements of the total charm production cross section in pp collisions at  $\sqrt{s} = 7$  TeV. The result from this thesis is given along with the results from the ALICE measurement using topological selection [12], and results from LHCb [69] and ATLAS [80, 81]. The measured D meson species, the  $p_T$  and the  $y$  or  $\eta$  range are also indicated.

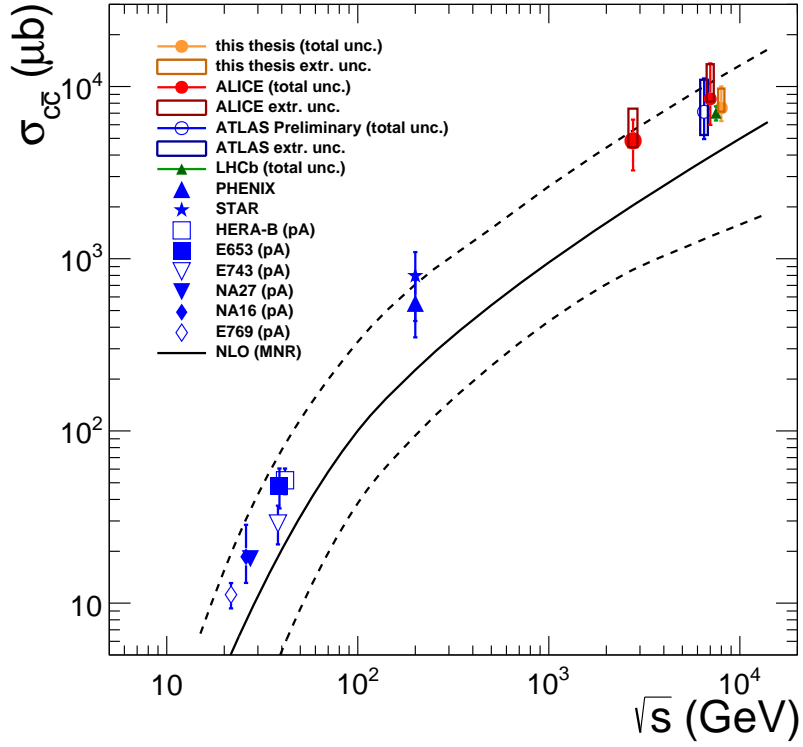


Figure 7.3: Total charm cross section in nucleon-nucleon collisions as a function of the centre-of-mass energy. The result obtained in this thesis is shown along with data points from various experiments [12, 20, 69, 80–83]. For measurements using proton-nucleus (pA) collisions, the cross section was scaled down by the number of binary collisions. The four LHC data points at  $\sqrt{s} = 7$  TeV are horizontally displaced with respect to each other for better visibility. The next-to-leading order MNR calculation is shown [84] with the solid (dashed) black line(s) indicating the central value and the uncertainty band. This figure is adapted from [12].

## SUMMARY AND OUTLOOK

---

The cross section of prompt  $D^0$  production at mid-rapidity in proton-proton collisions was measured down to zero transverse momentum for the first time at the LHC, providing an important baseline for the study of the low-momentum phenomenology of heavy quarks in the quark-gluon plasma as well as for the investigation of charmonium production in heavy-ion collisions. The full kinematic reconstruction of D mesons at low  $p_T$  is particularly challenging as a topological approach can not be adopted due to the small Lorentz boost of a low-momentum D meson. An alternative analysis strategy was thus developed in this thesis to extend the measurement of  $D^0$  production down to zero transverse momentum.

$D^0$  mesons were reconstructed with an invariant mass analysis in the  $D^0 \rightarrow K^- \pi^+$  decay channel using a data sample of pp collisions at  $\sqrt{s} = 7$  TeV with an integrated luminosity  $\mathcal{L}_{\text{int}} = 5.25 \text{ nb}^{-1}$ , collected with a minimum-bias trigger in 2010. Particle identification in the TPC and TOF detectors was exploited in order to improve the signal-to-background ratio. Large parts of the combinatorial background could then be subtracted using the like-sign technique.

The  $p_T$ -differential cross section for prompt  $D^0$  production was found to be consistent with the topological analysis in the overlapping  $p_T$  region. The new data point for  $p_T < 1 \text{ GeV}/c$  lies in the upper range of the FONLL prediction, supporting the trend observed in the higher  $p_T$  intervals. It is intrinsic to the different methods that the topological analysis is rather limited by the systematic uncertainty, whereas the new analysis is limited in the statistical uncertainty. Combining the statistical and systematic

uncertainties in quadrature, the results from the analysis presented in this thesis are more precise than those of the topological measurement for  $p_T < 3 \text{ GeV}/c$  ( $p_T < 2 \text{ GeV}/c$ ) in terms of the lower (upper) uncertainty. For  $p_T < 1 \text{ GeV}/c$  it is obviously superior, as no data is available for the topological analysis.

Based on the presented  $D^0$  measurement, the  $p_T$ -integrated charm production cross section at mid-rapidity can be given without extrapolation. The cross section and its overall uncertainty were determined to be  $d\sigma^{c\bar{c}}/dy = (879 \pm 135) \mu\text{b}$ . The relative overall uncertainty of 15 % signifies an increase in precision by about a factor of two, as compared to the previous measurement [12]. Models of charmonium production in heavy-ion collisions [18, 19], for which  $d\sigma^{c\bar{c}}/dy$  is an important input parameter, will benefit greatly from this increase in precision. The  $p_T$ -integrated charm cross section at mid-rapidity was extrapolated to the full phase space and compared to other LHC experiments, where good agreement was found.

An analysis using the same strategy as in this thesis is currently being performed in the p–Pb collision system. A comparison of the pp and the p–Pb measurements down to zero transverse momentum will thus soon become possible, providing important information to disentangle experimental observations in Pb–Pb collisions that are due to the hot and dense matter from those arising from initial-state effects. Meanwhile, the measurement of D mesons in Pb–Pb collisions without topological selection is probably not feasible using the currently available data sets due to the large background. With the tenfold statistics expected for the LHC Run II starting in 2015, the measurement of D mesons at low  $p_T$  in Pb–Pb collisions without topological selection may become possible.

In the long term, the logical follow-up of D-meson measurements would be the direct kinematic reconstruction of B mesons. Currently, this is foreseen as part of the ALICE physics programme for Run III, scheduled for 2020. With the upgrade of the Inner Tracking System [85], a significantly improved precision of the vertex separation is expected. The topological selection might thus be extended to much lower  $p_T$  values than are currently possible. In the meantime, it would be worth attempting a direct reconstruction of B mesons in the upcoming Run II, both with the topological approach and with the alternative approach presented in this thesis. The direct measurement of low-momentum B meson production at mid-rapidity would signify a major leap forward in the study of heavy-quark production in the Quark-Gluon Plasma.

## BIBLIOGRAPHY

---

- [1] S. Glashow. Partial-symmetries of weak interactions. *Nucl. Phys.*, 22(4):579–588, 1961. doi:10.1016/0029-5582(61)90469-2.
- [2] S. Weinberg. A model of leptons. *Phys. Rev. Lett.*, 19(1264), 1967. doi:10.1103/PhysRevLett.19.1264.
- [3] A. Salam. Weak and electromagnetic interactions. In N. Svartholm, editor, *Elementary particle physics: relativistic groups and analyticity*, page 367. Almqvist and Wiskell, 1968.
- [4] G. 't Hooft and M. Veltman. Regularization and renormalization of gauge fields. *Nucl. Phys. B*, 44(1):189–213, 1972. doi:10.1016/0550-3213(72)90279-9.
- [5] ATLAS Collaboration. Observation of a new particle in the search for the standard model higgs boson with the ATLAS detector at the LHC. *Phys. Lett. B*, 716:1–29, 2012. arXiv:1207.7214, doi:10.1016/j.physletb.2012.08.020.
- [6] CMS Collaboration. Observation of a new boson at a mass of 125 GeV with the CMS experiment at the LHC. *Phys. Lett. B*, 716:30, 2012. arXiv:1207.7235, doi:10.1016/j.physletb.2012.08.021.
- [7] F. Englert and R. Brout. Broken symmetry and the mass of gauge vector mesons. *Phys. Rev. Lett.*, 13:321, 1964. doi:10.1103/PhysRevLett.13.321.
- [8] P. W. Higgs. Broken symmetries, massless particles and gauge fields. *Phys. Lett.*, 12:132, 1964. doi:10.1016/0031-9163(64)91136-9.
- [9] Borsanyi et al. Full result for the QCD equation of state with 2+1 flavors. *Phys. Lett. B*, 370:99–104, 2014. arXiv:1309.5258, doi:10.1016/j.physletb.2014.01.007.
- [10] A. Bazavov et al. The equation of state in (2+1)-flavor QCD. 2014. arXiv:1407.6387.
- [11] ALICE Collaboration. Measurement of charm production at central rapidity in proton-proton collisions at  $\sqrt{s} = 7$  TeV. *JHEP*, 01(128), 2012. arXiv:1111.1553, doi:10.1007/JHEP01(2012)128.

- [12] ALICE Collaboration. Measurement of charm production at central rapidity in proton-proton collisions at  $\sqrt{s} = 2.76$  TeV. *JHEP*, 07(191), 2012. arXiv:1205.4007, doi:10.1007/JHEP07(2012)191.
- [13] ALICE Collaboration.  $D_s^+$  meson production at central rapidity in proton-proton collisions at  $\sqrt{s} = 7$  TeV. *Physics Letters B*, 718(2):279–294, October 2012. arXiv:1208.1948, doi:10.1016/j.physletb.2012.10.049.
- [14] ALICE Collaboration. Suppression of high transverse momentum D mesons in central Pb-Pb collisions at  $\sqrt{s_{NN}} = 2.76$  TeV. *Journal of high energy physics*, 09(112), 2012. arXiv:1203.2160, doi:10.1007/JHEP09(2012)112.
- [15] ALICE Collaboration. D meson elliptic flow in noncentral Pb-Pb collisions at  $\sqrt{s_{NN}} = 2.76$  TeV. *Phys. Rev. Lett.*, 111(102301), 2013. arXiv:1305.2707, doi:10.1103/PhysRevLett.111.102301.
- [16] ALICE Collaboration. Azimuthal anisotropy of D meson production in Pb-Pb collisions at  $\sqrt{s_{NN}} = 2.76$  TeV. *Phys. Rev. C*, 90(034904), 2014. arXiv:1405.2001, doi:10.1103/PhysRevC.90.034904.
- [17] M. Cacciari, M. Greco, and P. Nason. The  $p_T$  spectrum in heavy-flavour hadroproduction. *JHEP*, 9805(007), 1998. arXiv:hep-ph/9803400, doi:10.1088/1126-6708/2001/03/006.
- [18] P. Braun-Munzinger and J. Stachel. (Non)Thermal aspects of charmonium production and a new look at  $J/\psi$  suppression. *Phys. Lett. B*, 490:196–202, 2000. arXiv:nucl-th/0007059, doi:10.1016/S0370-2693(00)00991-6.
- [19] R. L. Thews, M. Schroedter, and J. Rafelski. Enhanced  $J/\psi$  production in deconfined quark matter. *Phys. Rev. C*, 63(054905), 2001. arXiv:hep-ph/0007323, doi:10.1103/PhysRevC.63.054905.
- [20] STAR Collaboration. Measurements of  $D^0$  and  $D^*$  production in p+p collisions at  $\sqrt{s} = 200$  GeV. *Phys. Rev. D*, 86(072013), 2012. arXiv:1204.4244, doi:10.1103/PhysRevD.86.072013.
- [21] STAR Collaboration. Observation of  $D^0$  meson nuclear modifications in Au+Au collisions at  $\sqrt{s_{NN}} = 200$  GeV. *Phys. Rev. Lett.*, 113(142301), 2014. arXiv:1404.6185, doi:10.1103/PhysRevLett.113.142301.
- [22] H. Qiu. STAR heavy flavor tracker. *Nucl. Phys. A*, 2014. doi:doi:10.1016/j.nuclphysa.2014.08.056.
- [23] K.A. Olive et al. (Particle Data Group). The review of particle physics. *Chin. Phys. C*, 38(090001), 2014.
- [24] D. J. Gross and F. Wilczek. Ultraviolet behavior of non-abelian gauge theories. *Phys. Rev. Lett.*, 30(1343), 1973. doi:10.1103/PhysRevLett.30.1343.

- [25] H. D. Politzer. Reliable perturbative results for strong interactions? *Phys. Rev. Lett.*, 30(1346), 1973. doi:10.1103/PhysRevLett.30.1346.
- [26] K. Wilson. Confinement of quarks. *Phys. Rev. D*, 10(2445), 1974. doi:10.1103/PhysRevD.10.2445.
- [27] R. Alkofer and J. Greensite. Quark confinement: The hard problem of hadron physics. *J. Phys. G*, 34(S3), 2007. arXiv:hep-ph/0610365, doi:10.1088/0954-3899/34/7/S02.
- [28] CBM Collaboration. CBM progress report. 2013. URL: <http://www.fair-center.eu/for-users/experiments/cbm/cbm-documents.html>.
- [29] V. Koch. Aspects of chiral symmetry. *Int. J. Mod. Phys. E*, 6:203–250, 1997. arXiv:nucl-th/9706075, doi:10.1142/S0218301397000147.
- [30] K. Rajagopal and F. Wilczek. The condensed matter physics of QCD. *Ann. Rev. Nucl. Part. Sci.*, 51(131), 2001.
- [31] J.-Y. Ollitrault. Relativistic hydrodynamics for heavy-ion collisions. *Eur. J. Phys.*, 29:275–302, 2008. arXiv:0708.2433, doi:10.1088/0143-0807/29/2/010.
- [32] K. Redlich A. Andronic, P. Braun-Munzinger and J. Stachel. Statistical hadronization of heavy quarks in ultra-relativistic nucleus-nucleus collisions. *Nucl. Phys. A*, 789:334–356, 2007. arXiv:nucl-th/0611023.
- [33] X. Zhu, M. Bleicher, S.L. Huang, K. Schweda, H. Stoecker, N. Xu, and P. Zhuang.  $D\bar{D}$  correlations as a sensitive probe for thermalization in high energy nuclear collisions. *Phys. Lett. B*, 647:366–370, 2007. arXiv:hep-ph/0604178v2, doi:10.1016/j.physletb.2007.01.072.
- [34] CMS Collaboration. First measurement of the cross section for top-quark pair production in proton-proton collisions at  $\sqrt{s} = 7$  TeV. *Phys. Lett. B*, 695:424–443, 2011. arXiv:1010.5994, doi:10.1016/j.physletb.2010.11.058.
- [35] ATLAS Collaboration. Measurement of the top quark-pair production cross section with ATLAS in pp collisions at  $\sqrt{s} = 7$  TeV. *Eur. Phys. J. C*, 71(1577), 2011. arXiv:1012.1792, doi:10.1140/epjc/s10052-011-1577-6.
- [36] K. Schweda. *Prompt production of D mesons with ALICE at the LHC*. Habilitation thesis, Heidelberg University, 2013. arXiv:1402.1370.
- [37] ALICE Collaboration. Heavy flavour decay muon production at forward rapidity in proton-proton collisions at  $\sqrt{s} = 7$  TeV. *Phys. Lett. B*, 708(3–5):265–275, 2012. arXiv:1201.3791, doi:10.1016/j.physletb.2012.01.063.
- [38] ALICE Collaboration. Production of muons from heavy flavour decays at forward rapidity in pp and Pb-Pb collisions at  $\sqrt{s_{NN}} = 2.76$  TeV. *Phys. Rev. Lett.*, 109(112301), 2012. arXiv:1205.6443, doi:10.1103/PhysRevLett.109.112301.

- [39] ALICE Collaboration. Measurement of electrons from semileptonic heavy-flavour hadron decays in pp collisions at  $\sqrt{s} = 7$  TeV. *Phys. Rev. D*, 86(112007), 2012. arXiv:1205.5423, doi:10.1103/PhysRevD.86.112007.
- [40] ALICE Collaboration. Measurement of electrons from beauty hadron decays in pp collisions at  $\sqrt{s} = 7$  TeV. *Phys. Lett. B*, 721(1–3):13–23, 2013. arXiv:1208.1902, doi:10.1016/j.physletb.2013.01.069.
- [41] ALICE Collaboration. Beauty production in pp collisions at  $\sqrt{s} = 2.76$  TeV, measured via semi-electronic decays. *Phys. Lett. B*, 738:97–108, November 2014. arXiv:1405.4144, doi:DOI:10.1016/j.physletb.2014.09.026.
- [42] LHCb Collaboration. Prompt charm production in pp collisions at  $\sqrt{s} = 7$  TeV. LHCb-CONF-2010-013, 2010.
- [43] N. Brambilla et al. Heavy quarkonium: progress, puzzles, and opportunities. *Eur. Phys. J. C*, 71(1534), 2011. arXiv:1010.5827, doi:10.1140/epjc/s10052-010-1534-9.
- [44] M.B. Voloshin. Charmonium. *Prog. Part. Nucl. Phys.*, 61:455–511, 2008. arXiv:0711.4556, doi:10.1016/j.pnpnp.2008.02.001.
- [45] T. Matsui and H. Satz.  $J/\psi$  suppression by quark-gluon plasma formation. *Phys. Lett. B*, 178(4):416–422, 1986. doi:10.1016/0370-2693(86)91404-8.
- [46] F. Karsch and H. Satz. The spectral analysis of strongly interacting matter. *Z. Phys. C*, 51(2):209–224, 1991. doi:10.1007/BF01475790.
- [47] ALICE Collaboration. Centrality, rapidity and transverse momentum dependence of  $J/\psi$  suppression in Pb–Pb collisions at  $\sqrt{s_{NN}} = 2.76$  TeV. *Phys. Lett. B*, 734:314–327, 2014. arXiv:1311.0214, doi:10.1016/j.physletb.2014.05.064.
- [48] A. Andronic, P. Braun-Munzinger, K. Redlich, and J. Stachel. The thermal model on the verge of the ultimate test: particle production in Pb–Pb collisions at the LHC. *J. Phys. G*, 38(124081), 2011. arXiv:1106.6321, doi:doi:10.1088/0954-3899/38/12/124081.
- [49] Y. Liu, Z. Qu, N. Xu, and P. Zhuang.  $J/\psi$  transverse momentum distribution in high energy nuclear collisions. *Phys. Lett. B*, 678:72–76, 2009. doi:doi:10.1016/j.physletb.2009.06.006.
- [50] X. Zhao and R. Rapp. Medium modifications and production of charmonia at LHC. *Nucl. Phys. A*, 859(1):114–125, 2011. doi:10.1016/j.nuclphysa.2011.05.001.
- [51] P. Nason, S. Dawson, and R.K. Ellis. The total cross section for the production of heavy quarks in hadronic collisions. *Nuclear Physics B*, 303(4):607–633, 1988. doi:10.1016/0550-3213(88)90422-1.
- [52] M. Cacciari and M. Greco. Large  $p_T$  hadroproduction of heavy quarks. *Nucl. Phys.*

- B*, 421:530–544, 1994. arXiv:hep-ph/9311260, doi:10.1016/0550-3213(94)90515-0.
- [53] FONLL heavy quark production [online]. 2014. URL: <http://www.lpthe.jussieu.fr/~cacciari/fonll/fonllform.html>.
- [54] P. M. Nadolsky, H.-L. Lai, Q.-H. Cao, J. Huston, J. Pumplin, D. Stump, W.-K. Tung, and C.-P. Yuan. Implications of CTEQ global analysis for collider observables. *Phys. Rev. D*, 78(013004), 2008. doi:10.1103/PhysRevD.78.013004.
- [55] P.M. Nadolsky and Z. Sullivan. PDF uncertainties in WH production at tevatron. In N. Graf, editor, *Proceedings of APS / DPF / DPB Summer Study on the Future of Particle Physics (Snowmass 2001)*, Snowmass, Colorado, 30 Jun - 21 Jul 2001, pp P510, 2001. arXiv:hep-ph/0110378.
- [56] M. Cacciari, S. Frixione, N. Houdeau, M. L. Mangano, P. Nason, and G. Ridolfi. Theoretical predictions for charm and bottom production at the LHC. *JHEP*, 1210(137), 2012. doi:10.1007/JHEP10(2012)137.
- [57] L. Evans and P. Bryant. LHC machine. *Journal of Instrumentation*, 3(S08001), 2008. doi:10.1088/1748-0221/3/08/S08001.
- [58] ATLAS Collaboration. The ATLAS experiment at the CERN Large Hadron Collider. *Journal of Instrumentation*, 3(S08003), 2008. doi:10.1088/1748-0221/3/08/S08003.
- [59] CMS Collaboration. The CMS experiment at the CERN LHC. *Journal of Instrumentation*, 3(S08004), 2008. doi:10.1088/1748-0221/3/08/S08004.
- [60] LHCb Collaboration. The LHCb detector at the LHC. *Journal of Instrumentation*, 3(S08005), 2008. doi:10.1088/1748-0221/3/08/S08005.
- [61] ALICE Collaboration. The ALICE experiment at the CERN LHC. *Journal of Instrumentation*, 3(S08002), 2008. doi:10.1088/1748-0221/3/08/S08002.
- [62] ALICE Collaboration. Performance of the ALICE experiment at the CERN LHC. *Int. J. Mod. Phys. A*, 29(1430044), 2014. arXiv:1402.4476, doi:10.1142/S0217751X14300440.
- [63] J. Alme et al. The ALICE TPC, a large 3-dimensional tracking device with fast readout for ultra-high multiplicity events. *Nucl. Instrum. Meth. A*, 622(1):316–367, 2010. arXiv:1001.1950, doi:10.1016/j.nima.2010.04.042.
- [64] A. Akindinov et al. Performance of the ALICE time-of-flight detector at the LHC. *Eur. Phys. J. Plus*, 128(44), 2013. doi:10.1140/epjp/i2013-13044-x.
- [65] N. Cabibbo. Unitary symmetry and leptonic decays. *Phys. Rev. Lett.*, 10(531), 1963. doi:10.1103/PhysRevLett.10.531.
- [66] M. Kobayashi and T. Maskawa. Cp-violation in the renormalizable theory of weak interaction. *Prog. Theor. Phys.*, 49(2):652–657, 1973. doi:10.1143/PTP.49.652.

- [67] CLEO Collaboration. Updated measurements of absolute  $D^+$  and  $D^0$  hadronic branching fractions and  $\sigma(e^+e^- \rightarrow D\bar{D})$  at  $E_{\text{cm}} = 3774$  MeV. *Phys. Rev. D*, 89(072002), 2014. arXiv:1312.6775, doi:10.1103/PhysRevD.89.072002.
- [68] LHCb Collaboration. Observation of  $D^0 - \bar{D}^0$  oscillations. *Phys. Rev. Lett.*, 110(101802), 2013. arXiv:1211.1230, doi:10.1103/PhysRevLett.110.101802.
- [69] LHCb Collaboration. Prompt charm production in pp collisions at  $\sqrt{s} = 7$  TeV. *Nucl. Phys. B*, 871:1–20, 2013. arXiv:1302.2864, doi:10.1016/j.nuclphysb.2013.02.010.
- [70] T. Sjostrand, S. Mrenna, and P. Skands. PYTHIA 6.4 physics and manual. *JHEP*, 05:026, 2006. arXiv:hep-ph/0603175, doi:10.1088/1126-6708/2006/05/026.
- [71] P. Z. Skands. The Perugia tunes, 2009. arXiv:0905.3418.
- [72] R. Brun and F. Rademakers. Root - an object oriented data analysis framework. In Phys. Res. A, editor, *AIHENP'96 Workshop, Lausanne, Sep. 1996*, *Nucl. Inst. & Meth.*, volume 389, pages 81–86, 1997.
- [73] AliRoot reference manual [online]. 2014. URL: <http://aliweb.cern.ch/Offline/AliRoot/Reference.html>.
- [74] ALICE Collaboration. ALICE computing: Technical Design Report. CERN-LHCC-2005-018, 2005. URL: <https://cds.cern.ch/record/832753?ln=en>.
- [75] ALICE Collaboration. Measurement of inelastic, single- and double-diffraction cross sections in proton–proton collisions at the lhc with alice. *Eur. Phys. C*, 73:2456, 2013. arXiv:1208.4968, doi:10.1140/epjc/s10052-013-2456-0.
- [76] R. Frühwirth. Application of Kalman filtering to track and vertex fitting. *Nucl. Instr. and Meth. A*, 262(2-3):444–450, 1987. doi:10.1016/0168-9002(87)90887-4.
- [77] W. Blum and L. Rolandi. Particle detection with drift chambers, Springer, 1998.
- [78] R. Brun et al. GEANT detector description and simulation tool. CERN Program Library Long Write-up W5013, 1994. URL: <http://wwwasdoc.web.cern.ch/wwwasdoc/pdfdir/geant.pdf>.
- [79] LHCb Collaboration. Studies of beauty baryon decays to  $D^0 p h^-$  and  $\Lambda_c^+ h^-$  final states. *Phys. Rev. D*, 89(032001), 2014. arXiv:1311.4823, doi:10.1103/PhysRevD.89.032001.
- [80] ATLAS Collaboration. Comparison of  $D^{(*)}$  meson production cross sections with FONLL and GM-VFNS predictions. ATL-PHYS-PUB-2011-012, 2011. URL: <http://cds.cern.ch/record/1378479>.
- [81] ATLAS Collaboration. Measurement of  $D^{(*)}$  meson production cross sections in pp collisions at  $\sqrt{s} = 7$  TeV with the ATLAS detector. ATLAS-CONF-2011-017, 2011. URL: <http://cds.cern.ch/record/1336746>.

- [82] C. Lourenco and H. K. Wohri. Heavy flavour hadro-production from fixed-target to collider energies. *Phys. Rept.*, 433:127–180, 2006. arXiv:hep-ph/0609101, doi:10.1016/j.physrep.2006.05.005.
- [83] PHENIX Collaboration. Heavy quark production in p+p and energy loss and flow of heavy quarks in Au+Au collisions at  $\sqrt{s_{\text{NN}}} = 200$  GeV. *Phys. Rev. C*, 84(044905), 2011. arXiv:1005.1627, doi:10.1103/PhysRevC.84.044905.
- [84] M. L. Mangano, P. Nason, and G. Ridolfi. Heavy-quark correlations in hadron collisions at next-to-leading order. *Nucl. Phys. B*, 373(2):295–345, 1992. doi:10.1016/0550-3213(92)90435-E.
- [85] ALICE Collaboration. Technical design report for the upgrade of the ALICE Inner Tracking System. *J. Phys. G: Nucl. Part. Phys.*, 41(087002), 2014. doi:10.1088/0954-3899/41/8/087002.

## Acknowledgements

First and foremost, I would like to thank Kai Schweda for providing the exciting topic of my master thesis and for his great encouragement and support during the last year. I would like to express my gratitude to Ulrich Uwer for reading and evaluating this thesis.

Furthermore, I am grateful to Johanna Stachel for giving me the opportunity to join the ALICE group at the PI in Heidelberg. I would like to thank my office colleagues Michael and Martin and everybody in the working group for the pleasant atmosphere and the inspiring environment that I enjoyed during the last year. A big thanks goes to Michael Winn for his continuous interest in the progress of my work and for his answers to numerous questions. I am thankful to Martin Völkl for interesting discussions on statistical methods and on the determination of systematic uncertainties. I would also like to thank Jeremy Wilkinson for his support with computing issues and for helping me to significantly improve my English skills.

I wish to thank Zaida Conesa del Valle, Davide Caffari, Francesco Prino, Andrea Rossi, Chitrasen Jena, Massimo Venaruzzo and Andrea Dainese for many helpful discussions during meetings and via email. I am thankful to the conveners for the possibility to present and discuss my work in the D2H group and PWGHF.

Last but not least, I wish to express my gratitude to Michael Winn, Jeremy Wilkinson, Yvonne Pachmayer and Martin Völkl for proofreading my thesis.

This work was supported by the Cusanuswerk and by the Federal Ministry of Education and Research under promotional reference 06HD197D.

## Erklärung

Ich versichere, dass ich diese Arbeit selbstständig verfasst und keine anderen als die angegebenen Quellen und Hilfsmittel benutzt habe.

Heidelberg, den 1. Dezember 2014,